



School of Computing and Engineering

Synthesis and corrosion resistance of High Entropy materials for petrochemical applications

A thesis submitted to the University of Huddersfield in partial fulfilment of
the requirements for the award of the degree of Doctor of Philosophy

Waleed Muftah

Supervisor: Professor Vladimir Vishnyakov

Co-supervisor: Professor John Allport

February 1st, 2023

Abstract

Many industrial processes require materials with high erosion properties, e.g. a material must be both corrosion and wear resistant. Therefore, the work presented aimed to find novel alloys with high erosion resistance in the form of High Entropy Materials while preferably utilising common, widely available elements. Furthermore, it was planned from the beginning that additional corrosion resistance might be achieved if the alloys could be produced as an amorphous material.

Vacuum arc melting was used in search of complex multielement alloys with minimal or absent phase separation. The thin film production was seen as a step to reduce the material cost of the found promising alloys and to further increase alloy mechanical properties by creating the alloy in the slight deviation from the thermodynamical equilibrium.

Electron microscopy (Scanning and Transmitting) in combination with X-Ray Diffraction was employed to get insides into crystalline arrangements. At the same time, Energy Dispersive X-Ray (EDX) spectroscopy allowed us to determine phase compositions.

The main finding in bulk alloys results showed that the FeCrMnNiC_x ($x=2$ at. %) had a single-phase structure with no evidence of elemental segregation, thereby confirming that the synthesized alloy is a single-phase high entropy alloy. The results of FeCrMnNiC and FeCrSiNb high entropy thin film alloys deposited on silicon and steel substrates exhibited that the alloys are equiatomic and single-phase with no element separation or segregation. As well as the FeCrMnNiC and FeCrSiNb thin film alloys showed amorphous structure.

Both materials coated with the material samples (on silicon and steel) showed corrosion resistance exceeding one of the 304 SS in 0.6 M NaCl, H_2SO_4 solutions, and crude oil at standard temperature and pressure.

The novel materials also show very high hardness for metallic/metalloid composition. The exceptional properties of the alloys allow us to designate them for use in highly erosive environments.

Copyright Statement:

- I. The author of this thesis (including any appendices and/or schedules to this thesis) owns any copyright in it (the Copyright), and he has given The University of Huddersfield the right to use such copyright for any administrative, promotional, educational and/or teaching purposes.
- II. Copies of this thesis, either in full or in extracts, may be made only in accordance with the regulations of the University Library. Details of these regulations may be obtained from the Librarian. This page must form part of any such copies made.
- III. The ownership of any patents, designs, trademarks and any all-other intellectual property rights except for the Copyright (the Intellectual Property Rights) and any reproductions of copyright works, for example, graphs and tables (Reproductions), which may be described in this thesis, may not be owned by the author and may be owned by third parties. Such Intellectual Property Rights and Reproductions cannot and must not be made available for use without the prior written permission of the owner(s) of the relevant Intellectual Property Rights and/or Reproductions.

DECLARATION

I, Waleed Muftah, declare that no portion of the work referred to in the thesis has been submitted in support of an application for another degree or qualification of this or any other university or another institute of learning.

Publications and presentations:

Sections of this study have been presented at international conferences and published in scientific journals.

Journals Publications:

- Muftah, W., & Vishnyakov, V. (2021). Microstructure and properties of FeCrMnNiCx compositionally complex bulk alloys. *Vacuum*, 188, 110181.
- Muftah, W., Patmore, N., & Vishnyakov, V. (2020). Demanding applications in harsh environments–FeCrMnNiC amorphous equiatomic alloy thin film. *Materials Science and Technology*, 36(12), 1301-1307.
- Muftah, W., Allport, J., & Vishnyakov, V. (2021). Corrosion performance and mechanical properties of FeCrSiNb amorphous equiatomic HEA thin film. *Surfaces and coatings technology*, 36(12), 1301-1307.

Conference Presentations:

- Waleed Muftah & Vladimir Vishnyakov. (May 2021). Microstructure and Corrosion performance of equiatomic FeCrMnNiC amorphous high entropy thin film alloy. *Ions, Plasmas and Thin Films*. Institute of Physics (IOP), London – UK.
- Waleed Muftah & Vladimir Vishnyakov. (June 2021). Synthesis and Corrosion resistance of FeCrMnNiC amorphous HEA. *Thermic “International conference on processing & manufacturing of advanced materials”*. Vienna – Austria.

Acknowledgements

My sincere gratitude goes to my main supervisor, professor Vladimir Vishnyakov for guiding me and for his endless support throughout my PhD study, which started from scratch, and for his important advice in publishing papers in journals, really thank you.

I would like to thank my co-supervisor, professor John Alport for his comments and recommendations, which were truly valuable. Also, I would like to acknowledge the University of Huddersfield for granting me a fee waiver to study PhD. I am also thankful to all the research team and technicians at the School of Computing and Engineering.

Further, I would like to thank the Libyan cultural attaché and the Libyan ministry of higher education and scientific research for the financial support.

Special thanks to all my family members, my parents, brothers, sisters, nieces, nephews, uncles and cousins, for their unlimited support. A big thanks from the bottom of my heart to my wife for her support and for affording my tense situation during the study journey.

I would like to thank my best friend, Zeyad Rashed for his support. I would also like to thank my colleague and friend Mohammed Imtyaz for his support during my PhD study.

I am extremely grateful to everyone at the University of Huddersfield for their kind help and support.

Contents

1	Chapter 1: general introduction	17
1.1	Introduction:	18
1.2	Aims & objectives	21
1.2.1	Aims	21
1.2.2	Objectives	21
2	Chapter2: literature review	22
2.1	Corrosion process in the oil & gas sector	23
2.2	Overview of types of corrosion	23
2.2.1	CO ₂ corrosion	26
2.2.2	H ₂ S corrosion	27
2.2.3	Erosion corrosion	27
2.2.4	Oxygen corrosion	27
2.2.5	Crevice corrosion	28
2.2.6	Galvanic corrosion	28
2.2.7	Stress corrosion cracking (SCC)	28
2.2.8	Microbiologically Induced Corrosion (MIC)	29
2.3	Types and material selection of CRAs in the oil & gas industry	29
2.4	Coating in the oil and gas sector	30
2.4.1	Thin film technology:	31
2.5	Amorphous materials	32
2.6	High entropy alloys (HEAs)	33
2.6.1	Compositionally Complex alloys	34
2.6.2	High entropy thin films (HEAs TF)	34
2.6.3	The corrosion resistance of HEAs	35
2.6.4	Amorphous HEAs	42
2.6.5	Hardness and Nano-indentation of HEAs	43

2.7	Summary	45
3	Chapter3: Materials and Methods	47
3.1	Vacuum arc melting furnace	48
3.2	Scanning Electron Microscopy (SEM)	50
3.2.1	Signals available in the SEM	51
3.2.2	Secondary Electron (SE) images.....	52
3.2.3	Backscattered Electron (BSE) images	52
3.2.4	Characteristic X- rays.....	53
3.3	Transmission Electron Microscopy (TEM)	53
3.4	Focused Ion Beam.....	55
3.5	Ion Beam Sputter deposition:.....	56
3.6	Grinding and polishing equipment.....	58
3.6.1	Grinding and polishing process:	59
3.7	X-ray Diffraction (XRD)	59
3.8	Corrosion measurement	61
3.8.1	Electrochemical Tests	61
3.8.2	Polarization technique and Polarization Curves	62
3.8.3	Potentiodynamic Polarization technique.....	63
3.8.4	Passivity	63
3.9	Potentiostat.....	66
3.9.1	NOVA software	69
3.9.2	Electrochemical cell.....	70
3.10	Nanoindentation	70
3.11	Materials preparation	72
4	Chapter4: “Microstructure and properties of FeCrMnNiCx compositionally complex bulk alloys.”	76
4.1	Chapter overview	77
4.2	Materials and methods	79

4.3	Results and discussion	80
4.3.1	Microstructure	80
4.4	Corrosion test	89
4.5	Mechanical properties	91
4.6	Summary	92
5	Chapter5: “Demanding applications - FeCrMnNiC amorphous equiatomic alloy thin film.”	93
5.1	Chapter overview	94
5.2	Materials and methods	95
5.3	Results and Discussion	96
5.3.1	Microstructure	96
5.3.2	Electrochemical tests	100
5.4	Nanomechanical properties	106
5.5	Summary	109
6	Chapter6: “Corrosion performance and mechanical properties of FeCrSiNb amorphous equiatomic HEA thin film.”	110
6.1	Chapter overview	111
6.2	Materials and methods	112
6.3	Results and discussion	114
6.3.1	Microstructure	114
6.3.2	Corrosion tests	120
6.4	Mechanical properties	125
6.5	Summary	129
7	Chapter7: Deposit FeCrMnNiC & FeCrSiNb amorphous high entropy alloys thin films on steel and conduct corrosion tests in crude oil	130
7.1	Chapter overview	131
7.2	Materials and methods	132
7.3	Results and discussion	133

7.3.1	Microstructure of FeCrMnNiC	133
7.3.2	Corrosion test of FeCrMnNiC in crude oil	136
7.3.3	Microstructure of FeCrSiNb	138
7.3.4	Corrosion test of FeCrSiNb in crude oil	140
7.4	Summary	143
8	Chapter8: general conclusion	144
8.1	Conclusion	145
9	References.....	152
10	Appendix.....	173

List of figures:

Figure 2-1: general internal corrosion of crude oil pipeline due to salt and CO ₂ environment [14]. ...	24
Figure 2-2: pitting corrosion of a natural gas pipeline CO ₂ environment [18].	25
Figure 2-3: the difference between uniform, pitting corrosion [19].	26
Figure 2-4: Polarization curves of FeCoNiCrCu _x alloys and 304L in NaCl solution at room temperature [60].	36
Figure 2-5: Potentiodynamic polarization curves of CoNiCuFeCr equiatomic alloy coating and 304 ss in 1 N HCL solution [67].	41
Figure 3-1: Schematic of vacuum arc melting furnace [77].	49
Figure 3-2: Schematic drawing of the scanning electron microscope [86].	51
Figure 3-3: different types of imaging modes [83].	52
Figure 3-4: Schematic diagram of transmission electron microscope components [91].	55
Figure 3-5: targets (a: elemental targets of Fe, Cr, Si and Nb), (b: composite target of FeCrMnNi, and C sheet) positioning during the deposition process used in the current work.	58
Figure 3-6: a Bruker D2 Phaser instrument (XRD) used in the current study.	61
Figure 3-7: typical potentiodynamic polarisation curve of 304 SS [111].	65
Figure 3-8: potentiodynamic polarisation curve of 304 SS in 1 M NaCl solution [112].	66
Figure 3-9: an Autolab potentiostat used in this study.	68
Figure 3-10: the three electrodes set up, RE reference electrode, WE working electrode and CE counter electrode [116].	69
Figure 3-11: Figure 12: nano test, made by Micro Materials (UK), used in the present work [122]. ..	72
Figure 3-12: Vacuum Arc Melting Furnace at the University of Huddersfield.	73
Figure 3-13: Ion Sputter Deposition System University of Huddersfield.	74
Figure 4-1: Analysis of microstructure and compositions of equiatomic alloy. (a) – average chemical composition of equiatomic FeCrMnNiC; (b) – BSED surface microstructure image; (c) - chemical composition of the lighter element phase.	81
Figure 4-2: EDX mapping of FeCrMnNiC bulk alloy.	81

Figure 4-3: Analysis of microstructure and compositions of equiatomic alloy. (a) – average chemical composition of FeCrMnNiC0.5; (b) – BSED surface microstructure image; (c) - chemical composition of the lighter element phase.	82
Figure 4-4: EDX mapping of FeCrMnNiC with 10 at. % of C bulk alloy.....	83
Figure 4-5: Microstructure analysis in FeCrMnNiCx alloy with 6 at. % of C: (a) - chemical composition of the alloy; (b) - BSED surface microstructure image at high magnification; (c) - chemical composition of the dark area as marked in (b).	84
Figure 4-6: EDX element mapping of FeCrMnNiC0.3 bulk alloy.	84
Figure 4-7: Analysis of the surface microstructure of FeCrMnNiCx alloy with 2 at. % of C: (a) - BSED surface image; (b) - chemical composition.	85
Figure 4-8: Alloy element EDX mapping in FeCrMnNiC0.1.....	86
Figure 4-9: XRD patterns of crystalline FeCrMnNiCx bulk alloys with different carbon content as shown in distinctive peaks.	87
Figure 4-10: Potentiodynamic polarisation curves of FeCrMnNiCx bulk alloys.	90
Figure 5-1: Surface microstructure of FeCrMnNiC amorphous high entropy thin film alloy (A) and elemental composition (B).	96
Figure 5-2: Elemental EDX mapping of FeCrMnNiC thin film.	97
Figure 5-3: XRD pattern of amorphous FeCrMnNiC high entropy thin film alloy.	98
Figure 5-4: BFTEM image (a) and its SAED (b) of FeCrMnNiC thin film deposited on silica substrate at room temperature. The film in the image is in the right-bottom corner.....	99
Figure 5-5: Potentiodynamic polarisation curve of FeCrMnNiC amorphous high entropy thin film & 304 SS in aqueous 3.5% NaCl solutions at room temperature	101
Figure 5-6: Potentiodynamic polarisation curve of FeCrMnNiC amorphous high entropy thin film & 304 SS 0.6 M H2SO4 solution.....	102
Figure 5-7: polarization curves of FeCrSiNb HEA thin film & 304 SS in crude oil.	103
Figure 5-8: Nanoindentation data set for FeCrMnNiC amorphous HEATF.....	107
Figure 5-9: Reduced modulus value over plastic depth. The approximation to zero plastic depth was done by a linear fit.	107

Figure 6-1: SEM analysis of the amorphous equiatomic FeCrSiNb high entropy alloy thin film. (a): BSE image microstructure image. (b): chemical composition of HEA thin film.	114
Figure 6-2: EDX mapping of the amorphous equiatomic FeCrSiNb HEA thin film.....	115
Figure 6-3: EFTEM images of the amorphous equiatomic FeCrSiNb HEA thin film.....	116
Figure 6-4: XRD pattern of the FeCrSiNb thin film on a silica substrate.....	117
Figure 6-5: XRD pattern of the silica glass substrate.	118
Figure 6-6: (a): BFTEM images of the amorphous equiatomic FeCrSiNb high entropy alloy thin film synthesised by ion beam sputtering, and fig. 6 (b) SAED images of amorphous film taken from the marked area.....	119
Figure 6-7: polarisation curves of the amorphous equiatomic FeCrSiNb high entropy alloy thin film and 304 SS in 0.6 M NaCl solution.	121
Figure 6-8: polarisation curves of amorphous equiatomic FeCrSiNb high entropy alloy thin film and 304 SS in 0.6 M H ₂ SO ₄ solution.....	122
Figure 6-9: polarisation curves of FeCrSiNb HEA thin film & 304 SS in crude oil.	123
Figure 6-10: Nanoindentation data for amorphous equiatomic FeCrSiNb HEA thin film.	126
Figure 6-11: Reduced Young's modulus of amorphous equiatomic FeCrSiNb HEA thin film.	127
Figure 7-1: (a) BSE surface microstructure image of FeCrMnNiC amorphous HEA thin film alloy deposited on steel, and (b) elemental chemical composition.	133
Figure 7-2: elemental mapping of FeCrMnNiC amorphous HEA thin film alloy deposited on steel	134
Figure 7-3: XRD pattern of FeCrMnNiC amorphous HEA thin film alloy deposited on the steel.....	135
Figure 7-4: XRD pattern of steel substrate.	136
Figure 7-5: polarization curves of FeCrMnNiC HEA thin film deposited on steel & SS304 in crude oil.	137
Figure 7-6: (a) BSE microstructure image of FeCrSiNb amorphous HEA thin film alloy deposited on steel, (b) elemental chemical composition.....	138
Figure 7-7: elemental mapping of FeCrSiNb amorphous HEA TF	139
Figure 7-8: XRD pattern of FeCrSiNb amorphous HEA thin film alloy deposited on the steel.....	140

Figure 7-9: polarization curves of FeCrSiNb HEA thin film deposited on steel & 304 SS in crude oil.	141
Figure 8-1: polarization curves of FeCrMnNiC and FeCrSiNb HE TF alloys deposited on silicon and 304 SS in 0.6 M NaCl solution.	146
Figure 8-2: polarization curves of FeCrMnNiC and FeCrSiNb HE TF alloys deposited on silicon and 304 SS in 0.6 M H ₂ SO ₄ solution.....	147
Figure 8-3: polarization curves of FeCrMnNiC and FeCrSiNb HE TF alloys deposited on silicon and 304 SS in crude oil.	147
Figure 8-4: polarization curves of FeCrMnNiC and FeCrSiNb HE TF alloys deposited on mild steel and 304 SS in crude oil.	148

List of tables:

Table 4-1: Corrosion parameters of FeCrMnNiCx bulk alloys.	89
Table 5-1: Corrosion parameters of FeCrMnNiC amorphous HETF and different types of HEAs tested in 3.5% NaCl solution.....	101
Table 5-2: the corrosion parameters of FeCrSiNb HE TF alloy and 304 SS in 0.6 M H ₂ SO ₄ solution.	103
Table 5-3: the corrosion parameters of FeCrSiNb HEA thin film and 304 SS in crude oil.....	104
Table 6-1: the corrosion parameters of FeCrSiNb HEA thin film and 304 SS in 0.6 M NaCl solution.	121
Table 6-2: corrosion parameters of FeCrSiNb HEA thin film and 304 SS in 0.6 M H ₂ SO ₄ solution.	122
Table 6-3: corrosion parameters of FeCrSiNb HEA thin film and 304 SS in crude oil.....	123
Table 7-1: corrosion parameters of FeCrMnNiC HE TF alloy deposited on steel and SS304 in crude oil.	137
Table 7-2: corrosion parameters of FeCrSiNb HE TF alloy deposited on steel and 304 SS in crude oil	141

Thesis structure:

This thesis is arranged into eight chapters:

Chapter 1: discusses a general introduction to corrosion problems with its risk and some suggested solutions.

Chapter 2: presents a literature review of corrosion types, especially in the oil and gas field, coating and thin film technology, amorphous metals and high entropy alloys as a solution to the corrosion problem.

Chapter 3: contains a list of all the laboratory techniques and equipment used to synthesize and characterise the alloys.

Chapter 4: presents microstructure and properties of FeCrMnNiC_x ($x = 20, 10, 5$ and 2 at. %) compositionally complex bulk alloys. And deeply discusses how a single phase of FeCrMnNiC_2 has been reached.

Chapter 5: outlines the synthesis and corrosion performance of the synthesized FeCrMnNiC amorphous equiatomic alloy thin film.

Chapter 6: discusses the corrosion performance and mechanical properties of the synthesized FeCrSiNb amorphous equiatomic HEA thin film.

Chapter 7: presents the synthesis and corrosion performance of the FeCrMnNiC & FeCrSiNb amorphous high entropy alloys thin films deposited on steel substrates.

Chapter 8: contains a general conclusion of the proposed work and recommendations for future work.

1 Chapter 1: general introduction

1.1 Introduction:

The phenomenon of corrosion is historically related to metals and has been considered a threat that destroys structures and metals. Human civilization cannot exist without metals, but corrosion is one of their major barriers. Even though corrosion is a widely known process, it has been considered passively by researchers and scientists in the past [1]. Scientists have defined corrosion as the deterioration of a given material or its properties due to interaction with its immediate surrounding. Corrosion is also described as an electrochemical reaction that occurs upon the exposure of metals to the environment. The deterioration of the metal is a manifestation of the oxidation-reduction reaction that involves the release of electrons by the exposed metal (as anode) into the surrounding (as cathode) environment. This environment in the oil and gas industry includes crude oil, gas, different products of petroleum, fuels, an aqueous environment, fuel additives and other components [2].

The two major types of corrosion are internal and external corrosion; internal corrosion occurs inside tanks, pipes, boilers, and other structures. Internal corrosion is associated with the movement and storage of hydrocarbons and fluids inside pressure vessels and tanks. Internal corrosion is driven by the corrosive components found inside fluids and hydrocarbons. External corrosion, on the other hand, is any form of corrosion of the exterior part of metals exposed to the environment due to environmental factors such as seawater, rain, temperature, microbes, humidity, and external forces that might impact the surface [3].

There are numerous ways through which materials corrode upon contact with the environment. Generally, a corrosion process involves various mechanisms that occur when metals are in contact with the environment. Mechanisms may include atomic, molecular, or ionic transport processes. Additionally, the tendency of metals to corrode is related to the energy state, where the pipes and lines components undergo variable conditions of the well caused by variations in

fluid compositions and variations in working conditions of the temperatures and pressures. High impurity products such as free water, carbon dioxide, naphthenic acid, etc., are common contaminants of crude oil and natural gas [4, 5] that cause the degradation or removal of the material surface.

Consequently, loss of mechanical properties such as strength and ductility can lead to a reduction in thickness, loss of material and ultimate failure. There will be a point where the pipe (or any component in the field) might completely fail and require replacement; this requires stopping the production process, which is an unfavourable issue [6]. As a result, the risk of a failure due to corrosion is equivalent to the chances of such a failure multiplied by the consequences of the failure. The overall cost of a corrosion-related failure comprises the replacement cost, clean-up cost, downtime cost, repair cost, etc.; hence, it is often measured in financial terms [1].

Furthermore, in the oil and gas sector, corrosion costs much in lost profits and costs of the treatment per year. In the USA, industry corrosion costs are estimated at around \$170 billion per year, and more than half of these costs are considered for the oil and gas industry [4]. Corrosion costs studies have been carried out in Great Britain, Japan, Australia and other countries. The corrosion cost is approximately 3 – 4 % of the Gross National Product in each country [1].

To transfer crude oil and natural to saleable products, a refinery is a big industrial compound with extended pipes to transport different fluids between big reactor units operated continuously, making process optimization and process control very desirable [7]. To reduce the economic effect of corrosion, corrosion scientists and corrosion engineers attempt to decrease the losses of material and the accompanying economic losses which are produced from the corrosion of metal components of machines, piping, ships, tanks, marine structures,

bridges, and others that based on materials [8]. Metallic materials applied to make-up equipment for refining industries and gas processing are exposed to a wide diversity of potentially destructive mechanisms, and the most common is corrosion. Numerous methods and techniques have been used for corrosion prevention and control in the oil and gas sector, for example, anodic and cathodic protection, material selection, paint, and internal and external coatings [9]. A successful corrosion control and management strategy can contribute to asset integrity conservation in the oil and gas sector [4].

1.2 Aims & objectives

1.2.1 Aims

This study strives towards creating coating in the form of amorphous high entropy thin films to protect soft iron and steel used in the oil and gas industry.

1.2.2 Objectives

- Synthesis of single-phase complex concentrated alloys by arc melting
- Deposit amorphous high entropy alloy (HEA) thin films by Ion Beam Sputtering
- Provide a screening of the alloy morphology, microstructure and chemical composition by SEM, XRD and EDX
- Select the best corrosion resistance alloy and undertake characterisation in various corrosive media and extreme application environments
- Assess the mechanical properties of the produced selected alloys

2 Chapter2: literature review

2.1 Corrosion process in the oil & gas sector

A major issue in the oil and gas sector is corrosion, which damages most of the installed metallic structures. Corrosion is an unavoidable problem due to the impact of two major factors - the environment and the working conditions. Corrosion results from the interaction of a metal material with its immediate environment [6]. Any aquatic solution or environment can enhance corrosion under various complicated pipeline systems conditions. The process consists of three main parts: a cathode, an anode and an electrolyte. The corroding metal is the anode; the cathode composes an electrical conductor in the cell. The corrosive medium is the electrolyte that allows electrons to migrate from the anode to the cathode [4, 10].

The most common observed type of corrosion in the oil & gas sector occurs when steel contacts with oil, gas, or water and forms rust [10]. After exposing the metal to an electrolyte (the corrosive solution, e.g., water), the metal atoms at the anode lose electrons that the metal atoms will absorb at the cathode. This process involves the simultaneous presence of electrolytes and oxygen. As a result, the entire surface of the metal will be oxidized, leading to damage in the metal surface. This process is known as the electrochemical process [4, 11].

2.2 Overview of types of corrosion

Corrosion can be categorized into localized and uniform or general corrosion; uniform corrosion, as shown in fig. 2-1 is a type of corrosion that can be predicted and controlled and distributes uniformly over the entire material surface after exposing to the atmosphere, water or liquid, resulting in the formation of rust. Uniform corrosion is easy to detect and predict by some assumptions and equations. It is usually slow [12], where localized corrosion cannot be easily predicted or controlled because it is an accelerated attack of a passive material at discrete sites in the presence of corrosive media in which the passive protective layer is broken down. In contrast, the rest of the material surface corrodes slower. Localized corrosion is very fast

due to the concentration on a small area. The most common form of localized corrosion is pitting [13].



Figure 2-1: general internal corrosion of crude oil pipeline due to salt and CO₂ environment [14].

Pitting corrosion is an extremely localized corrosion that results in the development of small holes, cavities or pits on the material, as the surrounding metal is not affected during pitting. The initial phase of pitting (the beginning of the pit) starts with a "flaw" on the surface of the metal, mostly in the presence of a different potential on the affected part compared to that of the surrounding metal. A fault could be created by the breakdown of passive layers, for

instance, in stainless steel, changes in the metal's structure, coating removal, or microbiological reactions caused by bacteria. Pitting corrosion is believed to be very dangerous because it forms a small deep hole in a small area, making it difficult to detect and control [15-17]. Fig. 2.2 presents an example of pitting corrosion of a natural gas pipeline in a CO₂ environment.



Figure 2-2: pitting corrosion of a natural gas pipeline CO₂ environment [18].

Figure 2.3 (a and b) below illustrates a simple difference between uniform/general corrosion and pitting corrosion.

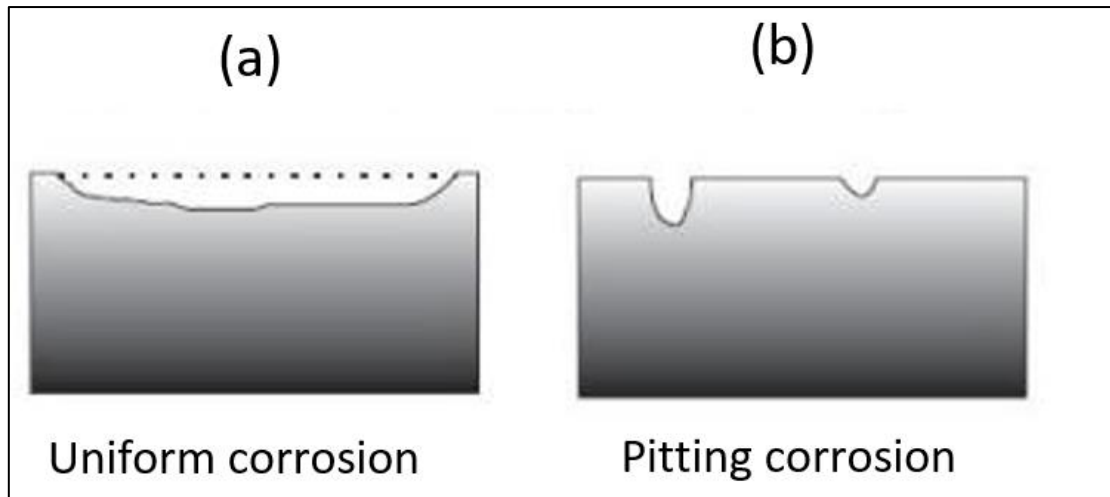


Figure 2-3: the difference between uniform, pitting corrosion [19].

The commonest corrosion types in the oil & gas sector are erosion-corrosion, crevice corrosion, oxygen corrosion, stress corrosion cracking, galvanic corrosion, and microbiologically induced corrosion; water acts as the catalyst for all these corrosion processes [11].

2.2.1 CO₂ corrosion

This is the commonest form of corrosion in the oil and gas field; it is also called sweet corrosion and was first reported in Texas in the 1940s. Due to the high temperatures in the oil & gas systems, dry CO₂ gas on its own is not corrosive, but when in an aqueous phase, enhances the electrochemical reaction between metal and the surrounding media [20]. CO₂ is partially higher soluble in hydrocarbons than in water. Hydrocarbon reservoirs include fluids and a certain amount of CO₂ gas, always in contact with the aqueous media. Therefore, CO₂ dissolves in the aqueous media of hydrocarbon products, and this aqueous phase leads to steel pitting corrosion. [21]. CO₂ corrosion can be in the form of pitting or/and mesa attack, a localized CO₂ corrosion under medium flow conditions [22].

2.2.2 H₂S corrosion

Hydrogen sulphide corrosion (known as sour corrosion) was first reported in the casing and tubing of gas wells in US & Canada in 1950-1951 [23]. H₂S is not corrosive on its own; however, it becomes corrosive mixed with water. H₂S dissolves water, produces weak acid, and then slightly dissociates to create hydrogen and bisulphate ions. In the occurrence of H₂S, materials suffer from corrosion that leads to hydrogen generation; hence, hydrogen encourages cracking and embrittlement problems which can lead to tragic failure. Pitting corrosion can happen under certain circumstances of flow rate, temperature, and the ratio of CO₂ to H₂S. [24].

2.2.3 Erosion corrosion

Erosion control refers to the increasing rate of attack or degradation of a metal due to the frequent contact between the surface of a metal and a reactive fluid. This contact is rapid and driven by either abrasion or mechanical wear. Metal removal from a surface can be done either by dissolving the metal into ions or by producing solid corrosion products that can be manually brushed off from the metal surface. Erosion-corrosion damage affects almost all metals and alloys. Many rely on forming a surface coating (passivity) for corrosion resistance. However, the failure of these protective surfaces due to friction or breakage exposes the metals or alloys to intense attacks, resulting in erosion-corrosion [7, 25].

2.2.4 Oxygen corrosion

This form of corrosion results from the breakdown of metals due to the rapid rate of oxidation and the reactivity of the resulting dissolved ions to generate insoluble deposits in the presence of oxygen. As a powerful oxidant, oxygen reacts rapidly with metals. Metallic surfaces experience corrosion when there is a considerable amount of oxygen, water, and electrolytic environments. Because of leaking pump seals, open hatches, casing, and process vents, the good fluids are oxygen-contaminated. Oxygen functions as an electron acceptor and depolarizer during cathodic processes, aiding the metal deterioration at the anode. The

corrosive effects of acid gases are more significant in the presence of oxygen (H₂S and CO₂). Pitting and uniform corrosion are the most common corrosion types related to oxygen [4, 26].

2.2.5 Crevice corrosion

This is a localized form of corrosion where the attack happens because part of a metal surface is in a restricted or shielded environment where a small amount of liquid is trapped between two parts lacking oxygen, for instance, under seals or gaskets gaps, spaces filled with deposits, inside cracks, and contact areas between parts. In the shielded area, this form of corrosion occurs as a crevice or crack between the surface of the metal and between metal & non-metal surfaces [27, 28].

2.2.6 Galvanic corrosion

Galvanic corrosion occurs from the electrical connection of dissimilar alloys or metals and their subsequent immersion in a conductive fluid. The galvanic series portrays the existence of a potential difference between two dissimilar metals when close to each other in a solution. Metals far apart in the galvanic series tend to encounter more galvanic corrosion. The materials with less corrosion resistance are more prone to corrosion, while those with less corrosion resistance are less corrosive; in other words, the more corrosion-resistant materials become the cathode while the less corrosion-resistant materials become the anode, paving the way for galvanic corrosion [29].

2.2.7 Stress corrosion cracking (SCC)

This cracking occurs mainly due to the co-presence of sensitive material, tensile stress, and a corrosion-favourable environment. SCC may not cause a significant metal loss but only occurs when certain metals are subjected to tensile stress in certain environments; SCC may occur rapidly without notice. For different alloys, the type of SCC depends on the type of corrosive environment; for instance, stainless steel can only crack in a chloride environment [7].

2.2.8 Microbiologically Induced Corrosion (MIC)

This is a form of corrosion facilitated by the action of microbes. MIC can present in different forms but can be controlled using biocides or other traditional corrosion control approaches. Most (MIC) is in the form of pits beneath colonies of live biological materials, mineral deposits, and bio-deposits. This biofilm protects the microbes from the harmful external environment, thereby enhancing the rate of MIC. Bio-corrosion or MIC is mostly encountered in cooling water systems, refineries, oil field water-handling systems, sprinkler water systems, gas processing plants, and oil pipelines, but it isn't always a serious problem in high-temperature steam systems [25].

2.3 Types and material selection of CRAs in the oil & gas industry

Corrosion resistance alloys (CRAs) provide good corrosion resistance to the application exposed to oil and gas environments. These applications include pipelines, vessels, valves, piping systems, downhole tubing, safety facilities and other equipment. Corrosion-resistance alloys are stainless steel and nickel alloys based. The selection of (CRAs) depends on temperature, pressure, hydrogen sulphide, carbon dioxide and chloride, as shown below [30].

13 Cr (Martensitic Stainless Steel): It can only be applicable in the absence of H_2 and H_2S because a small amount of H_2 can create pitting; therefore, 13 Cr alloy is not favourable to use in the long term [31].

316L (Austenitic Stainless Steel): It is mostly used for clad line pipe, vessel cladding and surface piping; however, when exposed to seawater, around 3.5 % NaCl at 20°C and more could form pitting. Also, the small amount of H_2 & H_2S can impact the resistance of 316 alloys to cracking and corrosion [31].

22 Cr (Duplex Stainless Steel): Compared to 13 Cr and 316L, 22 Cr has shown greater resistance to corrosion in NaCl & CO₂, but in the presence of H₂S also, 22 Cr alloy exhibited sensitivity to corrosion and cracking [32].

Alloy 28: Alloy 28 has shown good resistance to corrosion in environments presenting H₂S. However, it showed limited resistant to sulphide stress cracking [32].

Alloys 825, 2550, 625 and C-276: These alloys have provided good corrosion resistance in environments containing NaCl and CO₂; however, they are susceptible to H₂S and high temperatures [31].

2.4 Coating in the oil and gas sector

The coating is used to protect the surface of a metal from the action of its immediate corrosive environment; this ensures the preservation of the service conditions of the metal (both the physical & mechanical properties). The main purpose of using a good coating with very good mechanical properties is commonly more functional and economical rather than choosing a more corrosion-resistant but very expensive material [33]. There are several ways with many coatings functioning to achieve the protection of a metal, such as; a barrier coating which prohibits the corrosive environment from approaching the main metal, a noble metal coating which ensures that the base metal is passivated; and an inhibitor coating that reduces the reactions of the electrode [33]

The corrosion problem and its protection in oil and gas industry tools and equipment have become more vital and urgent. This refers to the increase in oil and gas industry improvement, specifically offshore, which includes severe corrosive components. In addition, intensive oil refining techniques, production and transference enhance the corrosion rate of oil and gas equipment. Therefore, more effective methods have been produced to reduce the corrosion rate and increase the lifetime of oil and gas equipment. Nowadays, industrial countries are working

to develop new anti-corrosion coatings with reasonable prices rather than improving anticorrosive steel and alloys [34].

The most common process used to protect metal or material from corrosion is insulating it from the surrounding environment, which could be achieved by using liners and coating. Historically, coatings, for example, early cold- and hot-applied tapes, early grease coatings, coal tar-based coatings, paints, asphalt coatings and epoxies are utilized outside the metallic structure, which helps to conserve the metal from any corrosive solution, which leads to deteriorating the metal [3]. Unfortunately, some of these coatings have difficulty applying on the pipe surface and, most of the time did not show a good bond on the pipe surface, causing imperfections such as pinholes and voids [35]. Furthermore, epoxies, thermosetting phenolic and thin film coatings are the most commonly applied to protect tubes and pipelines in the oil and gas field [3]. Nowadays, non-metallic and metallic coatings are used on metal surfaces to prevent wear and corrosion [36].

2.4.1 Thin film technology:

Thin-film technologies produce and manipulate thin layers ranging from a few microns in thickness to single atomic layers. In this process, thin films are typically deposited on existing surfaces using molecular or atomic physics and chemistry processes. For instance, physical vapour deposition (PVD) of thin films is based on energetically removing atoms from a liquid or solid and depositing the same on a nearby surface [37]. As a popular aspect of metallurgy and materials science, thin-film technology has numerous surface treatment applications that aimed at improving a wide range of material properties, such as heat, wear, mechanical strength, scratch resistance, frictional resistance, and reducing oxidation and corrosion in many metals. This technology has driven progress in many scientific fields, such as the surface coating of functional materials used in various applications like optics, steel tools, computer chips, space technology, microelectronics, nuclear, and the medical industry [38, 39].

2.5 Amorphous materials

Amorphous metals are non – crystalline with a disordered atomic-scale structure, unlike crystalline with high atoms arrangement. Amorphous metals (also well-known as glassy metal or metallic glass) are usually metallic alloys rapidly quenched from the liquid state at room temperature to avoid a significant degree of crystallization via different techniques such as; arc melting or vapour deposition [40]. In addition, metallic alloys normally include three or more components based on only one element with a higher percentage, for instance, Fe, Cu and Zr [41].

By avoiding the crystal defects, a material will improve mechanical properties to produce the next properties: toughness which is more fracture resistant than ceramics; hardness (appropriate for surface coatings); and strength which is twice the stainless steel in many cases. Also, the no-existence of grain boundaries improves the wear and corrosion resistance of the material [42].

Metallic alloys are one of the new materials applied in corrosion. Although the amorphous structure is potentially thermodynamically unstable, it shows homogeneity in the chemically compositional because of the absence of defects acting as chemically active sites. It has no defects in the structure like grain boundaries and no heterogeneity in the composition such as; segregates and precipitates. As a result, it can be expected that the corrosion susceptibility of amorphous metals is lower than that of crystalline metals [43].

Additionally, grain boundaries represent weak points of less than optimal atomic packing, in which cracks could form, and corrosion begins [42]. Metals have atomic arrangements as long order or short-range order. Repeated atomic arrangements in one place constitute a grain, and if these orientations are changed over a distance, they are called grain boundaries. Hence, grain

boundaries' properties differ from grains' because of the orientation of the atomic structures. Moreover, as grain boundaries increase (therefore, grain size reduces), mechanical properties (toughness, deformation and strength) are enhanced. However, corrosion and resistance in different environments reduce. Furthermore, grain boundaries have higher energy than grains and consequently are favourably susceptible to chemicals [29]. However, traditional amorphous alloys have some limitations, such as relatively high price (need for lab-grade elements, high-price consumables); as it has been mentioned, they are based on a major element, as well as very brittle in tension [44].

2.6 High entropy alloys (HEAs)

HEAs are typically considered solid solution alloys comprising five or more elements of similar or near-similar atomic percentages. The high entropy concept provides a different way to develop advanced materials with high properties that may not be possible with traditional alloys using a single dominant element [45]. The concept of large mixing entropies of solid solution phases is to improve their stability. [35]. Moreover, HEAs are composed of various metals mixed in required rations such as Fe, Al, K, Zn, Ni, Co, Cu, & Mg [46].

HEAs were designed to have excellent physical and mechanical properties, including strength similar to some metallic glasses and structural ceramics, high toughness exceeding the purest alloys and metals, superconductivity and high corrosion resistance [47]. Yeh et al. ascribed HEA properties to predominantly four essential effects: the cocktail effect; which can improve the properties via alloying, and the high-entropy effects; which provide the thermodynamics for stabilizing single-phase solid solutions. In addition, the severe lattice distortion impact, which offers excess strength, and the sluggish diffusion effect, impedes the formation of second-phase nuclei out of a single-phase solid solution, hence assisting the development of Nano-precipitates [47].

2.6.1 Compositionally Complex alloys

As mentioned above, high entropy (HE) is a term used to refer to the process of producing near equiatomic/ equiatomic ratio and single-phase microstructures. However, the concentration on producing a single-phase microstructure restricts the performance in many engineering applications [48]. Furthermore, a new branch is known as compositionally complex alloys or the complex concentrated alloys (CCAs) or multi principal element alloys (MPEAs), also known as multi-phase high entropy alloys. These alloys can have more than one phase and allow the elemental concentrations above 35 at. % without concerning the amount of entropy [49-51]. As well as, (CCAs) alloys can be ternary CoCrNi [52] and quaternary CoFeNiSi_{0.5} [53]. Many alloy compositions are subjected to form a secondary phase by adding some elements. Complex concentrated alloys (CCA) can increase the compositional area to provide numerous opportunities to use in different engineering applications and reach desired properties, such as adding a certain amount of an element to enhance the corrosion resistance of an alloy [54].

2.6.2 High entropy thin films (HEAs TF)

Most HEA alloys have been reported to be prepared via arc melting & casting. However, the limited sizes of arc melt synthesized HEAs, besides the high cost, which could be higher compared to the traditional alloys owing to the need for some costly elements, such as Ti, Ni, Nb, Co, V and W. Researchers are showing interest in the performance of high entropy coatings and films on low-cost metal substrates. A film is a thin layer of material ranging from a few micrometres (monolayers) to several micrometres. In contrast, a coating is a substance used to cover the surface of an object (a coating is often thicker than a film). Films may share similar features with coatings regarding their science and application [55-57]. So far, several processes have been developed to fabricate high entropy coatings and films, such as magnetron sputtering, laser cladding, plasma-transferred arc cladding, spraying, electrodeposition, etc.

Studies have shown that high entropy coatings and films exhibit excellent physical and mechanical properties, for instance, good wear resistance, high-temperature resistance, high hardness, corrosion resistance, elastic modulus, and attractive magnetic and electrical features [58].

2.6.3 The corrosion resistance of HEAs

In terms of corrosion, the fundamental theory is that incorporating certain alloying elements, for instance, Ni, Mo and Cr, leads to a dense porous free layer on the surface that keeps the alloys from corrosion. The improved corrosion-resistant capability results in their extensive usage in industry. [59]. The alloying process has limitations, ending up with intermetallic compounds, carbides, and nitrides, affecting the alloys' corrosion behaviour. Additionally, the ability to withstand the temperature of conventional alloys is very low, leading to corrosion and mechanical properties deterioration [59].

HEAs and CCAs are synthesised using induction, vacuum arc melting, magnetron sputtering, and ion beam sputtering. These alloys, in numerous cases, have shown good corrosion resistance in various solutions such as NaCl, H₂SO₄ and HCl, and at different strengths, such as 0.1, 0.5 and 0.6 M or in percentages. Some of the corrosion resistance of HEAs & CCAs studies are provided below:

2.6.3.1 *The corrosion resistance of HEAs in sodium chloride environments.*

The first corrosion test of high-entropy alloys was on FeCoNiCrCu_x alloys with different ratios of Cu (x= 0-1 at. %) content prepared by arc melting. The corrosion tests were conducted using by electrochemical polarization technique. The electrolyte was 3.5 at % (0.6 mol/L) NaCl solution at normal temperature and pressure. FeCoNiCrCu_x alloys in 3.5% NaCl solution were plotted using the potentiodynamic polarization curves in figure 2.4 below, as well as 304 stainless steel curve is plotted as a reference for the comparison [60].

The results corresponding to FeCoNiCrCu and FeCoNiCrCu_{0.5} show less passivation region, which are narrower than FeCoNiCr alloy without the addition of Cu and 304L stainless steel as confirmed from corrosion parameters; corrosion potential and corrosion current density ($E_{\text{corr}} = -0.33 \text{ V}$, -0.29 V , -0.26 V , and -0.25 V respectively, and, $i_{\text{corr}} = 1.32 \times 10^{-6} \text{ A/cm}^2$, $7.23 \times 10^{-7} \text{ A/cm}^2$, $3.15 \times 10^{-8} \text{ A/cm}^2$ and $6.01 \times 10^{-7} \text{ A/cm}^2$ respectively). In addition, it is observed from the polarization curves that the higher the Cu content, the higher the current value. This is due to Cu segregation in interdendritic, which causes a non-protective passive film on the surface. Therefore, FeCoNiCr alloy without the addition of Cu has high passivity and high corrosion resistance, as well as more resistance to corrosion than 304L stainless steel in 3.5% NaCl [60].

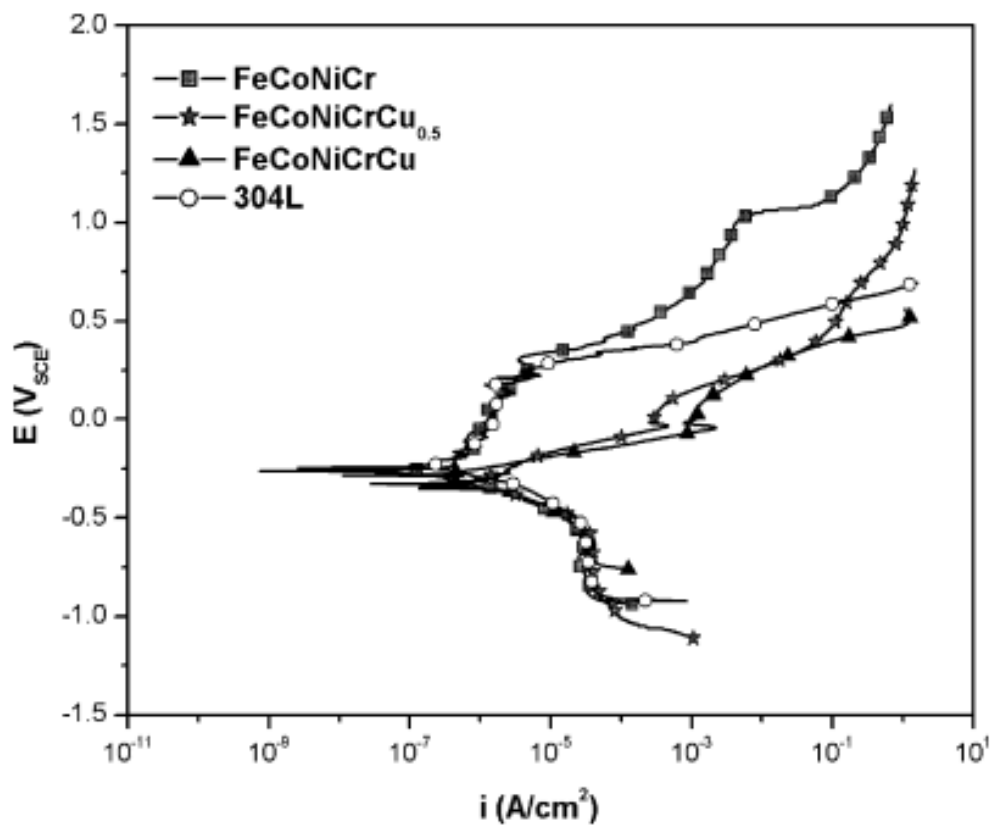


Figure 2-4: Polarization curves of FeCoNiCrCu_x alloys and 304L in NaCl solution at room temperature [60].

An experiment on $\text{Hf}_{0.5}\text{Nb}_{0.5}\text{Ta}_{0.5}\text{Ti}_{1.5}\text{Zr}$ refractory HEA was synthesised using an arc melting furnace. The analysis of microstructure showed that the alloy has a single-phase structure. The corrosion test of $\text{Hf}_{0.5}\text{Nb}_{0.5}\text{Ta}_{0.5}\text{Ti}_{1.5}\text{Zr}$ alloy in comparison with stainless steel type 316L was conducted by potentiodynamic polarisation technique in 3.5 wt. % (0.6 mol/L) NaCl using a three-electrode cell. The test was performed at normal temperature and pressure. Although the result showed that 316L has better corrosion potential $E_{\text{corr}} = -0.46 \text{ V}$ than $\text{Hf}_{0.5}\text{Nb}_{0.5}\text{Ta}_{0.5}\text{Ti}_{1.5}\text{Zr}$ alloy -0.73 V . However, $\text{Hf}_{0.5}\text{Nb}_{0.5}\text{Ta}_{0.5}\text{Ti}_{1.5}\text{Zr}$ alloy showed less corrosion current density $I_{\text{corr}} = 3.4 \times 10^{-7} \text{ A/cm}^2$ than 316L $1.78 \times 10^{-6} \text{ A/cm}^2$. Also, $\text{Hf}_{0.5}\text{Nb}_{0.5}\text{Ta}_{0.5}\text{Ti}_{1.5}\text{Zr}$ alloy displayed a very large passivation area than 316L. This ascribed to the single-phase formation and elements distributed homogeneously allowed to form a constant passive-layer which improved the corrosion performance of $\text{Hf}_{0.5}\text{Nb}_{0.5}\text{Ta}_{0.5}\text{Ti}_{1.5}\text{Zr}$ HEA [61].

An experiment on an equiatomic AlFeCrNiMo (HEA) coating; was fabricated by the magnetron sputtering technique. The coating thickness measured to be about $1.5 \mu\text{m}$. And the microstructure analysis showed that the AlFeCrNiMo coating has a single-phase structure. The potentiodynamic polarization method using a three-electrode cell was used to examine the corrosion behaviour of AlFeCrNiMo HEA against stainless steel type 304 ss. The corrosion tests were conducted in artificial sea water at normal temperature and pressure. The results showed that AlFeCrNiMo HEA coating has a higher corrosion potential $E_{\text{corr}} = -0.04 \text{ V}$ than 304 ss -0.31 V .

Moreover, the high entropy coating has less corrosion current density $i_{\text{corr}} = 2.04 \times 10^{-7} \text{ A/cm}^2$ than 304 stainless steel $7.6 \times 10^{-6} \text{ A/cm}^2$. Hence, the equiatomic AlFeCrNiMo high entropy alloy coating has better corrosion resistance than 304 stainless steel. This could refer to the

elements Mo, Ni, Cr and Al, which have increased the electrode potential. As a result, forming a dense layer protects the surface from corrosion [62].

A study on equiatomic CrMnFeCoNi HEA coating was synthesised via mechanical alloying. The coating was performed on a steel substrate type Q235. The coating microstructure was analysed to be a single-phase solid solution. The coating thickness was measured to be 180 μm and was successfully bonded on the substrate. Potentiodynamic polarisation technique using a three-electrode cell setup to evaluate corrosion performance of the CrMnFeCoNi HEA coating compared with Q235 steel. The corrosion tests were performed in 3.5 at. % NaCl to simulate the sea water environment under normal temperature and pressure. The CrMnFeCoNi HEA coating showed better corrosion potential than Q235 steel ($E_{\text{corr}} = -0.06 \text{ V}$ and -0.19 V , respectively). In addition, less corrosion current density was observed in HEA coating $i_{\text{corr}} = 9.81 \times 10^{-6} \text{ A/cm}^2$ compared to $1.05 \times 10^{-5} \text{ A/cm}^2$ in Q235 steel. Therefore, the equiatomic CrMnFeCoNi high entropy alloy coating possesses good corrosion resistance compared to Q235 steel in the studies solution. This might refer to the cocktail effect as the high entropy coating contains elements Cr, Co and Ni, which can form a passive protective layer on the surface [63].

An examination of AlCoFeNiTiZr HEA films was prepared via magnetron sputtering. The films were synthesised on silicon substrates with different elements ratios: (Fe-Co-Ni)₁₅ (Al-Ti-Zr)₈₅, (Fe-Co-Ni)₂₀ (Al-Ti-Zr)₈₀ and (Fe-Co-Ni)₂₅ (Al-Ti-Zr)₇₅. The microstructure characterisation showed that the films displayed a multi-phase structure (FCC solid solution with an amorphous phase). The thickness of the films was measured to be around 400 nm. The corrosion test of high entropy alloy films was done by The potentiodynamic polarisation technique via three-electrode cell workstation. The tests were performed in 3.5 at % NaCl solution at ambient temperature and normal atmospheric pressure. The results showed that (Fe-Co-Ni)₂₅ (Al-Ti-Zr)₇₅ has a higher corrosion potential $E_{\text{corr}} = -0.26 \text{ V}$ than (Fe-Co-Ni)₂₅ (Al-

Ti-Zr)₇₅ with -0.46 V, and (Fe-Co-Ni)₂₀ (Al-Ti-Zr)₈₀ with -0.28 V. Moreover, (Fe-Co-Ni)₂₅ (Al-Ti-Zr)₇₅ film exhibits less corrosion current density than (Fe-Co-Ni)₂₀ (Al-Ti-Zr)₈₀ and (Fe-Co-Ni)₂₅ (Al-Ti-Zr)₇₅ ($i_{\text{corr}} = 6.2 \times 10^{-8} \text{ A/cm}^2$, $2.04 \times 10^{-6} \text{ A/cm}^2$ and $5.86 \times 10^{-7} \text{ A/cm}^2$ respectively). As a result, (Fe-Co-Ni)₂₅ (Al-Ti-Zr)₇₅ exhibits high corrosion resistance and is better than the other two HE alloys film. This is due to the increase of (Fe-Co-Ni) amount, which reduced dislocation, vacancy grain boundary segregation, and increased the formation of an amorphous phase. Hence, a large protective passive area increased the corrosion resistance to (Fe-Co-Ni)₂₅ (Al-Ti-Zr)₇₅ HEA film [64].

2.6.3.2 *The Corrosion resistance of HEAs in acid liquids environments.*

An experiment on multi-principal elements AlCrFeNiCuTi equiatomic alloy was prepared by powder metallurgy using a vacuum furnace. The microstructure analysis shows an occurrence of element segregation, and the alloy has two phases. Furthermore, the potentiodynamic polarization technique was examined in 0.5 mol/L H₂SO₄ solution using a three-electrode method of an electrochemical cell against 304 ss at normal temperature and pressure. The result acquired by linear fitting displays that AlCrFeNiCuTi alloy has good corrosion resistance with corrosion density $I_{\text{corr}} = 8.65 \times 10^{-4} \text{ mA/cm}^2$ and corrosion potential $E_{\text{corr}} = 0.042 \text{ V}$. And better than 304 stainless steel with corrosion current density $I_{\text{corr}} = 2.40 \times 10^{-2} \text{ mA/cm}^2$, and corrosion potential $E_{\text{corr}} = -0.312 \text{ V}$. This may be due to the high corrosion resistance of titanium which can improve the corrosion performance of the AlCrFeNiCuTi equiatomic alloy in 0.5 mol/L H₂SO₄ [65].

A study on CuCrFeNiMn high entropy alloys with different content of Cu, CuCr₂Fe₂Ni₂Mn₂ and Cu₂CrFe₂NiMn₂ was fabricated via a vacuum arc melting furnace. The microstructure characterisation showed that the alloy with low Cu amount possesses FCC solid solution structure with low degree of elements segregation. In contrast, the alloy with high content of Cu displays a mix of two phases (FCC & BCC) and more elements segregation. The corrosion

tests of HE alloys compared to SS304 were performed using a three-electrode cell setup in 1 M H₂SO₄ at room temperature and atmospheric pressure. The corrosion parameters obtained from the potentiodynamic polarization technique showed that CuCr₂Fe₂Ni₂Mn₂ alloy with low amount of Cu has less corrosion current density $I_{\text{corr}} = 2.09 \times 10^{-6} \text{ A/cm}^2$, $4.02 \times 10^{-5} \text{ A/cm}^2$ and $5.10 \times 10^{-5} \text{ A/cm}^2$. And higher corrosion potential $E_{\text{corr}} = -0.73 \text{ V}$, -0.90 V and 0.86 V , respectively. Consequently, CuCr₂Fe₂Ni₂Mn₂ HEA exhibits good corrosion resistance and is better than CuCr₂Fe₂Ni₂Mn₂ alloy and 304 ss in 1 M H₂SO₄ solution. This is because the uniform structure of CuCr₂Fe₂Ni₂Mn₂ HE alloy with less elements separation could enhance the passivation area, enhancing the corrosion resistance [66].

An examination of an equiatomic CoNiCuFeCr HEA coating synthesised by the Plasma Transferred Arc Cladding Process. The HEA coating was deposited on Q235. The microstructure analysis showed that the coating has an FCC single-phase structure. The Potentiodynamic polarisation method using a three-electrode workstation was used to perform the corrosion test of CoNiCuFeCr HE Alloy coating compared with 304 ss. The corrosion tests were conducted in 1N HCL solution at normal temperature and open to the air. The results displayed that HEA coating has a higher and better corrosion potential $E_{\text{corr}} = -0.235 \text{ V}$ than 304 ss with -0.45 V .

Moreover, less corrosion current density $I_{\text{corr}} = 8.99 \times 10^{-6} \text{ A/cm}^2$ than 304 ss with $7.29 \times 10^{-4} \text{ A/cm}^2$. Therefore, CoNiCuFeCr HEA coating shows good corrosion performance compared to SS304 in 1N HCl. This could be due to the chemical composition effect of the HEA alloy and the elemental effects (Cr, Ni and Co) that led to a passive layer formation which shields the coating from further corrosion [67].

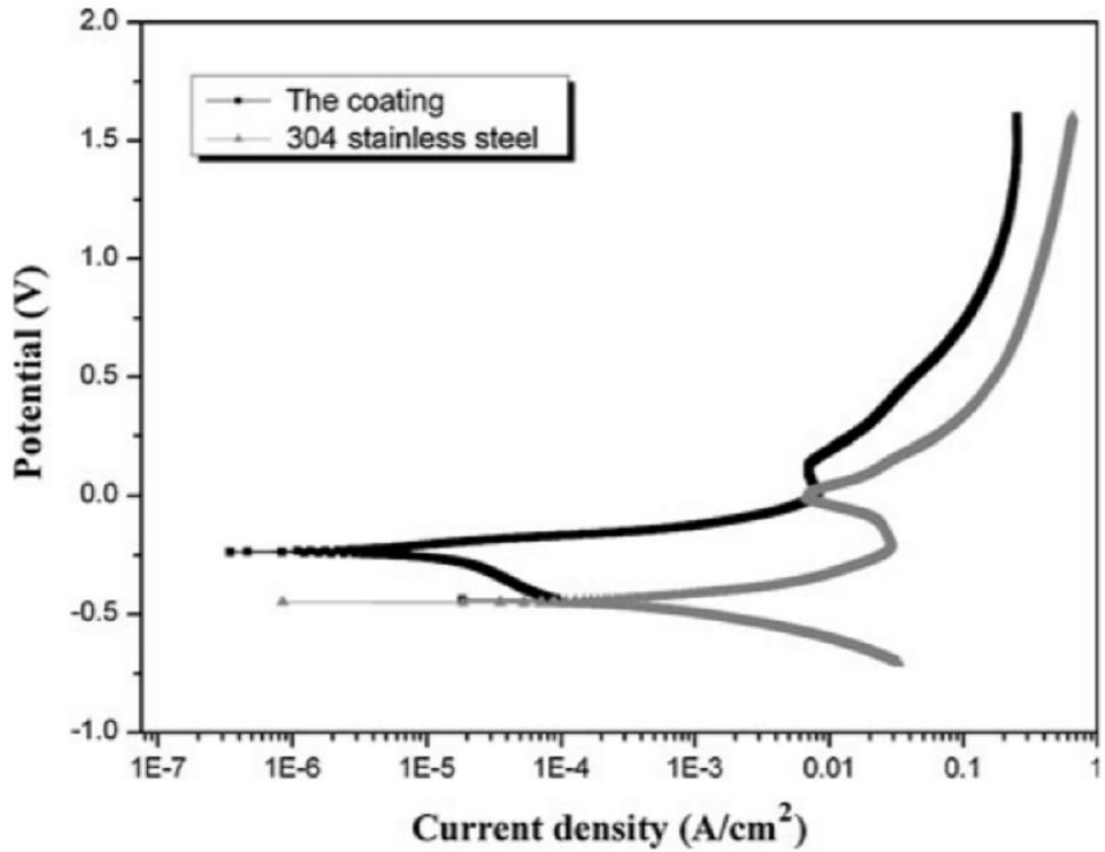


Figure 2-5: Potentiodynamic polarization curves of CoNiCuFeCr equiatomic alloy coating and 304 ss in 1 N HCL solution [67].

An examination of $\text{Al}_2\text{CrFeNiCoCuTi}_x$ HEA coatings was produced by laser cladding. The coatings were produced with different amounts of Ti_x ($X = 0.0, 0.5, 1.0, 1.5, 2.0$) on Q235 steel substrates. The thickness of the coatings was measured to be about 1 mm. the microstructure characterisation showed the high entropy coatings possess a mix of two phases (FCC + BCC structure). A three-electrode cell setup used the potentiodynamic polarisation technique to evaluate the corrosion test. $\text{Al}_2\text{CrFeNiCoCuTi}_x$ HEAs coatings were tested against Q235 steel in 0.5 mol/L Nitric acid (HNO_3) under normal pressure and temperature. The results showed that $\text{Al}_2\text{CrFeNiCoCuTi}_{x=2}$ exhibits higher corrosion potential and is better than where $X = 0.0, 0.5, 1.0, 1.5$ and Q235 steel, $E_{\text{corr}} = -0.15, -0.18, -0.30, -0.33, -0.30$ and -0.35 respectively. Also, less corrosion current density $I_{\text{corr}} = 2.7 \times 10^{-3}, 3.8 \times 10^{-2}, 2.2 \times 10^{-2}, 7.3 \times 10^{-3}, 4.4 \times 10^{-3}$ and 2.4×10^{-3} respectively.

¹ respectively. This is due to increasing the amount of Titanium element in $\text{Al}_2\text{CrFeNiCoCuTi}_x$. Hence, the high entropy coating where $\text{Ti} = 2.0$ has the best corrosion resistance in 0.5 mol/L Nitric acid [68].

Although some HEA or complex concentrated alloys with multi-phase structures and elements segregation showed good corrosion resistance. However, corrosion is favoured to happen at grain boundaries and elements separation. Hence, when microstructure is more homogenous, like smooth grain boundaries, equated grain shape, and uniform composition with no element segregation or phase separation will enhance the resistance to corrosion of high entropy alloys [69].

As discussed in the corrosion resistance of high entropy alloys section, different high entropy alloys showed corrosion resistance ranging from good to very good. However, in many cases, early pitting corrosion occurs as same as in alloys used in oil and gas fields, such as 304 SS and different Cr and Ni-based alloys. This pitting is not preferred in oil and gas fields as it leads to leaks, consequently leading to a failure in the application. Therefore, high entropy thin film alloys in an amorphous structure are provided as a solution to early pitting issues.

2.6.4 Amorphous HEAs

Furthermore, HEA can be mixed with metallic glass MG (amorphous) or bulk MG to produce metallic glassy alloys with five or more core components in equal or near-equal atomic ratios; these alloys are named; high entropy amorphous or metallic glasses high entropy. These alloys would have higher mixing entropy than conventional metallic glassy ones based on a single dominant element. In addition, developing MGs with high entropies will produce materials with unique mechanical, physical, and chemical properties. And also high corrosion resistance [41]. These types of new materials have excellent properties such as soft magnetic and mechanical properties $\text{Fe}_{25}\text{Co}_{25}\text{Ni}_{25}(\text{P}, \text{C}, \text{B}, \text{Si})_{25}$ [70], high fracture strength

Ti₂₀Zr₂₀Cu₂₀Ni₂₀Be₂₀ [71]. However, there is a lack of studying corrosion properties and thin films.

An experiment presents the corrosion behaviour of HEA with the chemical compositions (wt. %) compared with 304S stainless steel. The high entropy alloy used was Cu_{0.5}NiAlCoCrFeSi in a non-equal mole. The alloy was prepared using arc melting from pure elements under a purified Ar gas at a normal temperature (~25°C). The high entropy had a nearly amorphous structure, as XRD confirms it. The test was performed using the polarization method with a three-electrode cell [72].

The polarization curves of HEA and 304 ss results showed that the HEA exhibited better corrosion potential (E_{corr}) (−0.53 V) than the SS304 (−0.59 V). Moreover, the HEA presented lower corrosion current density (I_{corr}) (3.16×10^{-6} A/cm²) than the SS304 (4.37×10^{-6} A/cm²). Therefore, low Cu content and the elemental segregation degree lead to good corrosion resistance [72].

2.6.5 Hardness and Nano-indentation of HEAs

Hardness can be defined as a measure of a material's ability to resist plastic deformation, such as scratching, wear and indentation when applying a load. [73]. Nano-indentation, also known as depth sensing indentation, is a method used to measure and test very small volumes of mechanical properties of materials (specifically, thin films & coatings) where the hardness impression could be determined. [74, 75]. There are different ways to measure hardness in labs, for instance, Vickers Hardness to measure microhardness and Nano-indentation tester to measure Nano-hardness (as described in chapter 3) [76]. Increasing a material's hardness is important for numerous materials engineering applications. High entropy alloys, from hardness point of view exhibited very good, excellent, and high hardness in many cases:

A study of the hardness of CoCrFeNiC_x high entropy alloy with different amounts of carbon (X= 0, 0.05, 0.1, 0.2, 0.3, and 0.5) was synthesised by a vacuum arc melting furnace. The microstructure showed that the alloys have a matrix FCC structure with carbide phases, which later increases with the amount of C. The produced alloys were subjected to hardness tests using the Vickers Hardness method under a 500g load for 15 seconds. The results showed the hardness improved from 133 HV to 335 HV as the carbon content increased from 0 to 0.5. The reason could refer to increasing carbon content, which enhanced the hardness of CoCrFeNiC_x HE alloy [77].

An equiatomic CoCrFeNi HEA thin film was prepared via the magnetron sputtering technique. The HEA film was deposited on a silicon substrate with a thickness of around 3.97 μm . The analysis of the microstructure displayed that the HEA film has an FCC single phase and uniform structure. The Nano-hardness was measured using a Nano-indentation tester. The maximum load was five mN to avoid the substrate impact. The high entropy film displayed high hardness and YM values of 8.5 GPa and 161.9 GPa, respectively. This could be attributed to the lattice distortions effect, which is very influential in preventing current movement, and to the abundant nanocrystalline and Nano-twin boundaries [78].

FeCoNiCuVZrAl high entropy alloy film with equiatomic ratio was prepared by direct current magnetron sputtering. The microstructure characterisation showed the HEA film possesses an amorphous structure. The thickness of the high entropy film was measured to be about 1.5 μm . A Nanoindenter instrument was used to measure the hardness of the HEA film. The results showed that the film has a hardness of 8.6 GPa, and young's modulus of 153 GPa. This is due to the effect of the formation of a dense and smooth amorphous structure with pore-free film. Also, the effect of the extensive lattice distortion [79].

2.7 Summary

This chapter provided a relevant literature review of the proposed work, starting with an explanation of the corrosion process, corrosion types, materials and coating used previously in the oil and gas sector. Then, thin film technology and traditional amorphous materials with their drawbacks were discussed as an immediate solution to the corrosion problem. After that, high entropy alloys in the shapes of bulk or coating alloys were provided as a general solution to the corrosion issue. Some experiments and studies were discussed accordingly. These alloys showed properties ranging from good to excellent, including corrosion resistance in sodium chloride and acids. However, these high entropy alloys were reported as crystalline materials. Few bulk high entropy alloys were reported to have an amorphous structure and were only meant to study mechanical properties.

From a corrosion point of view, the high entropy coating method has been provided as an additional feature to improve the corrosion resistance of high entropy alloys. On the other hand, from the economic perspective, bulk high entropy alloys prepared by arc melting or casting are considered higher costs. However, thin film high entropy alloys prepared by deposition techniques such as magnetron sputtering or ion beam sputter deposition could solve this problem at a lower cost. Another point, very few studies reported the deposition of high entropy alloy on steel. However, these alloys were prepared by alloying and laser cladding techniques. They showed crystalline structures such as CrMnFeCoNi deposited on Q235 steel via mechanical alloying FeCoCrAlNiTi_x deposited on 304 SS synthesised by laser cladding method.

Therefore, there is a lack of synthesising and performing corrosion tests of coating amorphous high entropy alloys. Moreover, performing corrosion tests of amorphous HEA thin films in crude oil has not been considered before, and that is what we aim to achieve in this project.

3 Chapter3: Materials and Methods

3.1 Vacuum arc melting furnace

Vacuum arc melting is a method for producing chemically and mechanically homogeneous metal ingots. Vacuum Arc Melting is used to melt metals to form different alloys. In vacuum arc melting, the melting is performed in the argon atmosphere by evacuating the chamber first and then injecting the argon gas back into the chamber [80]. A schematic depiction of the vacuum arc melting is displayed in fig. 3.1.

Basic Principle: A standard Tungsten Inert Gas (TIG) welding device was employed as the power supply. Heat generation is achieved by striking an electric arc between the metal and the electrode to dissolve the metals in the crucible and form an alloy. A DC power supply was connected to the crucible and electrode to produce the electric arc. The metal is melted in a copper crucible that is kept cool by water. The electrode is pulled down during the melting process to maintain the arc length. The melting process is then steadily repeated to improve the alloy's compositional uniformity [81].

Features of Arc melting: the temperature could reach > 3000 degrees Celsius and is regulated by altering the electrical powder. The hearth has five melting pots (crucibles); therefore, it can produce five alloys in a single evacuation. There are four small crucibles and one large. Approximately 80g of metals can be melted in the larger crucible and 15g in the small crucibles. A cooling system to cool the electrodes and the copper hearth [80]. Removing non-metallic impurities and dissolved gases, low macro-segregation, and high density with suitable grain structure are also some of the advantages of this approach. In addition, the vacuum environment and high temperature make it easier to remove entrapped gases and high vapour-pressure materials [72].

The high temperatures of the electric arc could cause separation of the non-metallic and high melting temperature components into smaller fractions. As a result, components made by arc

melting typically have a columnar grain structure for the small diameter parts or a mixture of columnar and equiaxed grains for the larger parts [82].

During the processing of high melting point elements like Mg, Zn, and Mn, this technique is useful; however, it is not suitable for the processing of low melting point elements that can easily evaporate because it is difficult to control the constituents; hence, it is not the right synthesis method. Despite this, the possibility of combining most elements in their liquid state in this furnace has made arc melting a useful liquid processing approach for HEA synthesis. On the other hand, heating or induction heating may be more appropriate for low melting point materials [82].

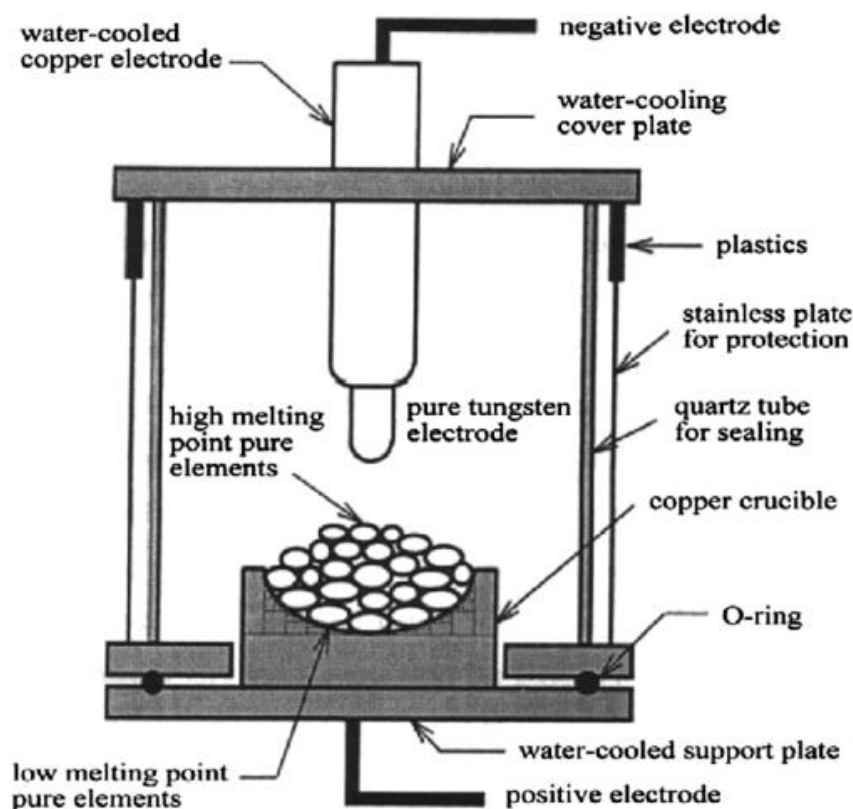


Figure 3-1: Schematic of vacuum arc melting furnace [77].

3.2 Scanning Electron Microscopy (SEM)

In an electron microscope, the voltages are applied from 2-40 keV in an electron gun, from which the incident electrons are accelerated and focused by magnetic lenses. Due to this, the incident electrons have less wavelength, and a narrow beam is formed, which is helpful for imaging materials [83].

SEM is a form of electron microscopy where the surface of a sample is scanned by focusing an electron beam on the area of interest to acquire the surface images. During the scanning, the interaction of the electron beams with the sample atoms produces different signals that provide relevant sample information, like the composition and topography of the surface [84].

Figure 3.2 presents a schematic drawing of the scanning electron microscope. The “electron beam is scanned in a raster scanning pattern to form an image, and its position is combined with the detected signal. Deflection coils within the objective lens raster the electron beams over the material, resulting in image creation. The astigmatism corrector, also known as a stigmator corrector, is placed in the objective lens and uses a magnetic field to eliminate electron aberrations. The electron beam cross-section must be circular upon striking the sample; however, the stigmator normally controls this problem since it is usually elliptical.

An electron gun comprises an emission source that could be field emission thermionic filaments (a cathode). In an anode, the emitted electrons in the gun are forced from the filament's high negative potential (-20000 V) to ground potential [84].

Lenses

The electron lenses are used to generate an electron spot of <10 nm size. The lenses are vacuum-operated metal cylinders with a cylindrical holes. A magnetic field is produced inside the lens, which is then changed to focus or defocus the electron beam that passes through the hole [85]. A scanning electron microscope's (SEM) resolution is more than 1 nm. Samples can

be examined either in a high vacuum in SEM or a wet or low vacuum condition in an environmental or variable pressure SEM; samples can also be examined at a wide range of temperatures using specific instruments [85].

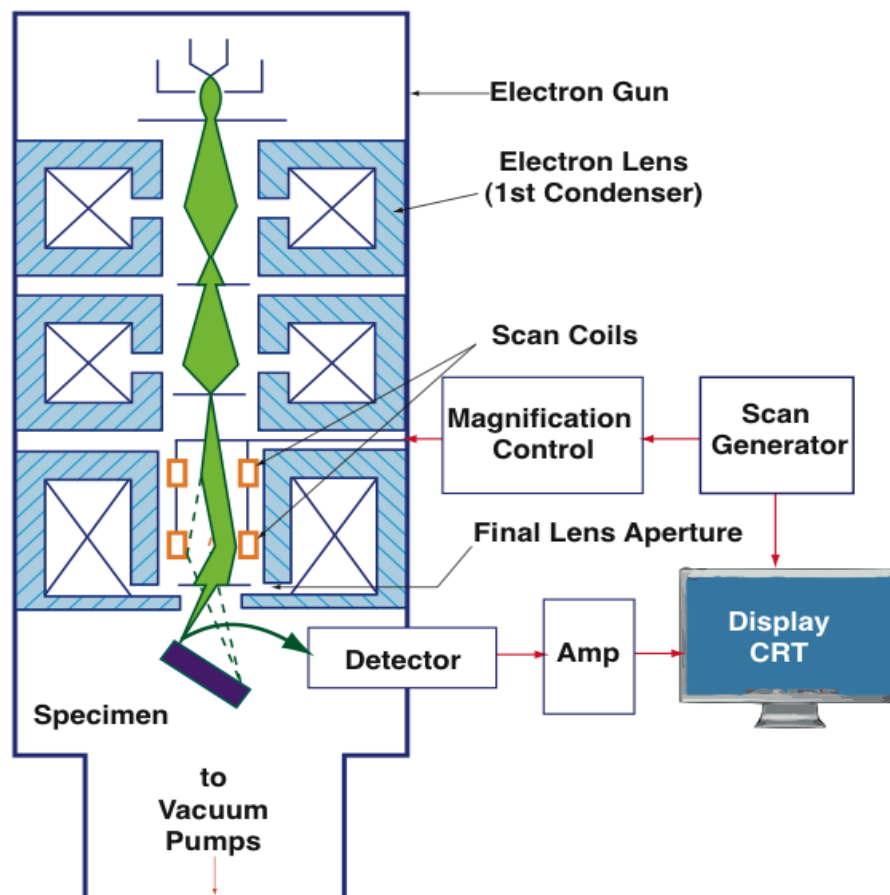


Figure 3-2: Schematic drawing of the scanning electron microscope [86].

3.2.1 Signals available in the SEM

Different signals are generated when the incident energetic electrons interact with the sample or material; therefore, these emitted signals are collected to form images: secondary electron (SE) images, backscattered electron (BSE) and images characteristic X- rays as shown in fig. 3.3 [83].

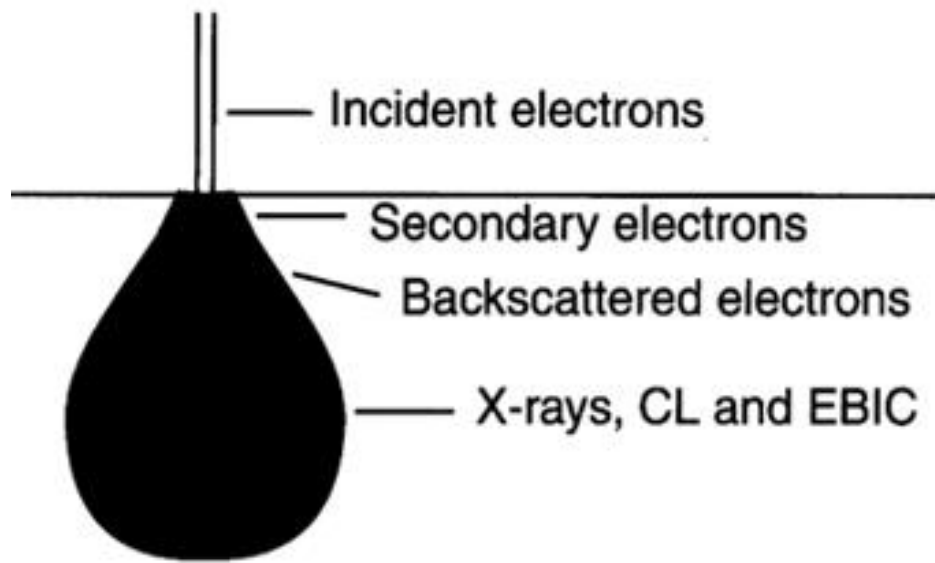


Figure 3-3: different types of imaging modes [83].

3.2.2 Secondary Electron (SE) images

Secondary electrons are knocked out of their orbits around an atom from the sample due to energy transfer from the incident energetic electrons. These provide the highest spatial resolution images because they can leave from an extremely shallow, near-surface material layer, and the signal arrives from an area around the magnitude of the electron probe [83].

3.2.3 Backscattered Electron (BSE) images

BSE are the incident electrons that are reflected through a large angle from the nucleus of an atom and re-appear from the specimen surface. BSEs are characteristic of the atomic number and elemental composition of the sample. These electrons arise from deeper in the specimen. Hence, image resolution is partially less than secondary electron images [83].

3.2.4 Characteristic X- rays

X-rays are generated by atoms when their inner-shell electron has been knocked off by energetic incident electrons, causing an outer-shell electron to migrate to the vacant orbit. During this movement, an electron moves from higher energy to lower energy statuses (for instance, from L to K, then M to L) till the electron refills all the states. At every level, emissions of x-rays are for conserving energy. The specimen's chemical composition can be obtained by measuring the energies (or wavelengths) of these x-rays. Generally, x-rays are detected using a wavelength dispersive or an energy-dispersive spectrometer. [83].

3.3 Transmission Electron Microscopy (TEM)

TEM has emerged as the primary method of determining the microstructure of materials. Transmission Electron Microscopy (TEM) uses energetic electrons when high voltage is applied to know the microstructure, crystal structure and chemical composition. The advantage of TEM over SEM is that the energy of electrons and applied voltage (up to 300 KV) are higher, allowing transmission through the material. In addition, the wavelength of electrons or electron beam size is less (up to 0.1nm), which allows interaction with the material at the atomic level, thereby producing electron diffraction, and the thickness of samples is less than 200 nm so that electrons are transparent to material [87].

The energetic electrons travel through a series of magnetic lenses and interact with the specimen (to be analysed), resulting in various emissions. Electrons experience Elastic and Inelastic scattering. Elastic scattering, where there is no energy loss with incident electrons, is used for electron diffraction (SAED) and imaging by bright field (BFTEM). In electron diffraction (ED), the electrons scatter with atoms of material that need to be analysed, producing a diffraction pattern. The imaging or microstructure is revealed by BFTEM, which works with energy absorption; thicker sample regions or regions with a higher number of atoms will appear dark whilst the background appears bright (hence the term "bright-field"). Inelastic

scattering is where there is a loss of energy and producing secondary electrons and X-rays. Collecting these inelastic electrons gives the chemical composition of the analysed material [87]. Fig. 3.4 shows a schematic diagram of transmission electron microscope components.

Bright and Dark Field

Bright-field (BF) imaging requires positioning the objective aperture with the optic axis to allow only direct beam electrons. The BF image is achieved by placing the aperture in a way that passes only transmitted electrons. This is a useful method for plain view studying the microstructure of materials (which aids in understanding the microstructure and calculating the average particle size) and cross-sectional view studies (which aids in identifying the number of multilayers). Only one powerful diffracted beam is used to create a dark field image. Hence, this technique is used for diffracted beam imaging or diffraction. This method moves the objective aperture to the diffraction beam or the incident beam tilted. A dark-field (DF) image is created when the aperture is set to allow only some diffracted electrons to flow through. Because the image is formed by collecting just the fraction of the incident beam dispersed by the sample in a specified direction, the image is generally dark except for the regions that interacted with the electron beam & scattered it in the defined direction [88, 89].

Selected area electron diffraction (SAED)

The diffraction patterns of the prepared thin-film lamellas were captured using the SAED aperture in this study. The SAED aperture was utilised to select areas of interest in the sample. The SAED aperture is placed in the image plane of the objective lens at the area of interest to produce a virtual aperture at the sample's position by only allowing electrons to pass through the virtual aperture, thereby forming the diffraction pattern [90].

Different sources can produce the emission of electrons; Field emission sources and Thermionic sources. Generally, Thermionic sources are the most common source used [89]. The source has been used in this work is Lanthanum boride (LaB_6) filament.

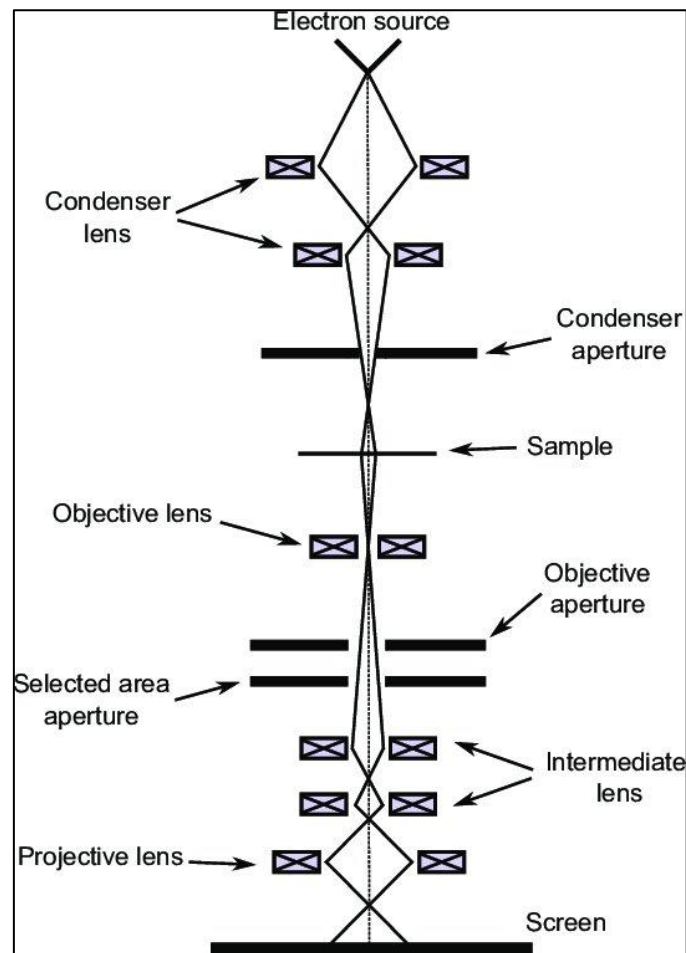


Figure 3-4: Schematic diagram of transmission electron microscope components [91].

3.4 Focused Ion Beam

The FIB equipment is like the SEM, except that an ion beam is rastered across the material instead of an electron beam. FIB uses energetic ion beams and chemical precursors to remove materials from a specified location to make TEM samples; selective material removal or material deposition by the involved chemical reaction and milling is also appropriate [89].

The material deposition is done by first choosing a precursor that will decompose into non-volatile compounds of desired properties for applications such as protecting samples from ion damage and surface layers of thin films. A precursor for FIB-induced material deposition must have enough surface sticking probability. When blasted by an energetic ion beam, it must rapidly decompose rather than sputtered away by the ion beam [92].

3.5 Ion Beam Sputter deposition:

Sputter deposition is one of the physical vapour deposition (PVD) methods used for depositing thin films on substrates. Sputtering can be defined as the ejection of atoms or particles from a target that is bombarded via energetic ions [93].

Ion Beam Sputter deposition sputtering has become a common method for deposition in several areas of industrially significant coatings for the insane; decorative coatings, corrosion-resistant coatings, low friction coatings, and wear-resistant coatings [94].

The generation of ions in Ion beam sputtering deposition is initiated by the emission of electrons from the filament and its interaction with argon gas into an ion gun, thus generating ions and creating plasma. These ions are then accelerated onto targets, thus generating atoms and depositing them on the required substrate. Synthesising the thin films can be done by composite targets or elemental targets. The required composition is achieved by adjusting the geometry of targets. In the ion beam sputter, geometrical arrangements must be made in a small order to deliver reasonable deposition rates, which could sometimes be a problem [38]. Figure 3.5 shows a schematic drawing of an ion beam sputtering system.

Ion beams are used in sputtering applications to adjust ion energy, flux, species, and incidence angle. Not only can these parameters be controlled through a wide domain, but they can also be controlled almost independently of one another. The discharged gaseous ion source is also controlled and kept away from the other parts of the deposition system [95].

Ion Sources: the ion beam sputtering process requires the delivery of as much ion current to the sputter target as possible. This is why huge ion sources (such as 10 - 15 cm diameter) are used. However, the process can also be conducted using wire filament cathodes and neutralizers made of Ta or W, with a diameter of 0.010 to 0.015'' inch [96].

Targets: the target size should be large enough to ensure the beam does not pass through it and sputter the surrounding materials. To enhance the sputtering process, the target is positioned at an angle of 45° to the ion beam [96]. Figure. 3.5 (a and b) present examples of target positioning during the deposition process used in the current work.

Contamination: thin films can be contaminated by contaminated gas, target, and walls of the deposition chamber. The use of contaminated gas can affect the composition of the thin film. Thin-film contamination can also be caused by the deposition of previously sputtered targets from the deposition chamber's walls [97]

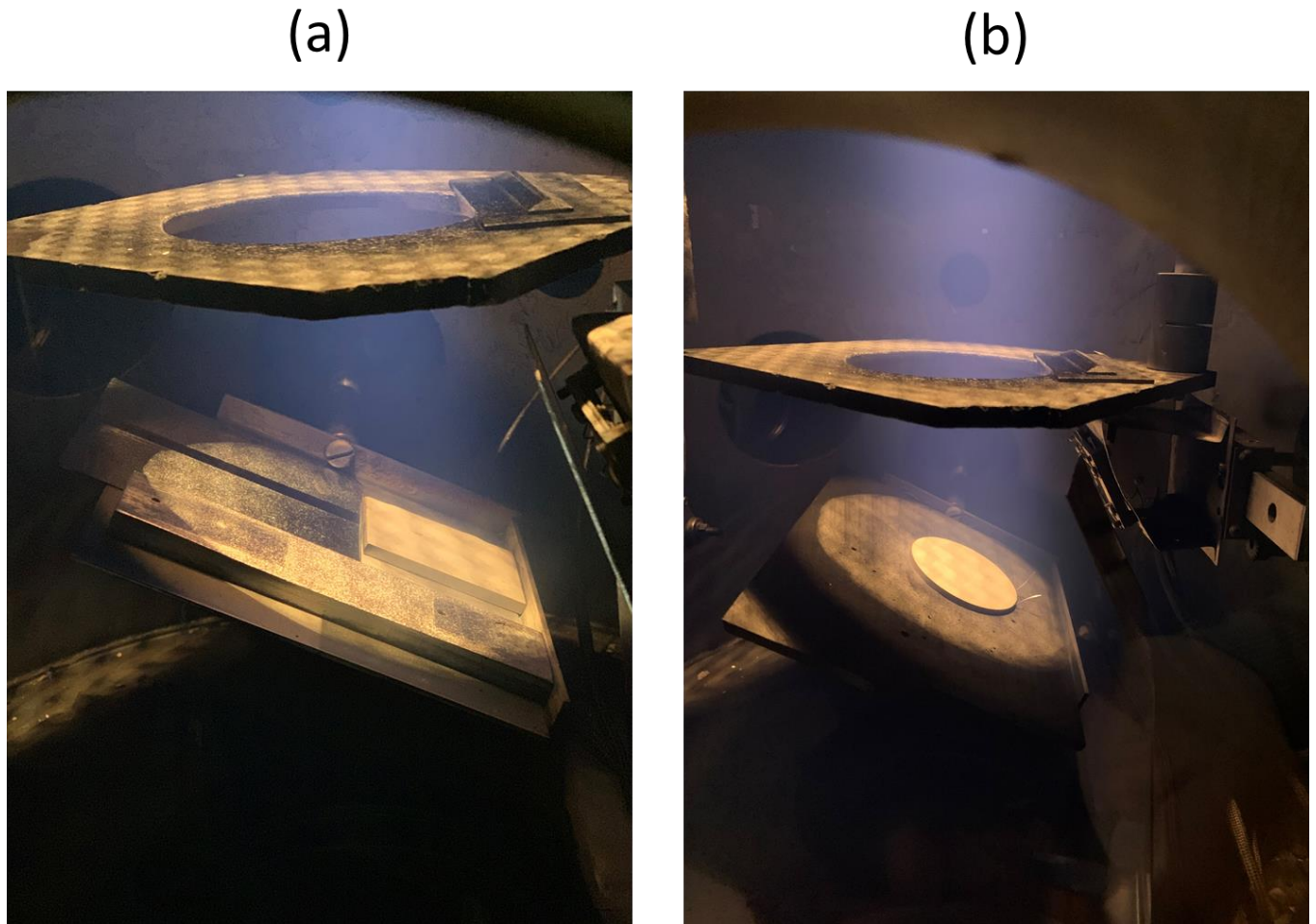


Figure 3-5: targets (a: elemental targets of Fe, Cr, Si and Nb), (b: composite target of FeCrMnNi, and C sheet) positioning during the deposition process used in the current work.

3.6 Grinding and polishing equipment

Grinding and Polishing are techniques used to prepare the bulk sample for analysis, such as microscopy, hardness, and corrosion characterisation. Grinding removes material from a specimen to clean the surface, reduce the size, remove marks, and create a flat surface. Polishing is the final process that follows the grinding that provides the sample surface with a high quality of smoothness and shines using a finer abrasive. Also, to remove the subsurface damage left from hard grinding [98]. An automatic grinding or/and polishing machine was used

in this work. Before starting the grinding and polishing process, a sample mount mould and two different moulds are prepared by mounting press machine.

3.6.1 Grinding and polishing process:

Diamond polishing abrasives are progressively smaller diamond abrasives from 30, 15, 9, 6, 3, 1, and 0.25 μm sizes (used as required) until a final structure is reached. Different factors influence the surface finish, for instance: abrasive type and size, specimen load, polish time, rotational speed, and rotational direction [98, 99].

In manual grinding/polishing, the same steps are used without a mount mould. Instead, the sample is firmly held by hand against the abrasive desk. A reference point should be chosen in the 12 o'clock position by changing the direction, the abrasive, and so on. Manual grinding is normally used when an automatic is unavailable, as it is difficult to control and time-consuming. However, it can be used for a short time polishing [99]. Figure 3.7 displays Buehler Motopol 2000 Semi-automatic Specimen Preparation Unit was used in the current study at the University of Huddersfield.

3.7 X-ray Diffraction (XRD)

This method is used to characterize the crystallographic structure and the crystalline size (grain size) and identify unknown substances' structure (phase analysis) [100].

As high-energy electromagnetic waves, X-rays have a wavelength range of 10^{-3} and 10^1 nm. X-rays are produced in sealed tubes, rotating anodes utilized in lab tools, both generate X-rays via the same technique. Electrons are emitted when the source tungsten is exposed to thermal energy in the vacuum and are accelerated by a high-potential anode. When these electrons interact, the target emits X-rays [101].

Principle: when X-ray photons approach matter, numerous interactions can occur, resulting in various scattering and absorption effects. Nevertheless, because of the periodic nature of a crystalline structure, constructive interference (when waves reinforce one another, they are in phase) or destructive interference (when Waves cancel one another, are out of phase) scattered radiation will result, leading to characteristic diffraction phenomena which can be studied to investigate the crystal structure of materials [101].

Fig. 3.8 A Bruker D2 Phaser instrument X-Ray Diffraction (XRD) was used in this work. The crystal structure was measured using the Measurement Center 4.0 software.

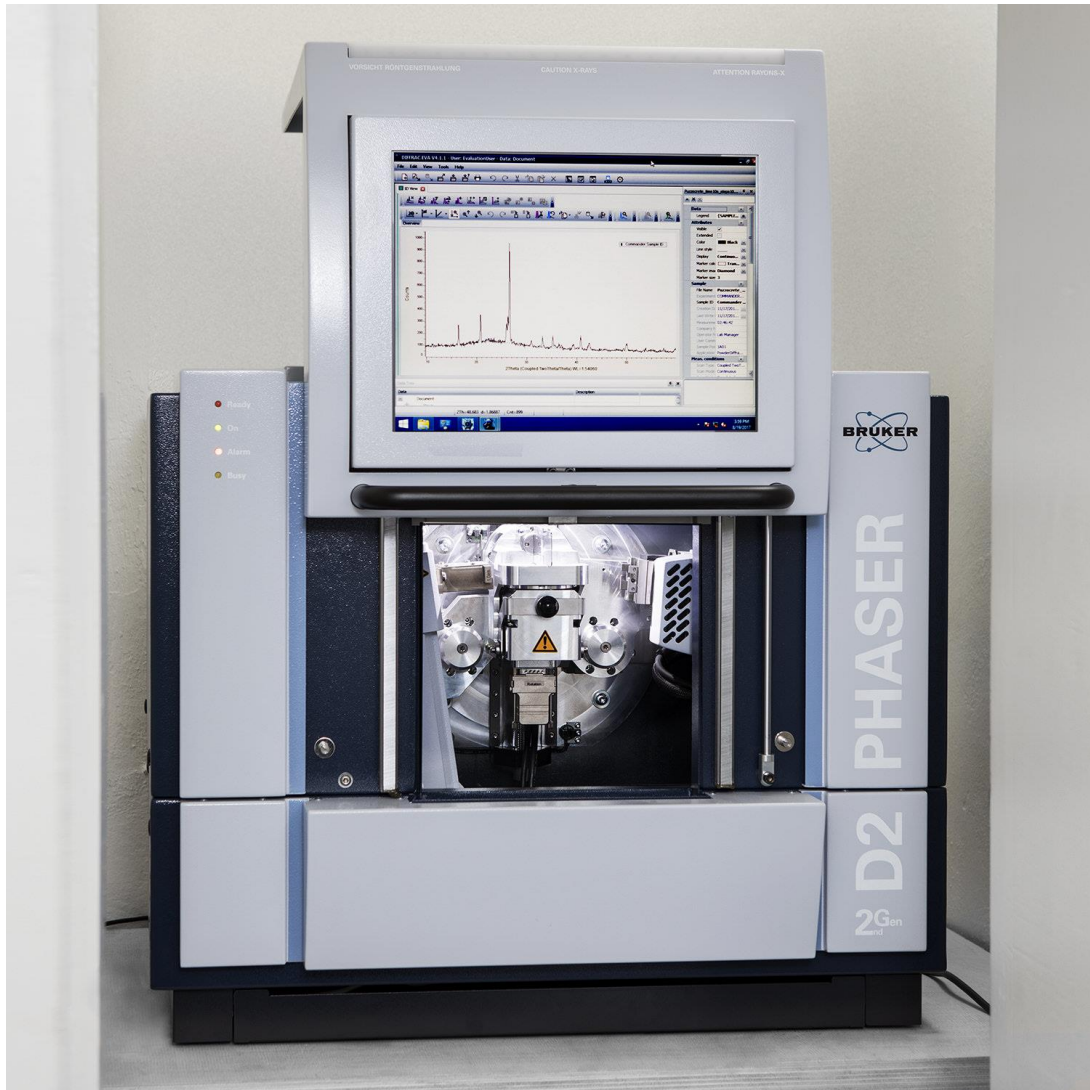


Figure 3-6: a Bruker D2 Phaser instrument (XRD) used in the current study.

3.8 Corrosion measurement

3.8.1 Electrochemical Tests

All laboratory corrosion tests need acceleration to the corrosion process; the only test that can be applied directly to affect the corrosion process is an electrochemical test. The major practical purpose is electrochemical tests, where fundamental electrode kinetics models related to corrosion processes are used to determine the corrosion rate. When the electrochemical process is taking place, an atomic mechanism can be deduced from the measurement of electrical

current and potential [102]. Measuring the current flowing between the anodic and cathodic sites has been effectively utilized to determine the processes during corrosion [103].

Electrochemical methods are used in corrosion research and chemical, oil and gas industries [103]. Using electrochemical techniques in the lab to evaluate the corrosion behaviour of alloys and metals, and also to avoid long-term field tests, determine the susceptibility of metal to bimetallic corrosion, corrosion rate, and pitting are some cases of corrosion types that can be examined in the lab via electrochemical techniques [104].

Electrochemical techniques of corrosion testing require a definition of particular properties of the electrical double layer formed when a metal contacts an electrolyte. These properties are the potential difference through the electric double layer (E) and the current density (i), which is the reaction rate per unit area [105].

The electrochemical test's main feature is that it can examine corrosion in the desirable solution instead of a less aggressive and possibly more relevant environment. Moreover, acquiring great information quickly, unlike the immersion test, requires a long time for testing [106].

Furthermore, electrochemical methods such as; galvanostatic, potentiostats and potentiodynamic are commonly used and well-known by electrochemists and corrosion engineers [107].

3.8.2 Polarization technique and Polarization Curves

Polarization is the shift in electrode potential from the equilibrium resulting from the current flow impacts. All corrosion reactions require current flow, changing the metal surfaces' potential. The resistance of the corrosion cell determines the polarization degree. This means the higher the cell resistance, the larger the shift in potential. $V = I.R$ [108].

In corrosion testing and research, one of the most common electrochemical techniques is determining the polarization curve, which is the relationship between the potential applied

and the current. The target to determine polarization curves is commonly under near steady-state conditions (for example, the measured current at every potential would be gained after a long while at a constant potential) [105].

3.8.3 Potentiodynamic Polarization technique

This is a common polarization technique in which the electrode potential is altered over a large range of potential at a designated rate by passing a current through the electrolyte [109].

The principle of the potentiodynamic polarization variant is called cyclic voltammetry, which requires varying the potential toward the positive route until a pre-set potential or current value is achieved. After that, the scan is driven backwards in the negative direction till the original potential value is achieved. In many instances, this scan can be done several times to determine the changes in the present current-potential curve created with scanning [109].

3.8.4 Passivity

Numerous metals can form an oxide layer on the surface as they corrode because of chemical reactions. As long as the oxide layer prevents corrosion, then it can be said this metal is passivated [110]. Also, metal is passive when it increases its potential to positive values, exhibits a low current rate at high potential, and the rate of dissolution reduces (also named as thin film passivity) [106]. Furthermore, alloys containing titanium, nickel and chromium tend to be more when they form protective surface films passive in strong oxidizing solutions. Also, semiconductors such as Carbon can increase the passivity region [110]. The passive barrier film can be amorphous or crystalline, with the advantage of an amorphous structure as it will be described in amorphous metal. Fig. 3.7 presents the typical corrosion behaviour of 304 SS, showing passivity region and pitting. The passive layer can cover various metal surfaces as pore-less continuous films, preventing metallic substrate dissolution. Normally, the thickness

of these oxide layers is around a few nm. In addition, the polarization curve of metals is caused by the formation of these oxide films.

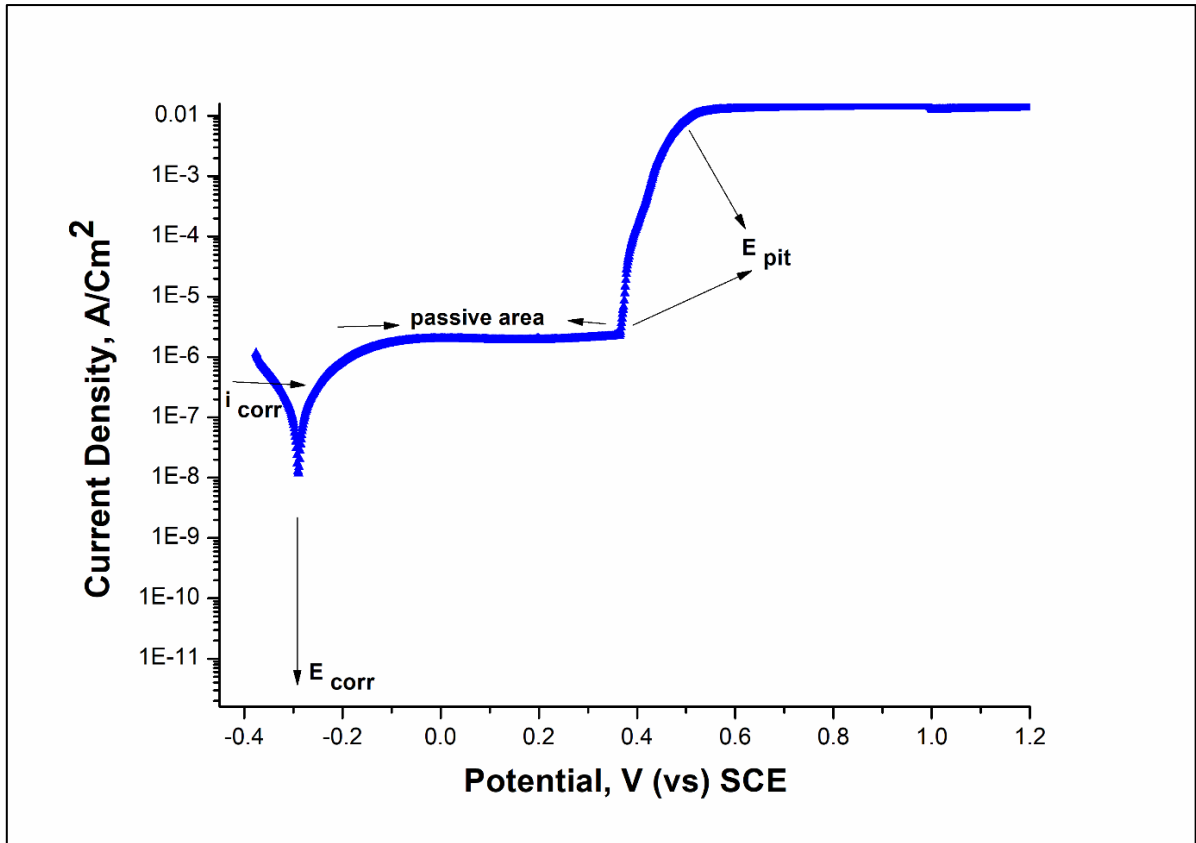


Figure 3-7: typical potentiodynamic polarisation curve of 304 SS [111].

Also, the polarisation curve can be in opposite orientation, as shown in fig. 3.8 below displays a polarisation curve of SS304 in 1 M NaCl. However, the readings and explanations are still under the same conditions.

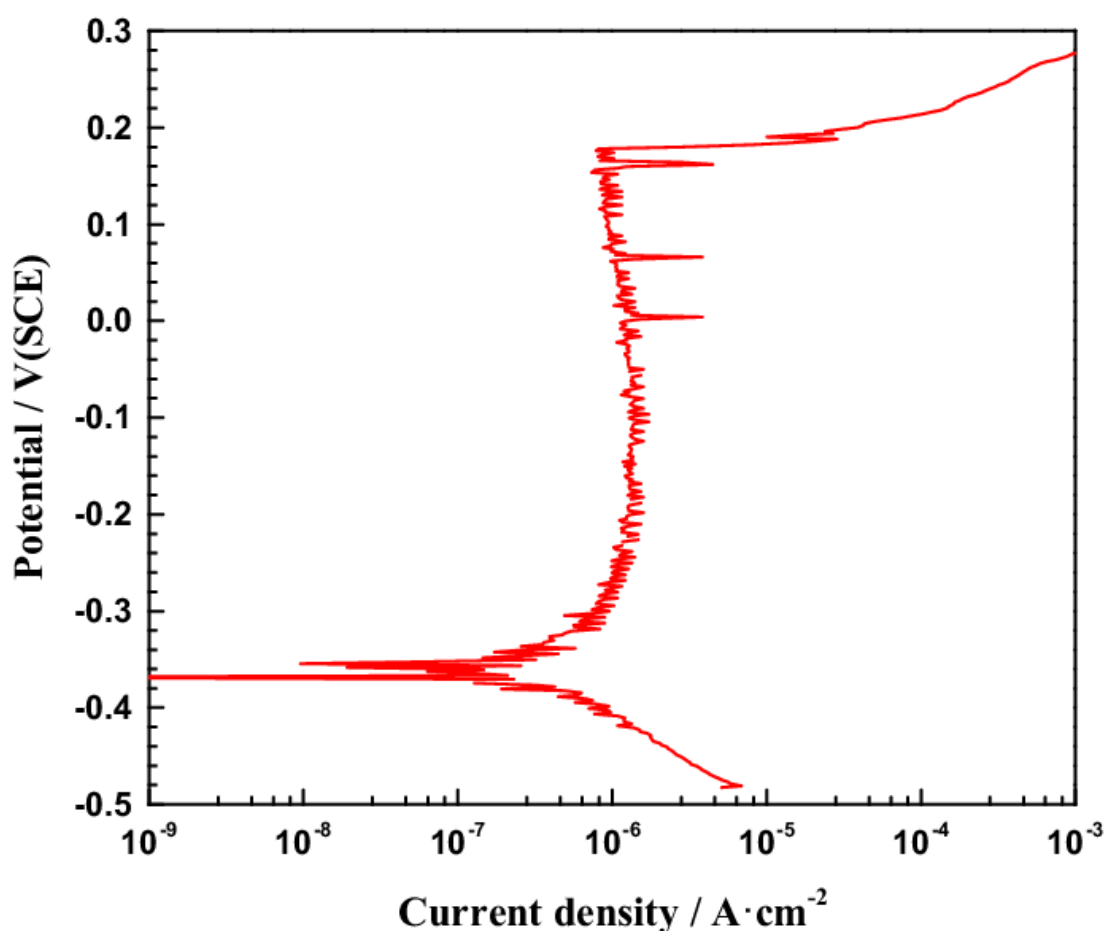


Figure 3-8: potentiodynamic polarisation curve of 304 SS in 1 M NaCl solution [112].

3.9 Potentiostat

A potentiostat is defined as a voltage source that can adjust its output potential to suit changes in the circuit resistance. As per Ohm's Law, potentiostats supply more or less current during electrochemistry tests; their primary role is to ensure constant potential across an electrochemically active cell. A potentiostat is used in many electrochemical cells to manage the working electrode's potential. The potentiostat is equipped with several internal circuits that enable its optimal performance. These circuits generate and measure the currents and potentials. The circuit of the potentiostat is connected to the electrochemical cell electrodes via external wires in a cell cable. The cell cable is connected to the working, counter, and reference electrodes and one end and to the cell cable connection of the potentiostat in a traditional three-

electrode cell. The internal circuitry of the potentiostat controls the applied signal. The working electrode potential is held concerning the reference electrode in potential-regulated methods. At the same time, current flows between the working and counter electrodes. The role of the potentiostat circuit is to prevent all but a small amount of current from flowing between the high-impedance reference electrode and the working electrode. While current potentiostats are more intricate than can be covered in this work, a basic overview of potentiostat circuitry will be covered to assist in knowing how they work [113-115].

A potentiostat is connected to a 3-electrode cell made up of the working, counter, and reference electrodes to make up the typical experimental setup. As shown in Fig. 3.9, as used in this investigation [116], the voltage between the reference and working electrodes is controlled by the potentiostats; it also detects the current between the counter and working electrodes.

Based on the employed approach, analysing the acquired data by a potentiostat exposes various intrinsic electrochemical features of the material. Hence, potentiostats are suitable for determining the material's redox potential and the reversibility of any reaction and can quantitatively describe the electrochemical reversibility & energy levels of polymers (semiconductors) using approaches like cyclic voltammetry [19].

This test, there are two different parts. The first is a brief OCP test to know the corrosion potential of the material to be analysed, and then a voltage sweep is made starting from a point close to the OCP to know how much current is passing through the circuit with the potential difference. In this way, it is possible to know, for example, the pitting potential of steel, or what is the same, with what voltage difference will pitting due to corrosion begins to occur in said steel [117].



Figure 3-9: an Autolab potentiostat used in this study.

Working electrode

In an electrochemical system, the working electrode is the main/primary electrode; it is the point of entry of the applied voltage into the system; most electron transfers and electrochemical reactions also occur in the working electrode. The voltage between the working and reference electrodes, as well as the current between the working and counter electrodes in a three-electrode system, can be determined using a potentiostat [118].

Reference electrode

The reference electrodes provide a constant for electrochemical measurements by providing a consistent, predictable, and well-defined electrochemical potential. The reference electrodes maintain a constant potential for measuring and controlling the working and counter electrodes by the potentiostat in a 3-electrode system. This is accomplished by utilizing materials with known electrochemical potentials, normally chemically isolated from the measured reactions. The reference electrode allows zero current flow in an ideal electrochemical system, allowing

accurate control and measurements of the working electrode potential. This is realized by ensuring that the reference electrode impedance is very low, ideally zero [117].

Counter electrode

Counter electrodes complete a three-electrode system's circuit also called auxiliary electrodes. The mechanical and electrochemical stability of platinum, as well as its high electrical conductivity, made it the most utilized material for counter electrodes. A high enough current and proper polarity are pushed between the counter and working electrodes to maintain the working electrode potential in consideration of the reference electrode [114]. Figure 3-9 displays the three electrodes set up.

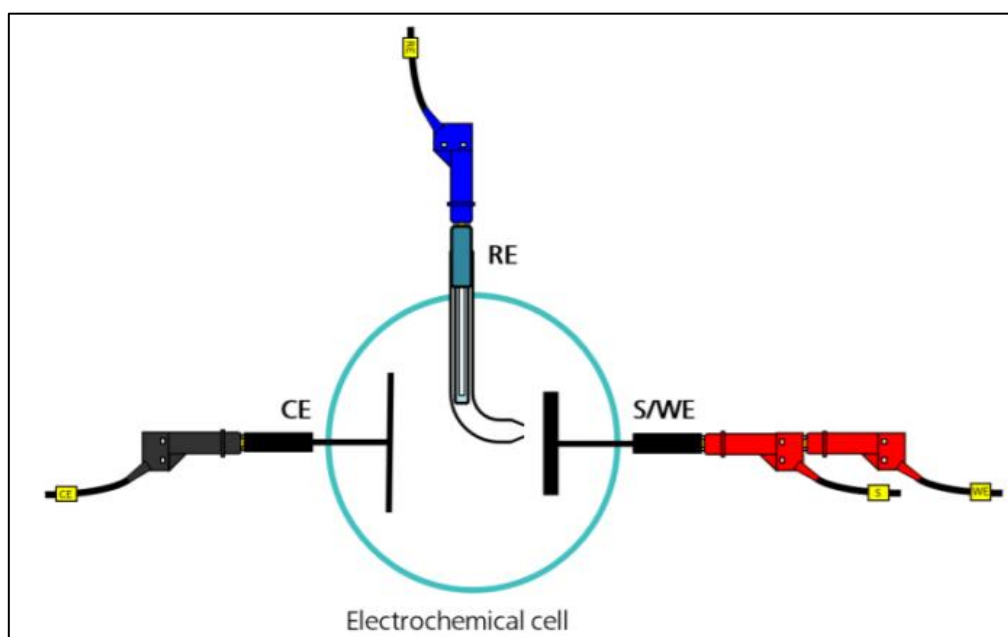


Figure 3-10: the three electrodes set up, RE reference electrode, WE working electrode and CE counter electrode [116].

3.9.1 NOVA software

Metrohm Autolab developed the NOVA software to facilitate the use of a USB connection to control all Autolab potentiostat/galvanostat instruments. NOVA software enables the users to

set up an experiment, take measurements, and analyse and plot data obtained from corrosion or electrochemical tests to produce ready-made publishable graphs. Tools, features and control panels in NOVA were developed to satisfy amateur and expert electrochemists' demands [119].

3.9.2 Electrochemical cell

The electrochemical cell is an electrode/solution arrangement used to study the corrosion process. To perform the electrochemical corrosion; there main requirements which are: an anode (where the metal oxidation happens), a cathode (where the metal reduction occurs), an electrolyte (the solution where the reaction between the two sites occurs), and a reference electrode (which provides a measurement of an applied potential) [106].

Electrochemical cells can be classified into driving or driven regarding their functions. Firstly, a driving electrochemical cell converts chemical energy into electrical power (also called a power producer). This power could be utilized externally to the cell in some cases. A driven electrochemical cell (mostly used in polarization techniques) is where a power supply like a battery is used to accelerate the chemical reaction (also named a power consumer). When there is no external influence in the corrosion system, it is called short-circuited [106].

3.10 Nanoindentation

Nano-indentation was developed to assess the mechanical properties of small material volumes to enable measurement of the hardness impression or contact area without having to image the indentation directly [74, 120]. The system allows the continuous recording of the applied force, P , and indenter displacement, h , throughout the loading and unloading indentation cycles. Various material properties, like hardness and elastic modulus, can be determined by analysing this data. The Oliver and Pharr approach, introduced in 1992, was the most often used analysis method. The approach was first devised for indentation data using a Berkovich indenter;

however, it was later realized that the method could be used for any axisymmetric indenter, even a sphere [121].

The nano-indenter, as seen in Figure 3.11, is made up of a diamond-based triangular pyramid-shaped indenter; a capacitance displacement gauge (CDG) is used to determine the position of this indenter. With a resolution of 0.2-0.3 nm, the CDG can detect changes in displacement. Computer programs control all activities, including data logging and indentation rate control. A diamond tip is frequently used to take measurements. During loading and unloading, the tip is driven into the surface, leaving a permanent impression; the penetration depth is then measured as a function of pressure. The sample hardness is calculated using the maximum displacement and the predicted indent area, while the elastic modulus is determined from the slope. It's vital to ensure that the utilized indentation depth is $< 10\%$ of the entire thickness of the film to avoid substrate impacts [121, 122].

Although the Nanoindentation technique is powerful, however, it has some limitations; for instance, it requires a professional sample preparation which consumes much time, the sample size should be smaller to fit the sample holder, the load applied on a sample is limited, the surface of the indented material should be fully flat and aligned to the indenter tip, and it is an expensive technique [123, 124].

The Nanoindentation system from Micro Materials Ltd, UK measured hardness and modulus for all samples. A Berkovich nano-indenter was used with a maximum load applied of 50 mN.

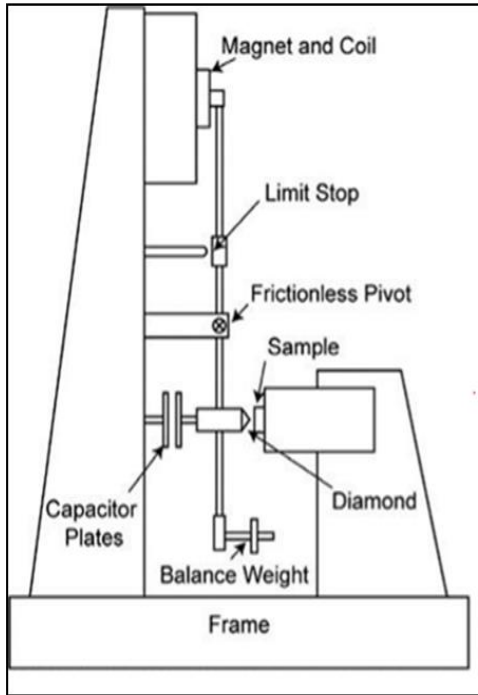


Figure 3-11: Figure 12: nano test, made by Micro Materials (UK), used in the present work [122].

3.11 Materials preparation

As seen in Fig 3.12, the Vacuum Arc Melting Furnace was used to prepare the bulk alloys from powdered Fe, Cr, Mn, Ni and C (purity ~ 99.5 %). The preparation of the compositions was done in a volume of 1cc using a total mass of about 8 g based on experience, as this is considered the right amount to facilitate the melting process. To minimize gaseous contamination to an acceptable limit: the samples were held in the furnace under a vacuum for about an hour. The melts were carried out in the presence of pure Ar gas at 500 mbar during the melting process. To homogenize the samples: the melting process was repeated five times before polishing with 120, 240, 600, & 1200 silicon carbide (SiC) papers and washing with 1 mic monocrystalline Gemini Diamond Slurry. The samples were then acetone cleaned and air-dried to prepare the surface for analysis.



Figure 3-12: Vacuum Arc Melting Furnace at the University of Huddersfield.

The thin film alloys were produced by ion beam sputter deposition displayed in Fig. 3.13 from the composite and elemental targets [FeCrMnNi and (Fe, Cr, Si Nb, and C)]. The deposition was carried out at normal room temperature on the steel, silicon, and silica substrates. The system was pumping until the deposition chamber's base vacuum reached 1.2×10^{-4} pa, and the deposition chamber pressure was 3.2×10^{-2} pa for about two h during the deposition process. The equiatomic ratio was achieved by geometrically changing the elemental objectives in the deposition chamber. The equiatomic composition was achieved after three attempts under a precise configuration of the elemental targets. The sample thickness (thin film) was calculated as 1.5 microns from the SEM.



Figure 3-13: Ion Sputter Deposition System University of Huddersfield

Specimen preparation for SEM and TEM

Semiconductors require no special sample preparation; the sample surface for examination is positioned on a special SEM stub using pads that can conduct electric current. A conduction part to the ground is required for samples mounted on an insulator to keep the samples from charging (which distorts the image).

The lateral resolution of the microscope used in this study was around 5 to 10 nm at 20 kV. The surface analysis started with low resolution such that most of the sample surface was covered, and then in the next stage, at 2000X to 5000x magnification, the images were

captured. This particular resolution helped in taking images revealing all the microstructural features and also for compositional analysis.

For a Transmission Electron Microscope (TEM, Hitachi-9500.) examination, a specimen was produced by a Focused Ion Beam (FIB). In addition, the atomic structure was studied by Selected Area Diffraction (SAD).

Electrochemical cell

The cell was constructed in the lab using a small rubber tube 8 mm in diameter to fit thin film samples. First, the sample's surface was cleaned with acetone, followed by deionised water. Then the sample was attached to the tube using super glue to avoid leaking and connected carefully with electrodes. The reference and counter electrodes are currently used from gold; the working electrode is the thin film sample. After connecting the electrode to the cell, the tube was filled in sodium chloride solution of 3.5% NaCl (simulating sea water). After that, the three electrodes were connected to the Potentiostat device. After ensuring all setup, the polarisation technique was chosen to view the potential and current readings of the corrosion environment. In the beginning, different scan rates were tested, and different results were obtained until recently seen the ASTM standard scan rate is 1 mV/s [125]. According to many experiments, the sample was kept in OCP (open circuit potential) for at least 30 minutes, then started to run to obtain the curve described in the result section.

4 Chapter4: “Microstructure and properties of FeCrMnNiCx compositionally complex bulk alloys.”

This chapter is a verbatim copy of the publication: Muftah, W., & Vishnyakov, V. (2021). Microstructure and properties of FeCrMnNiCx compositionally complex bulk alloys. Vacuum, 188, 110181.

4.1 Chapter overview

“Several studies have investigated the effect of varying the element concentration on the corrosion behaviour of HEAs and CCAs in different media. For example, a study showed that increasing Al content in $\text{Al}_x\text{CoCrFeNi}$ alloys decreased the corrosion resistance in a 0.6 M NaCl solution [126]. Also, corrosion resistance was reduced with an increasing Al concentration in $\text{Al}_x\text{CrFe}_{1.5}\text{MnNi}_{0.5}$ alloys.[127] However, pitting corrosion improves with increasing Al content in each of the 0.5 M H_2SO_4 and 1 M NaCl solutions [127]. Other elements like Mo in $\text{Co}_{1.5}\text{CrFeNi}_{1.5}\text{Ti}_{0.5}\text{Mo}_x$ enhance the pitting corrosion in 1 M NaCl solution [128]. In addition, a study of varying the composition concentration on AlCoFeNiTiZr alloys showed that the alloy had higher corrosion resistance due to the presence of a dual phase [64]. Modifying a particular element concentration was beneficial in some alloys and harmful in others.

Generally, the properties of HEAs or CCAs can be improved by adding elements such as O, B, N and C. The non-metallic additions allow complex oxides, borides, nitrides or carbides; these alloys are called high entropy compound materials [129].

Carbon is added to austenitic steels as the interstitial atoms could acquire exceptional mechanical properties due to the creation of multiple structural changes such as complex compositions, reduction of grain size and triggering nano-twinning [130, 131]. The effect of adding a variant concentration of carbon on high entropy alloys has been investigated and shown to be beneficial to HEA properties. The hardness, strength and wear resistance of CoCrFeNiC_x alloy have increased [77]. The oxidation resistance, scratch and hardness were improved of $\text{FeCoCrNiW}_{0.3+5}$ at.% of C alloy [132]. The hardness of FeCoCrNiMn with 2 at.% of C alloy was higher than carbon-free alloy [133]. Irradiation resistance was enhanced in $\text{Fe}_{38}\text{Mn}_{40}\text{Ni}_{11}\text{Al}_4\text{Cr}_7\text{C}_x$ alloy [134].

An equiatomic quaternary FeCrMnNi alloy synthesised by an arc melting furnace had a multi-phase alloy structure [135]. We previously showed that equimolar thin film FeCrMnNiC is amorphous, has high hardness at around 12 GPa, and has corrosion resistance better than 304 SS [111].

This chapter is aimed to find and characterise a novel single-phase bulk alloy. We report the synthesis and properties of new equiatomic and near equiatomic compositionally complex alloys - FeCrMnNiC_x (x= 20, 10, 5 and 2 at%).

There are various ways to represent a minor element in alloys. In this paper, we have adopted the following representation: FeCrMnNiC_x with 20 at% carbon is written as FeCrMnNiC; FeCrMnNiC_x with 10 at% carbon is written as FeCrMnNiC_{0.5}; FeCrMnNiC_x with 6 at% carbon is written as FeCrMnNiC_{0.3}; FeCrMnNiC_x with 2 at% carbon is written as FeCrMnNiC_{0.1}.

All synthesised alloys have been chosen because they have not been reported before by colleagues to date. Also, some elements were selected deliberately to improve the properties of the alloys. For instance, Cr, Ni and C were chosen to enhance the corrosion resistance. On the other hand, elements like C and Mn harden the alloys.

4.2 Materials and methods

The bulk alloys were synthesised in Vacuum Arc Melting Furnace from powders of iron (Fe), chromium (Cr), manganese (Mn), nickel (Ni) and carbon (C) with purity at ~ 99.5 (at. %), (99.5, 99.2, 99.9, 99.6 and 99.3) respectively. The compositions were prepared in a volume of around 1 cc with an ingot weight of approximately 8 g. The system with loaded powders was kept for a few hours under a vacuum to ensure the powders were outgassing. The melts were conducted in the presence of pure argon with a pressure during the melting at around 500 mbar. The melts were repeated five times to make the samples more homogeneous. After the melting, the ingots were kept in the furnace under a vacuum for around an hour to reduce gaseous contamination. The sample surfaces were then polished using 120, 240, 600 and 1200 silicon carbide (SiC) sandpaper. The final polishing was done by 1 mic monocrystalline Gemini Diamond Slurry. After that, the samples were cleaned with acetone.

The surface morphology was analysed by FEI Quanta FEG250 Scanning Electron Microscope (SEM) using both secondary electrons (SE) and backscattered electron detectors (BSED). Energy-Dispersive X-ray spectroscopy (EDX), Oxford Instruments, was used to analyse the chemical composition of the samples. It is reasonable in our case to believe that the uncertainty in quantification is at around 2 at%. X-ray diffraction (XRD) was measured by Bruker D2 Phaser instrument under Center 4.0 software.

Potentiodynamic polarization tests were conducted in three-electrode cell arrangements. A saturated calomel electrode (SCE) was used as a reference electrode, platinum as the counter electrode and samples as working electrodes (exposed area of 0.5 cm²) were used. The corrosion media was aqueous 3.5% NaCl solution. The measurements were done under ambient pressure and at room temperature. The open circuit potential (OCP) was measured for thirty minutes before each test. The potential and current were measured using Autolab

potentiostat controlled by Nova 1.10 software. The polarization curves were used to evaluate the corrosion parameters such as corrosion current density (i_{corr}) and corrosion potential (E_{corr}).

A Micro Materials Nano Test platform was used to assess the mechanical properties (hardness and modulus) of FeCrMnNiC_{0.1} bulk alloy. The instrument and Berkovich nano-indenter were calibrated using silica and tungsten samples.

4.3 Results and discussion

4.3.1 Microstructure

4.3.1.1 *FeCrMnNiC alloy*

Figure 4.1 (a) presents an average chemical composition of equiatomic FeCrMnNiC analysed by EDX. The material constitution (microstructure) revealed by the SEM with BSE detector at 20 KeV is in Fig1(b). Light element enriched secondary phase marked with a small black box with darker contrast in fig.1(b) can be seen. The secondary phase chemical composition taken by EDX is shown in Fig.1(c). The chemical composition in Fig.1(c) shows equal ratios of Cr and C (making the material almost chromium carbide) with smaller amounts of Mn and Fe.

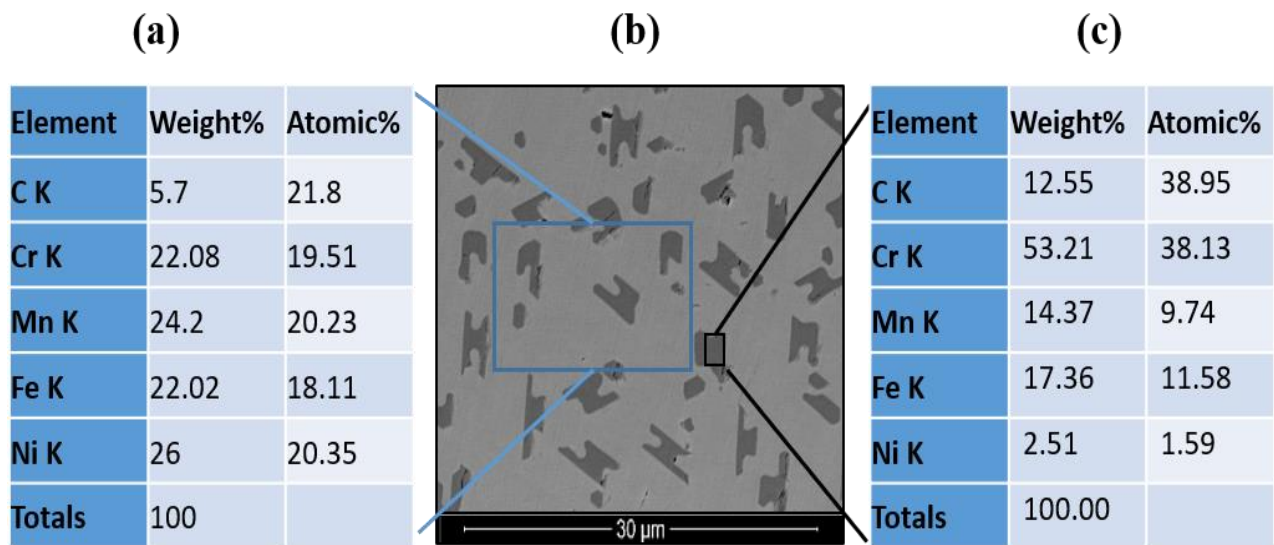


Figure 4-1: Analysis of microstructure and compositions of equiatomic alloy. (a) – average chemical composition of equiatomic FeCrMnNiC; (b) – BSEI surface microstructure image; (c) - chemical composition of the lighter element phase.

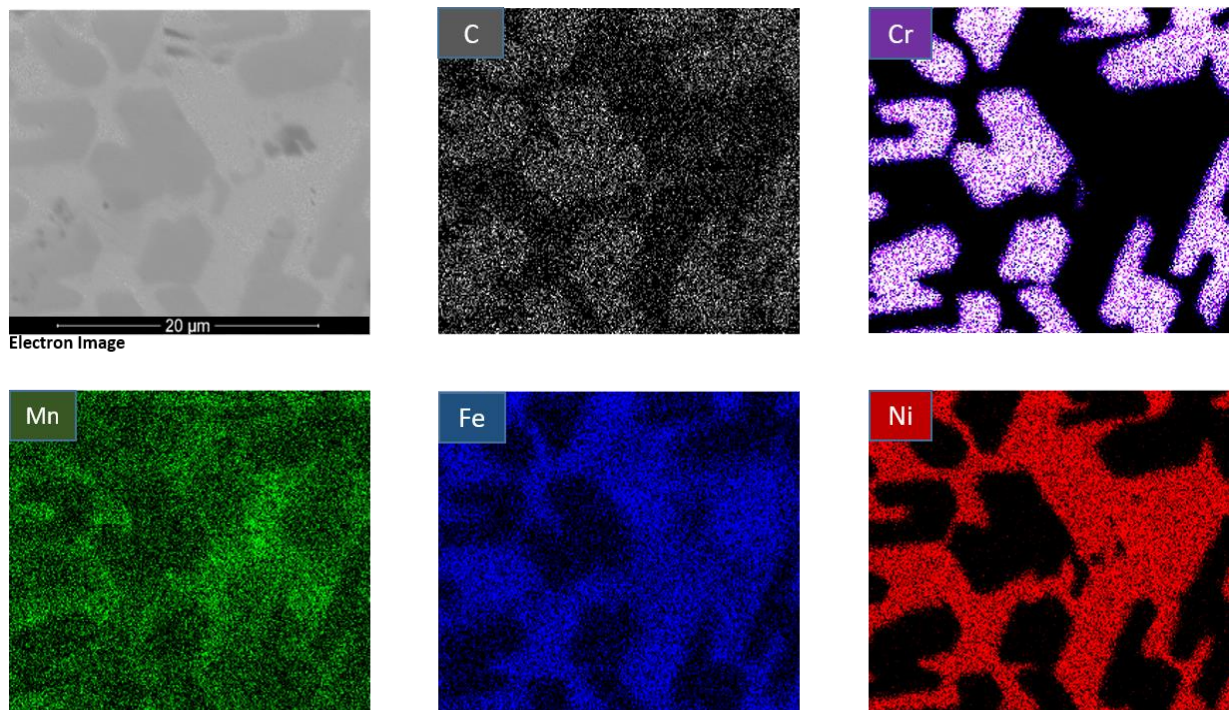


Figure 4-2: EDX mapping of FeCrMnNiC bulk alloy.

Figure 4.2 shows EDX elemental mapping of equiatomic FeCrMnNiC bulk alloy. The mapping demonstrates that the alloy is split into two phases – chromium/iron/manganese carbide and Ni/Mn.

It is well-known fact that Cr and Fe are strong carbide formers. Usually, the carbides in alloys form a compound in line with M_3C , but in FeCrMnNiC, carbon-rich precipitates are closer to M_2C composition.

4.3.1.2 *FeCrMnNiC_{0.5} alloy*

Fig 4.3 (a) demonstrates an average chemical composition of FeCrMnNiC_{0.5} analysed by EDX. The material structure (Fig 4.3 (b)) again shows the segregation of chromium and carbon, but the quantification ((Fig3(c)) reveals rather smaller iron segregation into the predominantly carbide grains.

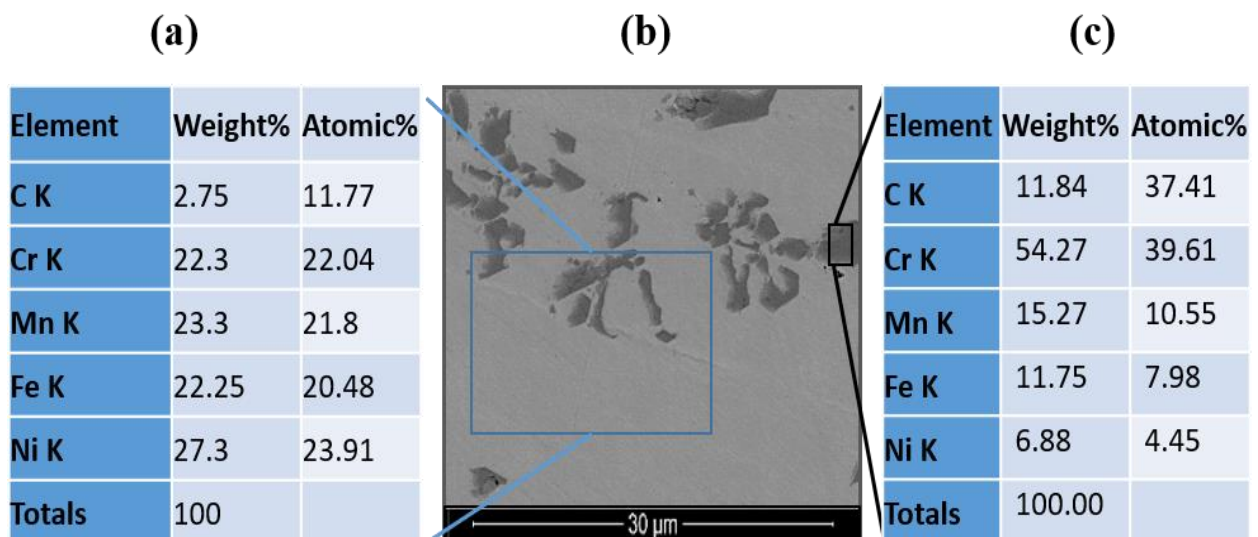


Figure 4-3: Analysis of microstructure and compositions of equiatomic alloy. (a) – average chemical composition of FeCrMnNiC_{0.5}; (b) – BSED surface microstructure image; (c) - chemical composition of the lighter element phase.

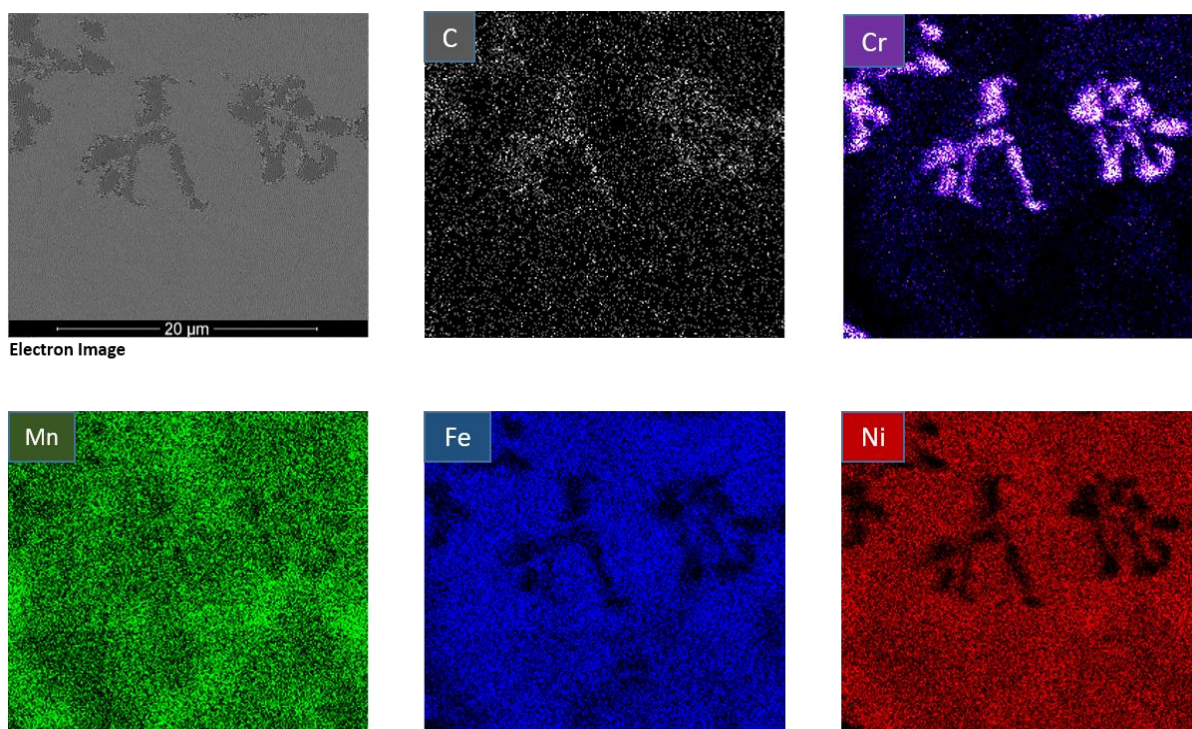


Figure 4-4: EDX mapping of FeCrMnNiC with 10 at. % of C bulk alloy.

Fig 4.4 clearly shows the existence of two compositionally distinctive phases. The maps of carbon and chromium show the co-segregation of those elements, which is attributed to the formation of predominantly chromium carbides. It is possible to note that Mn is more evenly distributed than the equimolar alloy in this case.

4.3.1.3 *FeCrMnNiC_{0.3} alloy*

In the case of FeCrMnNiC_{0.3} the EDX quantifications of distinctive areas (Figs 4.5(a) and 4.5(c)) show similar segregation to the higher carbon content alloys. Fig 4.5(a) shows the atomic percentage (at %) is near equiatomic in metals with 6 at% of carbon. The alloy has at least two phases, as demonstrated by the BSED detector surface microstructure image in Fig 4.5 (b).

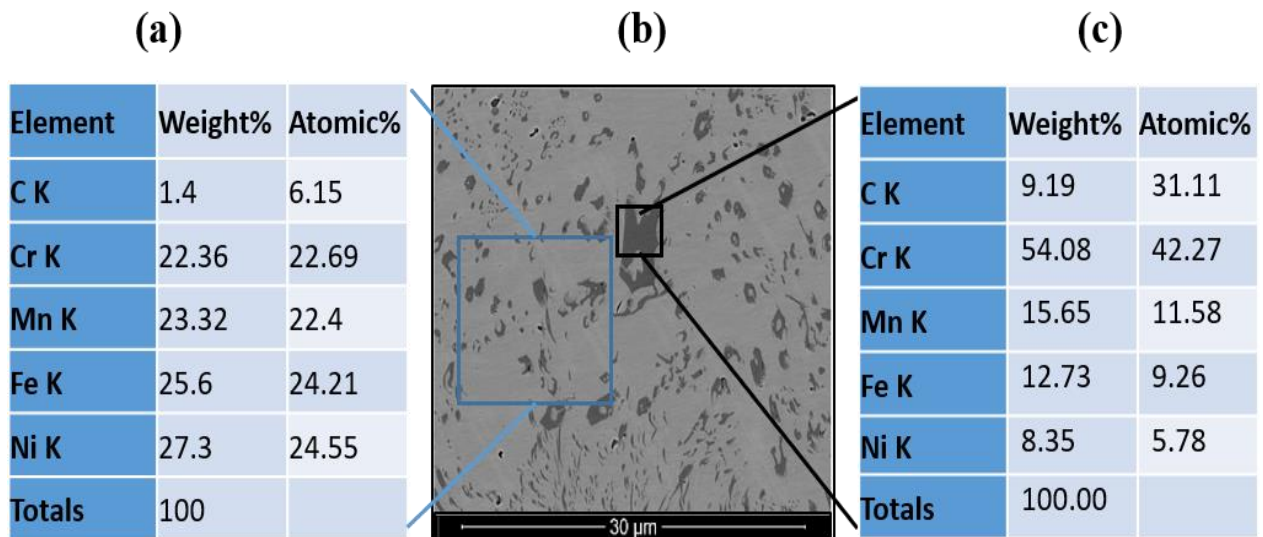


Figure 4-5: Microstructure analysis in FeCrMnNiCx alloy with 6 at. % of C: (a) - chemical composition of the alloy; (b) - BSED surface microstructure image at high magnification; (c) - chemical composition of the dark area as marked in (b).

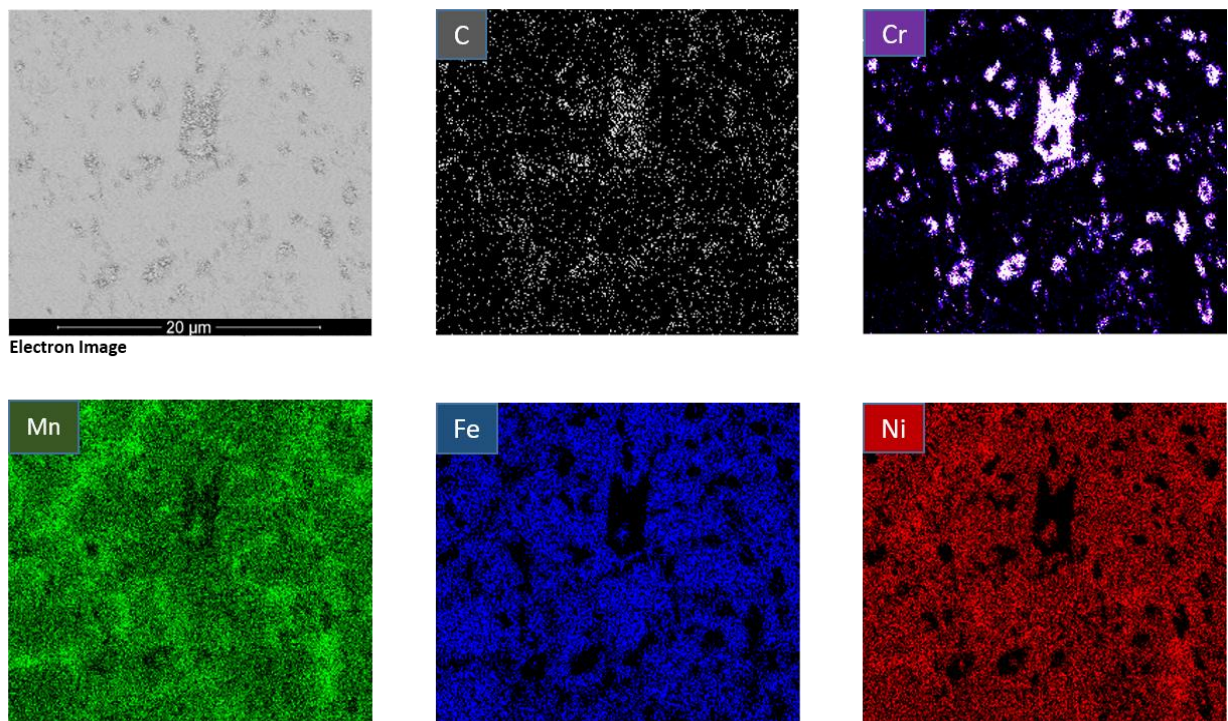


Figure 4-6: EDX element mapping of FeCrMnNiC_{0.3} bulk alloy.

At first glance (Fig 4.5 (b)), one can see only two phases. However, the element mapping in fig. 4.6 also reveals Mn preferential segregation in areas with less Cr/Fe carbides. Moreover, some carbide phases appear to be plate-like.

4.3.1.4 *FeCrMnNiC_{0.1}* alloy

After reducing carbon content to 2 at%, a single-phase alloy with uniform microstructure has been produced as provided in the BSED SEM surface image shown in figure 4.7 (a).

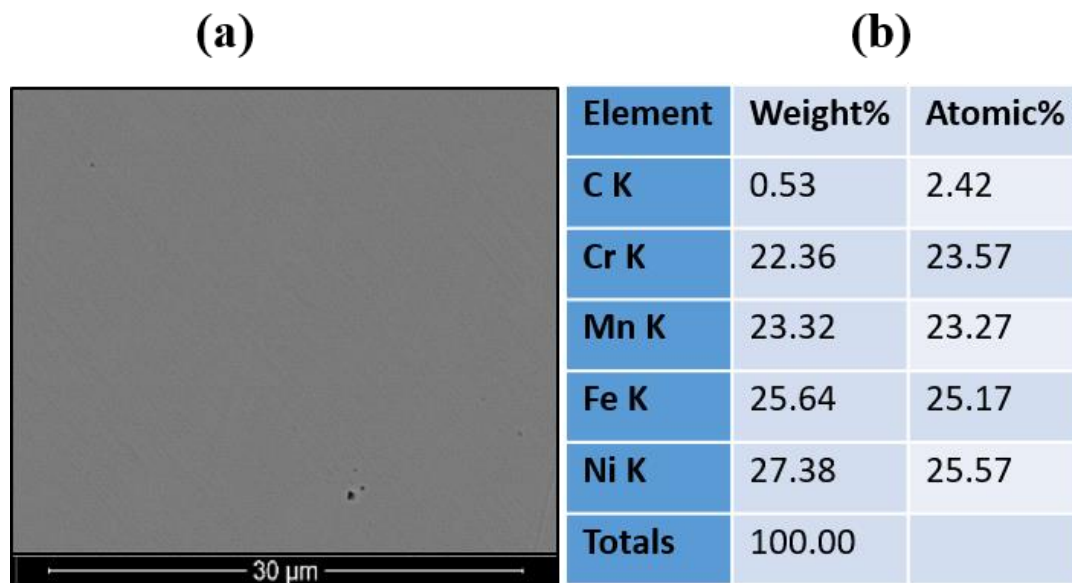


Figure 4-7: Analysis of the surface microstructure of FeCrMnNiCx alloy with 2 at. % of C: (a) - BSED surface image; (b) - chemical composition.

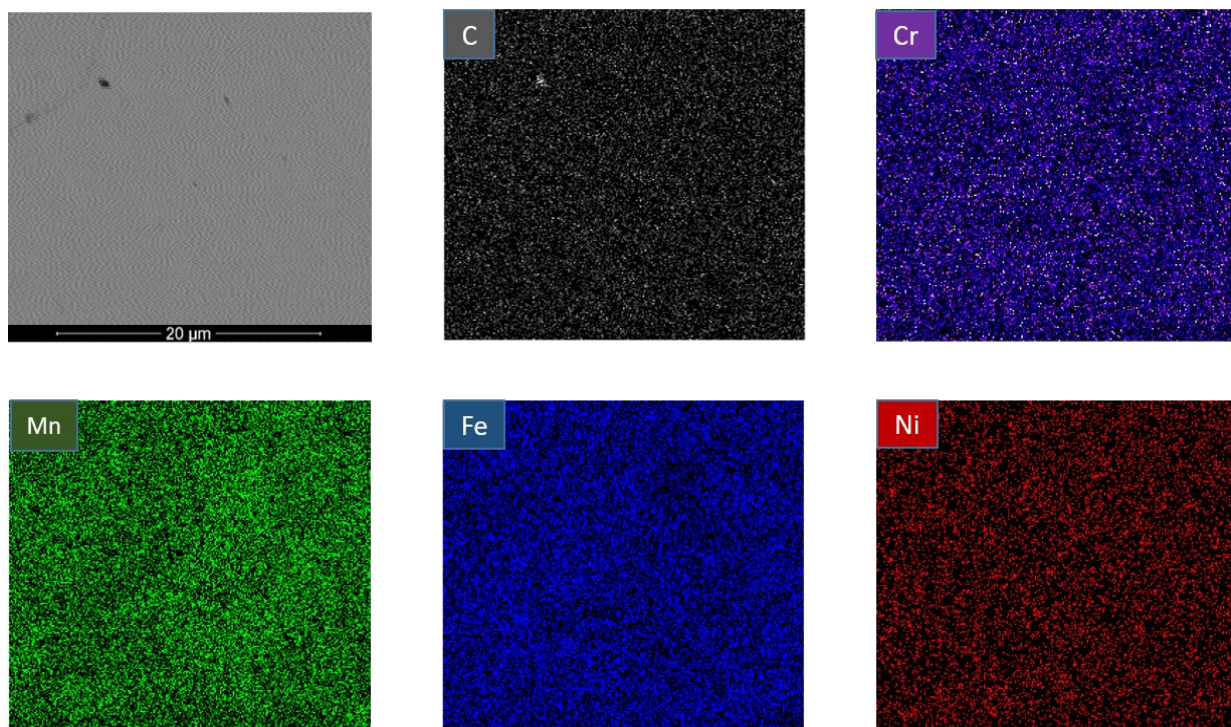


Figure 4-8: Alloy element EDX mapping in FeCrMnNiC0.1.

The EDX mapping (Fig. 4.8) confirms that C, Cr, Mn, Fe and Ni are distributed in the material homogeneously without any element separation or precipitation.

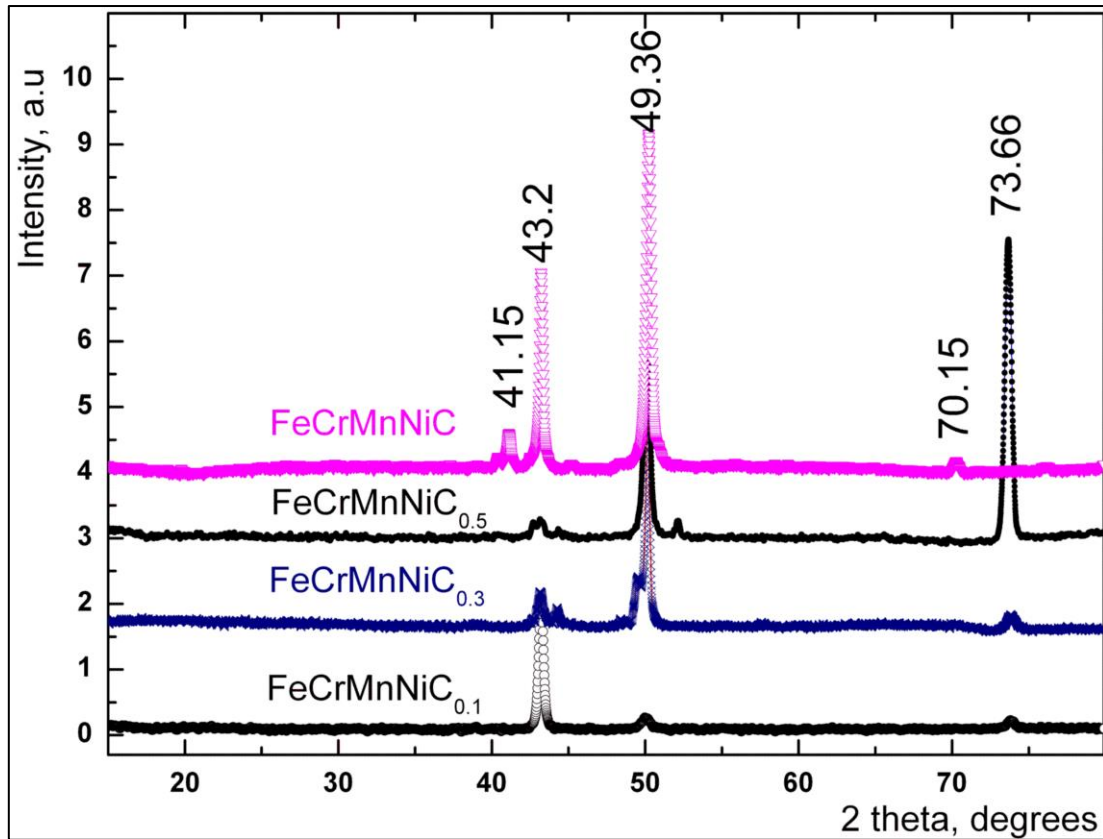


Figure 4-9: XRD patterns of crystalline FeCrMnNiC_x bulk alloys with different carbon content as shown in distinctive peaks.

XRD patterns of all FeCrMnNiC_x with varying carbon content are displayed in Fig. 4.9. It is possible to make a general statement that the patterns are quite complex and cannot be easily deconvoluted into simple BCC or FCC structures as for each phase, additional peaks are present, and those peaks cannot be indexed. It is probably easier to start with CrMnNiC_{0.1} as the material is not visible by BSD microscopy and EDX mapping phase separation. In this case, the main peak at 43.2° can be attributed to the (111) peak in the FCC phase in line with previously published work on NiCoFeCr with Al [136] and similar alloy with Co [137]. The peaks (200) and (220) at 49.93° and 73.66° also belong to the FCC phase.

Increased carbon content to 6 at% immediately complicates the spectra structure as additional phases appear (we also know this from the SEM analysis). For example, the peaks at 44.15° and 49.36° might belong to so named BCC and BCC/B2 phases [138].

The material at 10 at% develops a phase with a very strong reflection at 73.66° ((220) peak for FCC structure). This peak intensity rise looks like a texturing due to the alloy deformation (see, for instance, [137]), but the sample has not been deformed. Therefore, it is possible to assume that the peak is due to high stresses in the material due to more extensive carbide formation. A low-intensity peak at 52.3° probably indicates one of the secondary phases CrC [139].

The XRD spectra reflect but another material structure transformation when carbon content increases to 20 at%. The previous (220) peak completely disappears. The two small intensity peaks at (41.15° & 70.15°) can be secondary phases of chromium carbides [139]. Two high-intensity peaks probably belong to the previously observed FCC structure.

One can argue that carbides in steels are reasonably well understood, but a complex concentrated alloy with carbon during thorough analysis still reveals new complex phases [140]. Hence, the formation of single-phase high entropy alloys is believed to be limited by the possible limited lattice distortion effects, which can be calculated as a so-called δ parameter [141]. Carbon is an Interstitial element which can become soluble easily in alloys or compounds in less atomic percentages. Moreover, the atom radius of carbon is smaller than that of Fe, Ni, Mn and Fe, the carbon atom then can dissolve into the matrix and lead to lattice distortion. However, with the increase of carbon atoms, the excessive C atoms segregate to form carbides on grain boundaries during the solidification process [142, 143].

The effect of carbon content on CoCrFeNiMn was found to be single-phase with less C; however, carbide phases appeared when the C content increased. This also can be attributed to the effect of Cr on the solubility of C in a solid solution [77].

Many researchers have already shown that the formation of single-phase HEA by arc melting of bulk form only can be achieved when the difference between the atomic sizes is low (the δ value found to be < 8.6). In addition, if the entropy mixing is high, it enhances the formation of a single phase [141].

We, on our part and at this time, will cease the XRD analysis as our main focus was on a single-phase material and its properties.

4.4 Corrosion test

Potentiodynamic polarisation curve results for FeCrMnNiC_x (x= 2,5,10 and 20 at. %) bulk alloys are revealed in fig. 10. The numerical corrosion parameters (i_{corr} & E_{corr}) of FeCrMnNiC bulk alloys are provided in Table 4.1. The results confirm that as the amount of carbon increases, the resistance to corrosion increases for high-content FeCrMnNiC_x alloys.

Table 4-1: Corrosion parameters of FeCrMnNiC_x bulk alloys.

<i>Sample</i>	<i>i_{corr}, A/cm²</i>	<i>E_{corr}, v</i>
FeCrMnNiC _{0.1}	7.3*E ⁻⁷	-0.36
FeCrMnNiC _{0.3}	2.2*E ⁻⁷	-0.34
FeCrMnNiC _{0.5}	2.3*E ⁻⁷	-0.32
FeCrMnNiC	1.5*E ⁻⁷	-0.28

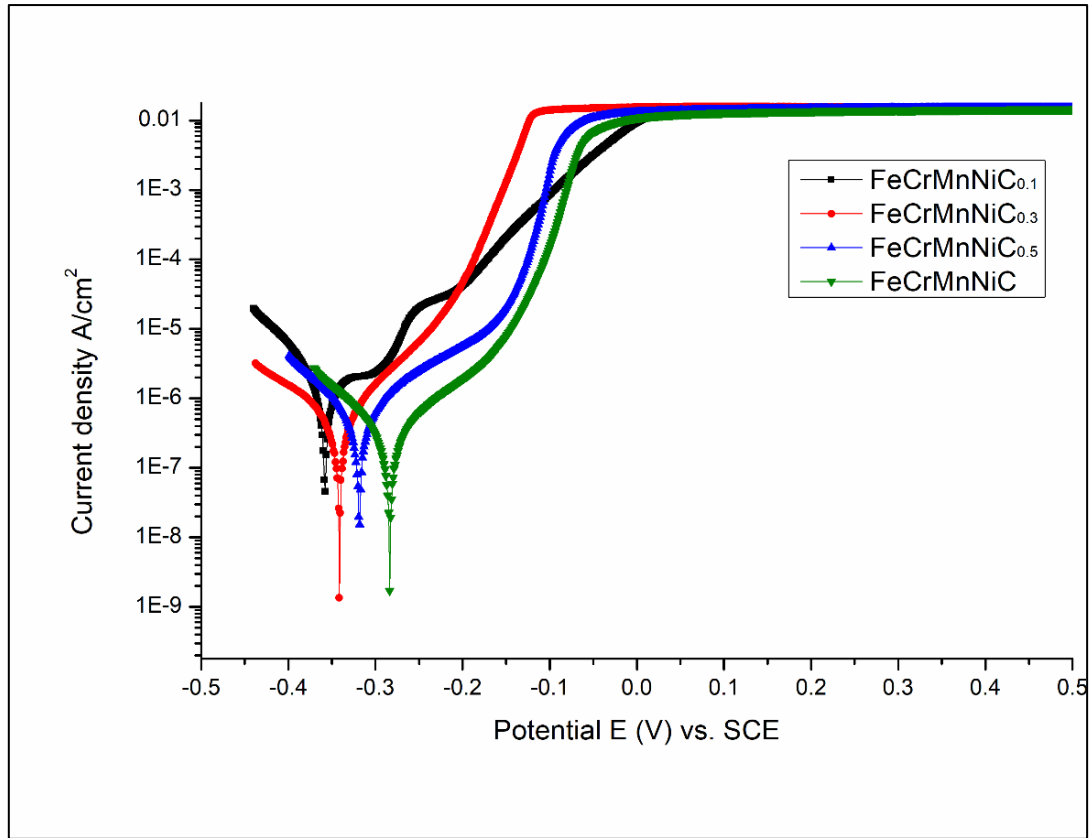


Figure 4-10: Potentiodynamic polarisation curves of FeCrMnNiC_x bulk alloys.

According to electrochemical practice, a material has good corrosion resistance when the corrosion potential E_{corr} increases to become more positive; this is accompanied by a reduction of corrosion current density i_{corr} [144, 145]. All our alloys exhibited similar corrosion behaviour with different corrosion values. It can be noticed from the polarisation curve on Fig. 4.10 that the corrosion potential moves towards higher cathodic as carbon concentration increases from 2 to 20 at. % in FeCrMnNiC_x alloys. The corrosion potential (E_{corr}) had improved from -0.36 to -0.28 V. The corrosion current density (i_{corr} , A/cm²) decreased from 7.3×10^{-7} to 1.5×10^{-7} . Apart from the influence of carbon and carbides, it is possible to assume that higher corrosion resistance is mediated by high entropy effect [10]. In other words, the cocktail effect of traditional elements (Cr and Ni), which have high corrosion resistance by themselves, improves the alloy's resistance to corrosion [63]. Adding a metalloid-like carbon to the alloy

further improves the resistance to corrosion [146]. The formation of CrC_x (chromium carbide) phase with a small content of manganese is also believed to have good corrosion resistance [147]. The above results are similar to other colleagues' earlier results, where the effect of Molybdenum (Mo) was found to be beneficial and enhances the corrosion resistance of CoCrFeNiMo_x , as CrMo phase played the main role in improving the corrosion resistance [148].

At this point, we have to admit that the same equiatomic composition FeCrMnNiC but as an amorphous coating, where mixing entropy probably was realised more fully, had exhibited much better corrosion performance ($E_{\text{corr}}=0.07\text{V}$, $i_{\text{corr}}=2.5\text{E-}10\text{ A/cm}^2$) [111].]

4.5 Mechanical properties

The hardness measurements were done for the single-phase FeCrMnNiC0.1 alloy. The indentation load was gradually varied from 20 to 50 mN. The results showed that the alloy has a hardness of $7.5 \pm 0.84\text{GPa}$. Reduced Young's modulus was at $250\pm 28.1\text{ GPa}$. The high hardness of the single-phase alloy FeCrMnNiC2 at. % can be attributed to the solid solution hardening effect [149]. It is also plausible to assume that the hardness is partially provided by the compositional homogeneity and partial alloying formation, which strengthens the bonding structure [82]. It demonstrates that adding carbon to high entropy alloy can be beneficial to increase the alloy's hardness. This is in agreement with the findings of other groups when adding carbon to CoCrFeNiC [77] and FeCoCrNiW0.3+5 at% of C [132] had led to better mechanical properties.

4.6 Summary

FeCrMnNiC_x (x= 2,5,10 and 20 at. %) alloys were produced by vacuum arc melting in search of a single-phase bulk alloy in the FeCrMnNiC_x system. Only FeCrMnNiC_x at x= 2 at. % was a single-phase alloy confirmed by BSE imaging, EDX mapping and EFTEM. At least two phases are observed at the higher carbon content in the FeCrMnNiC_x (x= 5, 10 and 20 at. %). The number of phases could be even higher, but it was considered outside the main interest. FeCrMnNiC_{2 at. %} is a new alloy and was found to be a single phase due to less carbon in the composition, as carbon is an interstitial element.

On the other hand, FeCrMnNiC_x (x= 5, 10 and 20 at. %) were multi-phase due to the increase of Carbon content; therefore, the carbon tends to form carbide phases with Chromium. All synthesised alloys were electrochemically tested in 3.5 wt. % NaCl solution to evaluate the corrosion resistance. The alloys get nobler and more corrosion-resistant as the amount of carbon content grows. However, comparing the corrosion properties of the current study with the amorphous thin film FeCrMnNiC demonstrates that not fully randomised lattice and possibly grain boundaries weaken the corrosion resistance. The FeCrMnNiC_{0.1} alloy showed a hardness of 7.5 ± 0.84 GPa, and reduced Young's modulus of 250 ± 28.1 GPa'' [150].

5 Chapter5: “Demanding applications - FeCrMnNiC amorphous equiatomic alloy thin film.”

This chapter is a verbatim copy of the publication: Muftah, W., Patmore, N., & Vishnyakov, V. (2020). Demanding applications in a harsh environment–FeCrMnNiC amorphous equiatomic alloy thin film. *Materials Science and Technology*, 36(12), 1301-1307.

5.1 Chapter overview

“In this chapter, we report the synthesis and corrosion resistance of a new equiatomic amorphous high entropy thin film alloy based on five elements: Fe, Cr, Mn, Ni and C. Elements were chosen based on published and desirable properties. Iron, for instance, is the principal element in most HEAs due to its wide availability and high miscibility with many other elements. Furthermore, Cr and Ni have good corrosion resistance, and Mn is used in many cases to harden an alloy. In addition, (Fe, Cr & Ni) combination is used in more than 70% of HEAs. Finally, carbon was chosen to increase the alloy hardness and enhance corrosion resistance. The whole FeCrMnNiC alloy is new and has not yet been investigated and reported by colleagues.

5.2 Materials and methods

The thin film alloy was synthesised by an ion beam sputter deposition system [151] from a composite target of FeCrMnNi and an elemental target of C. The deposition was done on a Silica substrate at room temperature without heating. Silicon substrates were used as they are standard substrates for coatings and thin film depositions. Silicon substrates are brittle and easy to break, which can be sized and shaped as required. Also, they withstand high temperatures, allowing different temperature rates [152-154]. The base system pressure was 2.2×10^{-4} Pa, and the Ar partial pressure in the deposition chamber during the deposition was 3.4×10^{-2} Pa (pressure was not gauge sensitivity corrected). The equiatomic composition was reached by geometrically adjusting the elemental targets under the sputtering beam. The thin film sample's thickness was around 1.5 microns as measured after Focused Ion Beam (FIB) sectioning.

An FEI Quanta FEG250 Scanning Electron Microscope (SEM) was used for the material surface observations. In addition, The chemical composition of the samples was investigated by Energy-Dispersive X-ray spectroscopy (EDX), Oxford Instruments. X-Ray Diffraction (XRD) was performed on a Bruker D2 Phaser instrument. Measurement Center 4.0 software was used to examine the crystal structure. Selected Area Diffraction (SAD) and imaging in Transmission Electron Microscope (TEM) were used to analyse atomic structure in detail.

Potentiodynamic polarization tests were performed in a three-electrode cell system, with the specimens as working electrodes (exposed area of 0.5 cm^2), saturated calomel electrode (SCE) as reference electrode and platinum as the counter electrode. The electrolyte used was an aqueous 3.5% NaCl solution. The measurements were taken at room temperature under atmospheric pressure. Before each experiment, the open circuit potential (OCP) was measured for 30 min to reach a stable potential. The current and potential were measured using an Autolab potentiostat controlled by Nova 1.10 software. According to ASTM standards, the potentiodynamic tests were conducted at a scan rate of 1 mV/s. Electrochemical parameters

such as corrosion current density (i_{corr}), corrosion potential (E_{corr}), and passivation regions were acquired by evaluating polarization curves.

A Nanoindentation system from Micro Materials Ltd, UK used to evaluate the nano hardness of FeCrMnNiC amorphous HEATF. The maximum load applied was 50 mN.

5.3 Results and Discussion

5.3.1 Microstructure

Figure 5.1 (A) shows the BSED (backscatter) SEM image of FeCrMnNiC high entropy thin film alloy. The absence of any topographical and electron channelling contrasts is the first indication of the film's amorphous nature. Figure 1B EDX analysis represents the chemical composition of FeCrMnNiC thin film alloy confirming the equiatomic ratio.

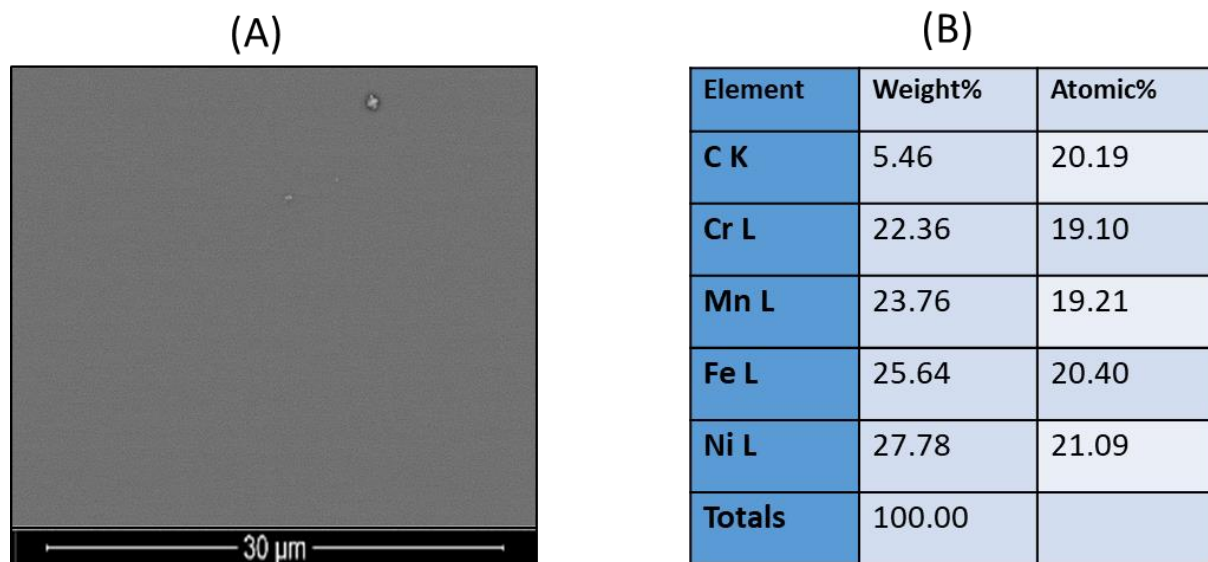


Figure 5-1: Surface microstructure of FeCrMnNiC amorphous high entropy thin film alloy (A) and elemental composition (B).

Elemental EDX mapping in Figure 5.2 shows uniform distribution of FeCrMnNiC alloy elements. The data confirm that the Cr, Mn, Fe and Ni elements present in the matrix are distributed homogeneously.

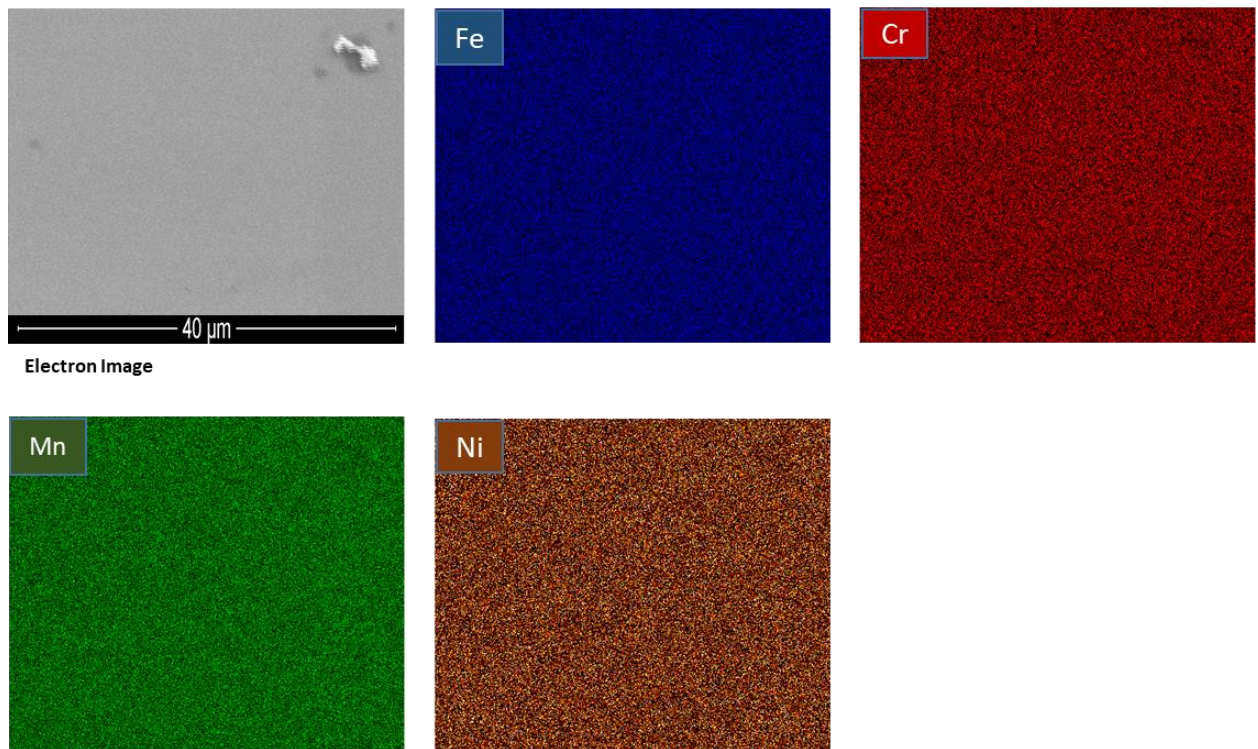


Figure 5-2: Elemental EDX mapping of FeCrMnNiC thin film.

XRD spectrum (Fig 5.3) confirms that FeCrMnNiC high entropy thin film alloy has an amorphous structure. The spectrum has only a peak at around 42° and does not demonstrate any sharp diffraction peaks. The other peak in 20° regions is referred to as the glass substrate.

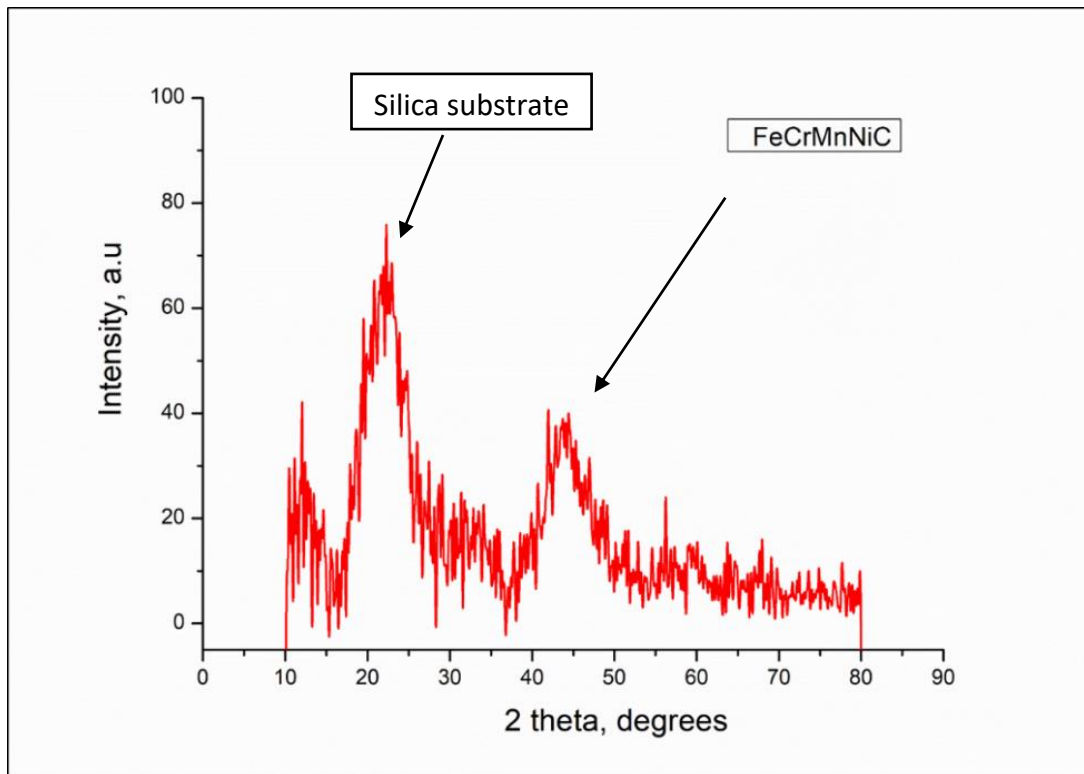


Figure 5-3: XRD pattern of amorphous FeCrMnNiC high entropy thin film alloy.

Transmission Electron Microscopy (Fig 5.4) shows uniform image contrast without any diffraction or mass thickness contrast. The SAED only shows the broad diffraction ring typical of amorphous structures without any trace of nanocrystalline. All the above demonstrates that the films are dense, uniform and amorphous.

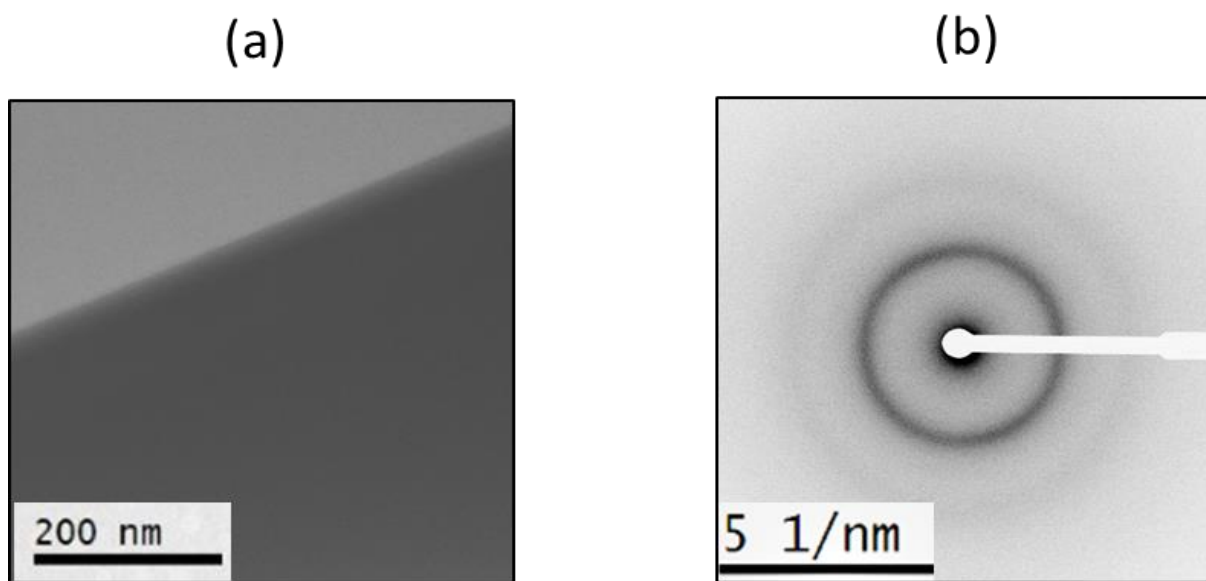


Figure 5-4: BFTEM image (a) and its SAED (b) of FeCrMnNiC thin film deposited on silica substrate at room temperature. The film in the image is in the right-bottom corner.

In many cases, thin films deposited at low temperatures (close to room temperature) do not have sufficient diffusion for possible phase separation. They are “frozen” in the not thermodynamically equilibrium state. This might be an advantage compared to bulk (for instance, arc melting) synthesis. Indeed, this was demonstrated before; there was no phase separation and segregation in synthesised CrCoCuNiFe thin films compared to bulk CrCoCuNiFe, which was found to be a two-phase alloy [55].

Even if films are deposited at the elevated substrate temperature, the temperature might not be high enough to produce crystallization rearrangement of amorphous, as immediately deposited, structure. For instance, this was the case in earlier work [155], when AlCoCrCuFeNi thin film deposited by magnetron sputtering at temperatures 110–510 °C was still not crystalline.

However, in our case, large atomic size differences and rapid cooling during deposition can assist in preserving the amorphous state, as predicted earlier [48, 156].

5.3.2 Electrochemical tests

The potentiodynamic polarization curve results for FeCrMnNiC equiatomic high entropy amorphous thin film compared with 304 SS are shown in Fig 5.5. In addition, the numerical corrosion parameters, such as corrosion current density and corrosion potential of the amorphous HEA against 304 SS, are provided in Table 5.1.

Fig. 5.6 and table 5.2 show the corrosion parameters of the amorphous FeCrMnNiC HEATF alloy and 304 SS in 0.6 H₂SO₄ solution. Fig. 5.7 and table 5.3 displays the corrosion parameters in crude oil.

The results show that FeCrMnNiC amorphous high entropy alloy and 304 SS both have high corrosion resistance in NaCl, H₂SO₄ solutions and crude oil, but better results are seen for the amorphous HEA thin film alloy.

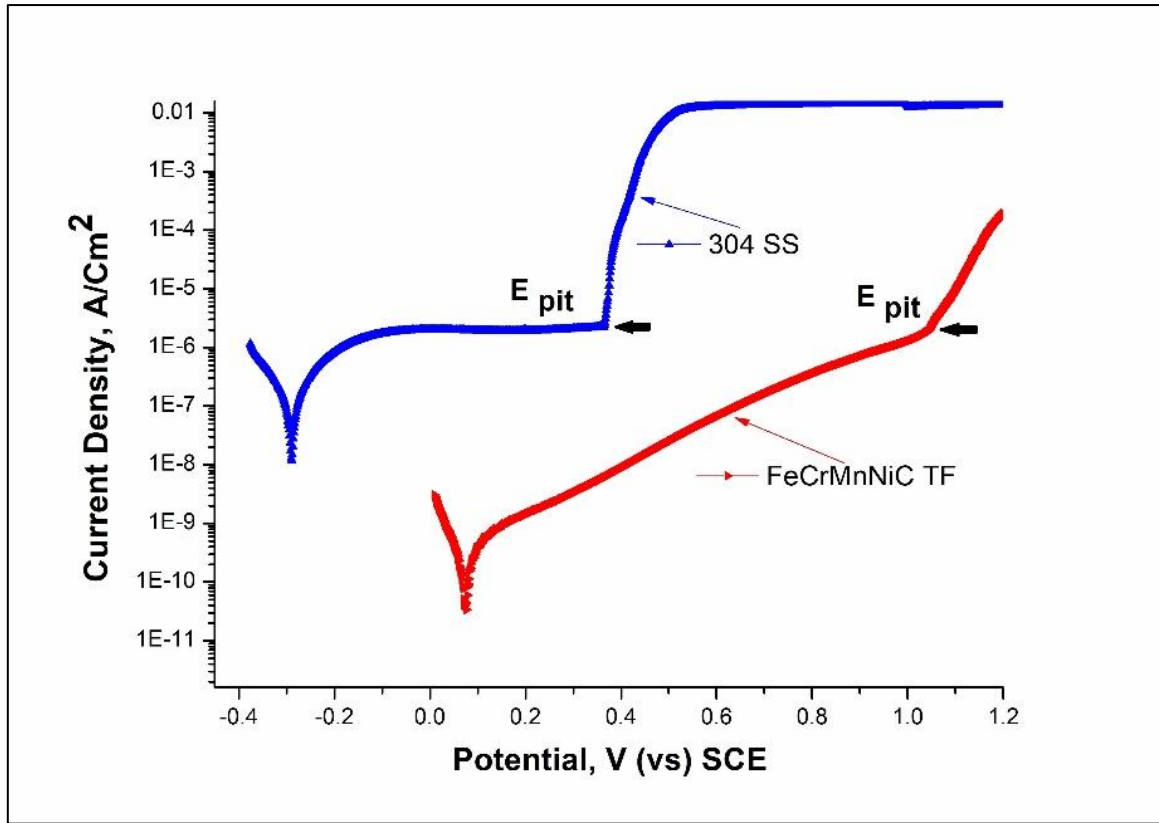


Figure 5-5: Potentiodynamic polarisation curve of FeCrMnNiC amorphous high entropy thin film & 304 SS in aqueous 3.5% NaCl solutions at room temperature

Table 5-1: Corrosion parameters of FeCrMnNiC amorphous HETF and different types of HEAs tested in 3.5% NaCl solution.

<i>Sample</i>	<i>Type of HEA</i>	$i_{corr}, A/cm^2$	E_{corr}, v	E_{pit}, v	<i>reference</i>
FeCrMnNiC	Coating	$2.5 \cdot 10^{-10}$	0.07	1.04	Current study
304 SS	Bulk	$1.1 \cdot 10^{-7}$	-0.29	0.36	Current study
CrMnFeCoNi	Coating	$1.1 \cdot 10^{-7}$	-0.09	0.22	[157]
CoCrFeNiW	-	$1.4 \cdot 10^{-5}$	-0.99	-0.37	[158]
CoCrFeNiW _{0.5} Mo _{0.5}	-	$1.4 \cdot 10^{-6}$	-1.02	-0.26	[158]
(CoCrFeNi) ₉₅ Nb ₅	-	$7.2 \cdot 10^{-6}$	-0.37	0.26	[159]

AlTiCrNiTa	-	3.2×10^{-8}	-0.26	N/A	[64]
FeCoNiCr	Bulk	3.1×10^{-8}	-0.26	0.31	[60]
FeCoNiCrCu	-	1.3×10^{-6}	-0.33	0.08	[60]
AlCoCrCuFe	-	9.7×10^{-7}	-0.25	-0.13	[160]
AlTiVCrSi	-	1.7×10^{-7}	-0.49	-0.01	[160]
CoCrFeNi ₂	-	1.3×10^{-7}	-0.29	N/A	[161]
CoCrFeNi ₂ Mo _{0.25}	-	1.3×10^{-7}	-0.26	N/A	[161]

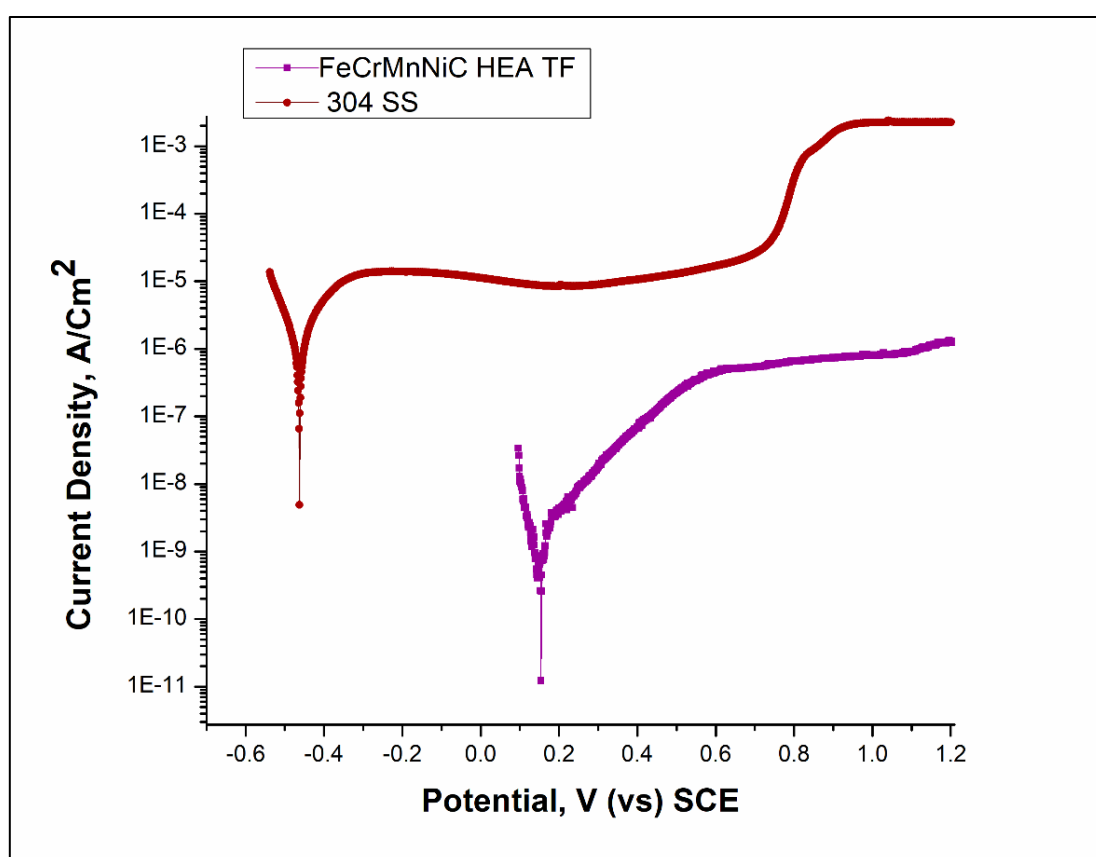


Figure 5-6: Potentiodynamic polarisation curve of FeCrMnNiC amorphous high entropy thin film & 304 SS 0.6 M H₂SO₄ solution.

Table 5-2: the corrosion parameters of FeCrSiNb HE TF alloy and 304 SS in 0.6 M H₂SO₄ solution.

Sample ID	i_{corr} , A/Cm ²	E_{corr} , V
FeCrMnNiC	$1.11 \cdot 10^{-9}$	0.15
304 SS	$4.86 \cdot 10^{-6}$	-0.46

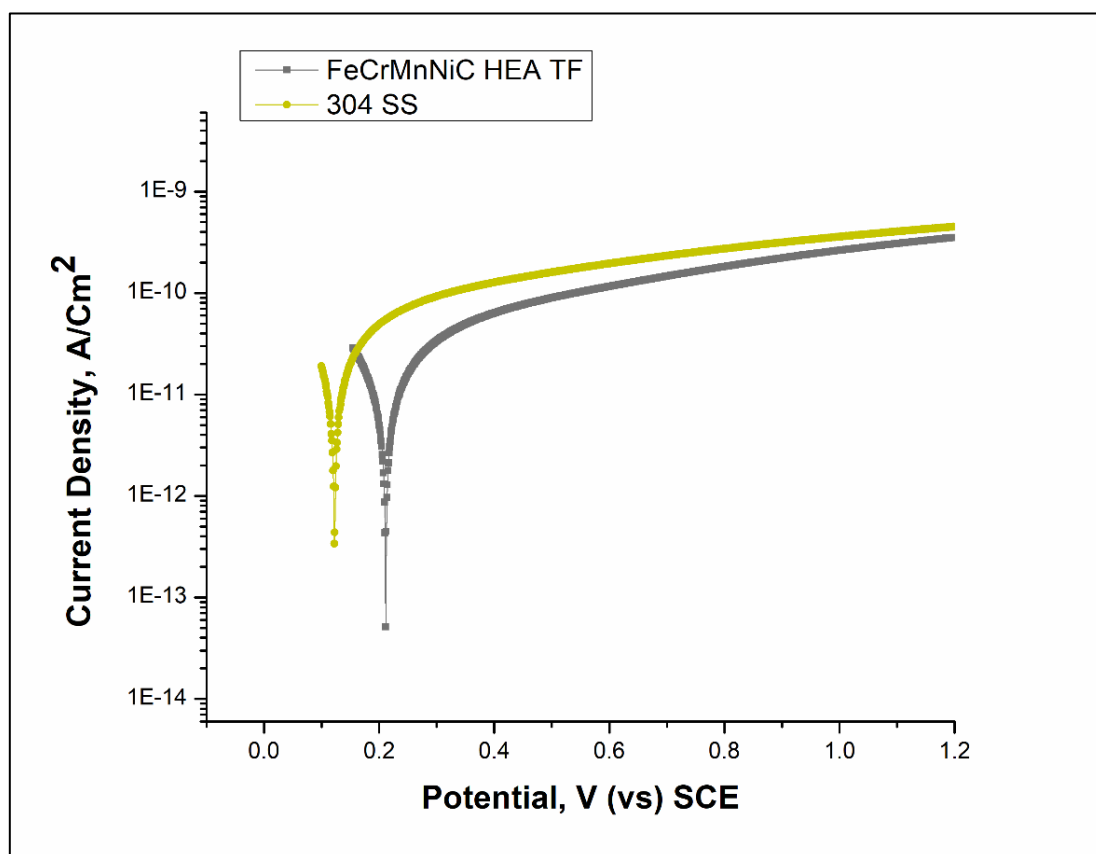


Figure 5-7: polarization curves of FeCrSiNb HEA thin film & 304 SS in crude oil.

Table 5-3: the corrosion parameters of FeCrSiNb HEA thin film and 304 SS in crude oil.

Sample ID	i_{corr} , A/Cm ²	E_{corr} , V _{SCE}
FeCrMnNiC	6.56×10^{-12}	0.22
304 SS	9.91×10^{-12}	0.12

According to the electrochemical theory for analysing corrosion behaviour, the material is resistant to corrosion if it exhibits a small corrosion current density (I_{corr}) with a high, cathodic corrosion potential (E_{corr}) [106]. As can be seen from the polarisation curve, the corrosion potential (E_{corr}) of HEATF (0.07 V) is significantly more cathodic than that of 304 SS (-0.29 V) in NaCl solution. As a result, the corrosion current density (i_{corr}) of HEATF (2.5×10^{-10}) is lower than 304 SS (1.1×10^{-7}). In addition, a larger passivation potential area exists in HEATF compared to 304 SS (0.93V vs 0.65V). Therefore, even at the pitting potential, the corrosion current for HETF is lower than for 304 SS.

Fig. 5.6 and table 5.2 show the corrosion parameters of the amorphous FeCrMnNiC HEATF alloy and 304 SS in 0.6 H₂SO₄ solution. The FeCrMnNiC has a corrosion potential (E_{corr}) of 0.15 V, much higher than 304 SS -0.46 V. On the other hand, the corrosion current density (i_{corr}) of FeCrMnNiC (1.11×10^{-9}) is smaller than 304 SS (4.86×10^{-6}).

In the case of the corrosion test in crude oil, the HEATF alloy also showed higher corrosion 0.22 V than 304 SS 0.12 V, with lower corrosion current density 6.56×10^{-12} than 304 SS 9.91×10^{-12} , as presented in Fig. 5.7 and table 5.3

In summary, the FeCrMnNiC amorphous HEATF alloy has excellent corrosion resistance - much better than 304 SS in NaCl, H₂SO₄ solutions, and oil. This can be attributed to the four

main effects of high entropy alloys; entropy effect, cocktail effect, sluggish diffusion effect, and lattice distortion effect [59, 162]. Also, the equiatomic composition and the uniform structure without element segregation led to the homogeneous microstructure of the alloy [69]. In addition, the low corrosion rate is due to the absence of grain boundaries in the amorphous film, as corrosion usually occurs preferably at grain boundaries [163, 164]. It is also possible to suggest that there is an effect of elements with excellent corrosion resistance, such as chromium and nickel, in the composition, which can form a protective passivation layer preventing further corrosion on the alloy surface. The latter is in line with corrosion resistance in HEAs suggested earlier [63].

Although stainless steel is a widely used material with good corrosion resistance, however, stainless steel is mostly relying on the amount of chromium element in the composition. Cr reacts with oxygen in the air to create a passive layer to prevent the surface from corrosion. However, over time and in several surrounding conditions, the passive protective layer begins to break up, resulting in a formation of holes called pitting, causing the application's failure. For instance, the presence of H_2 , H_2S and seawater on the material surface can lead to failure of the passive layer after some time and therefore develop the occurrence of pitting. This requires regular maintenance by removing the rust and cleaning the material surface with specific mechanical or chemical substances. However, this cannot be applicable in many applications in the oil field [31, 32]. Another advantage of amorphous equiatomic FeCrMnNiC and FeCrSiNb HEA thin films over stainless steel is that higher corrosion potential (E_{corr}) values in HEA thin films, which can be referred to that high entropy alloys undergo self-passivation at the beginning of the test, and this what makes high entropy alloys unique and better than stainless steel which has less corrosion potential (E_{corr}) values [51, 126]. In addition, adding metalloids such as carbon to the alloy is likely to enhance corrosion resistance [146]. As sintered, the FeCrMnNiC amorphous HEATF exhibited better corrosion resistance

than many high entropy alloys coatings such as CrMnFeCoNi [157]; CoCrFeNiW, CoCrFeNiW_{0.5}Mo_{0.5} [158]; (CoCrFeNi)₉₅Nb₅ [159] and AlTiCrNiTa [64]. Also, high entropy bulk alloys such as FeCoNiCr and FeCoNiCrCu [60]; AlCoCrCuFe and AlTiVCrSi [160]; CoCrFeNi₂ and CoCrFeNi₂Mo_{0.25} [161]. Corrosion parameters of all mentioned alloys are provided in table 1.

5.4 Nanomechanical properties

The film hardness was measured by nanoindentation. Moreover, the film was deposited on a silicon substrate with a measured thickness of around 1.6 microns. The maximum plastic penetration depth was limited to below 500 nm to avoid significant influence from the substrate [165]. This was proved from previous experiments and studies such as CoCrFeMnNi, and NbTaMoW high-entropy alloy thin films, which stated that with a film thickness ranging from 1-2 microns, the average ~300 nm of plastic penetration depth is suitable to perform nanoindentation test [166, 167]. Incremental loading was used to account for the influence of penetration depth on the measured mechanical properties. Figure 5.8 shows a series of nanoindentation curves. The average film hardness is 12.3 ± 0.5 GPa. The reduced Young's modulus is estimated by the modulus approximation to zero loads (in line with ISO14577 part 4 standard) as shown in Fig.5.9. The reduced Young's modulus is estimated to be 222 ± 7 GPa.

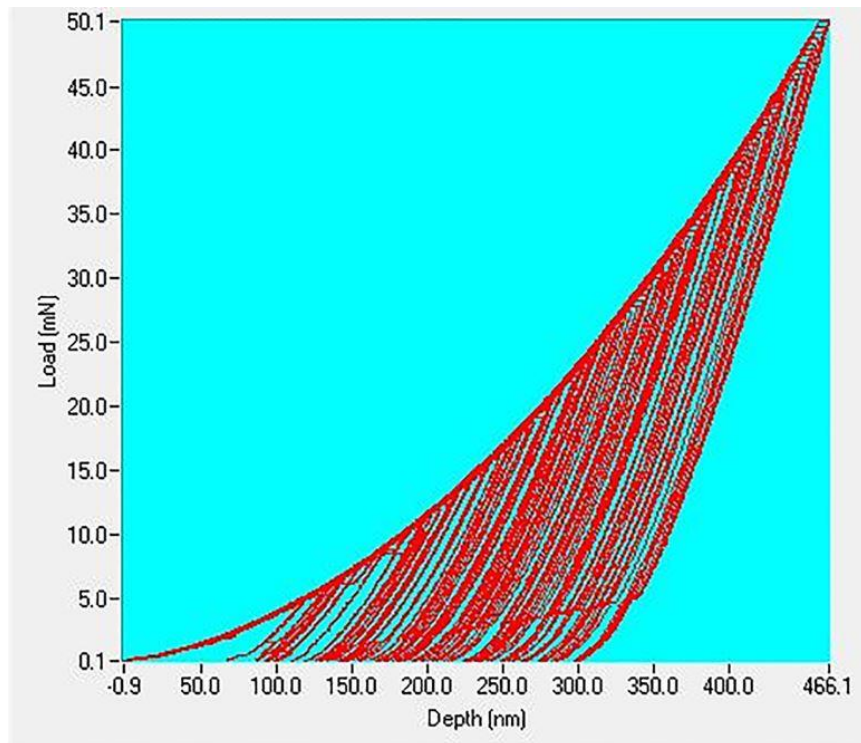


Figure 5-8: Nanoindentation data set for FeCrMnNiC amorphous HEATF.

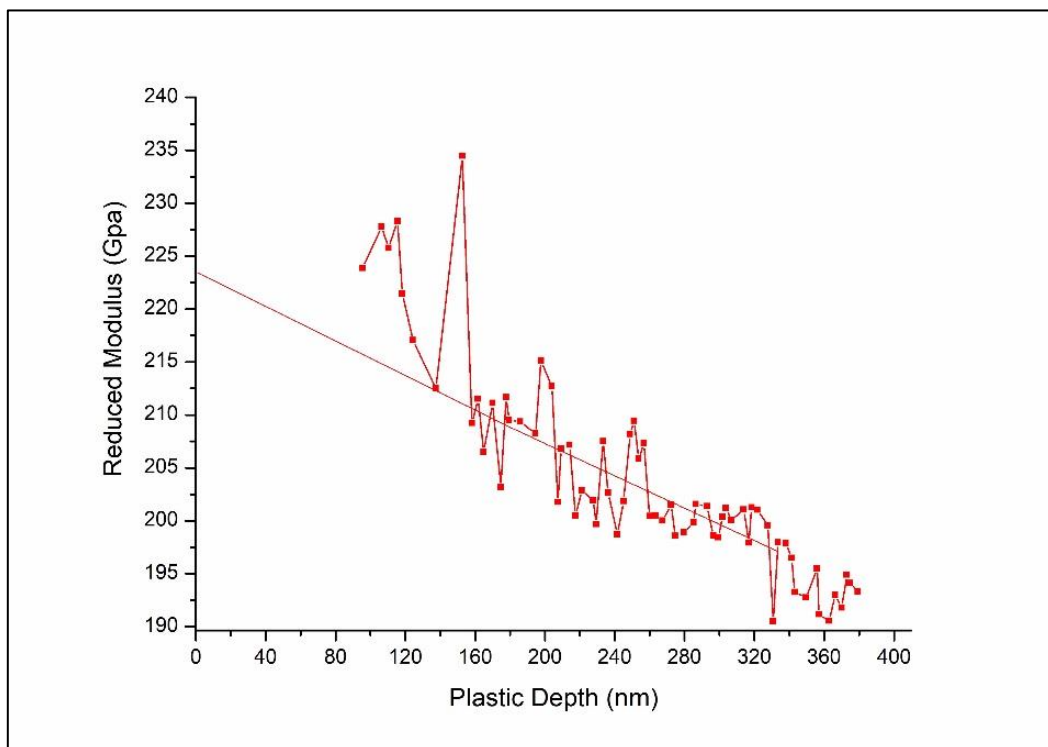


Figure 5-9: Reduced modulus value over plastic depth. The approximation to zero plastic depth was done by a linear fit.

The film's mechanical properties are higher than other amorphous pure metallic systems. For instance, the films are harder than TiVCrAlZr [168] and FeCoNiCuVZrAl [79] HEATF deposited by reactive radio-frequency and direct current magnetron sputtering, respectively. The nanohardness and reduced Young's Modulus [79, 168] for TiVCrAlZr and FeCoNiCuVZrAl were recorded to be 8.2, 8.6 GPa and 128.9 and 153 GPa, respectively.

The addition of covalent bonding elements leads to enhanced mechanical properties. For instance, adding nitrogen to TiVCrAlZr [168] and FeCoNiCuVZrAl [79] thin films resulted in an increment in hardness and reduced Young's modulus, which was recorded to be 11, 12 GPa and 151 GPa, 166 GPa, respectively. This superior hardness and reduced Young's modulus in the present study and nitride films [79, 168] compared to purely metallic high-entropy alloy thin films can be attributed to additional hardening effects due to extensive lattice distortion by the presence of carbon or nitrogen.

5.5 Summary

In this chapter, an equiatomic FeCrMnNiC thin film was successfully synthesised by ion beam sputter deposition. The alloy was successfully deposited on a silicon substrate. In addition, the FeCrMnNiC thin film conformed to be fully amorphous without any crystallinity. The film has a uniform composition and atomic arrangement structure with no element segregation. These could be attributed to the deposition layer by layer at room temperature without heating.

Furthermore, the FeCrMnNiC high entropy thin film alloy exhibits high corrosion resistance and outperforms 304 SS in aqueous NaCl, H₂SO₄ solutions and crude oil at room temperature under atmospheric pressure. This refers to the combination of FeCrMnNiC being a high entropy thin and having an amorphous structure which makes the FeCrMnNiC HE TF alloy has a higher corrosion potential, less corrosion current density, also a higher OPC (open circuit potential), and less pitting potential. However, 304 SS has a crystalline structure where the corrosion prefers to occur, as well as relying on the Chromium content, which makes the passive layer break down after some time. The FeCrMnNiC HE TF alloy demonstrates high hardness of 12.3 Gpa and reduced Young's modulus of 222 GPa. It is proposed that the FeCrMnNiC amorphous thin film can be used to protect mild steel in demanding environments such as oil and gas exploration and procession'' [111].

6 Chapter6: “Corrosion performance and mechanical properties of FeCrSiNb amorphous equiatomic HEA thin film.”

This chapter is a verbatim copy of the publication: Muftah, W., Allport, J., & Vishnyakov, V. (2021). Corrosion performance and mechanical properties of FeCrSiNb amorphous equiatomic HEA thin film. *Surface and Coatings Technology*, 422, 127486.

6.1 Chapter overview

The most commonly used alloys in the oil and gas field are based on chromium and nickel content as they provide a good protective passive layer to protect the surface from corrosion. However, this passive layer is only effective up to a certain point and time in the presence of harsh environments such as CO_2 and H_2S . By breaking down the passive layer, the material surface becomes weak and susceptible to corrosion, where pitting starts to occur. This leads to a failure of the material surface, which is a big problem for petroleum applications. [4, 30, 32].

In this chapter, we aim to solve this problem by studying a quaternary FeCrSiNb equiatomic amorphous HEA thin film amorphous equiatomic. FeCrSiNb HEA thin film amorphous has not been reported yet by other researchers. The composition contains elements of Cr, Si and Nb, which can increase the corrosion resistance of the HEA.

6.2 Materials and methods

An ion beam sputter deposition was used to synthesise and deposit the thin film alloy on silicon (100 orientated wafers) and optically polished silica substrates. The deposition process was fully outlined in earlier work [151, 169]. Silicon wafers were cleaved into 1 square inch pieces and then carefully dusted with a lint-free cloth and compressed air. The silica glass, 1 square inch pieces, was used as delivered from the manufacturer without additional cleaning.

The elements chosen for this work were Fe, Cr, Si and Nb in sheet shapes. The positions of the targets were adjusted several times towards the substrate to achieve the equiatomic composition. The deposition was conducted under stable parameters of current, pressure and temperature. The base system pressure was 2.2×10^{-4} Pa, and the Argon partial pressure in the deposition chamber during the deposition system was about 3.3×10^{-2} Pa. The deposition was done at room temperature, aiming to achieve the amorphous structure. In the deposition chamber, the targets were cleaned via the plasma for around 30 minutes before starting the deposition on the substrate. This avoids sputtering contaminants left on the target's surface while substrate exchanges. The thickness of the thin film after around 120 minutes was measured by the FIB (focused ion beam) sectioning method to be approximately 1.5 microns. According to Galvanizers Association, the coating thickness on steel varies from 30-80 microns depending on its thickness (from 1.5mm to 6 mm). However, it depends on the application's length, the alloy's composition, and the tests conducted. Therefore, the thickness of the coating should be agreed upon between the provider and the company [170].

An FEI Quanta FEG250 Scanning Electron Microscope (SEM) was used for microstructural observation to study the thin film surface. Energy-dispersive X-ray spectroscopy (EDX) using Oxford Instruments was employed to determine the chemical composition. The film's crystal structure was investigated using X-Ray Diffraction (XRD) Bragg Brentano configuration on a Bruker D2 Phaser instrument and Measurement Center 4.0 software. In addition, a

Transmission Electron Microscope (TEM, Hitachi-9500.) sample was made by Focused Ion Beam (FIB), and Selected Area Diffraction (SAD) was utilised to examine the atomic structure thoroughly. 300 keV electron beam was used for TEM analysis.

Corrosion tests were performed using the potentiodynamic polarization technique in a three-electrode cell setup. The specimens, deposited on silicon, were set up as working electrodes (with an exposed area of 0.5 cm^2), with a platinum counter electrode and using a saturated calomel electrode as the reference. The tests were carried out in 0.6 M NaCl and H_2SO_4 solutions. Both solutions were purged with nitrogen to remove dissolved oxygen. In addition, the test was performed on Libyan crude oil. The measurements were performed at room temperature and under atmospheric pressure. The potential and current were measured employing an Autolab potentiostat fitted with Nova 1.10 software. According to ASTM International (American Society for Testing and Materials) standards, the scanning rate of each test was set at 1 mV/s. Open Circuit Potential (OCP) measurements were performed for around half an hour (30 min) to achieve a stable potential. Polarization measurements were scanned between -0.1V and 1.2V. Corrosion parameters: corrosion potential (E_{corr}), corrosion current density (i_{corr}), and passivation regions were obtained by the linear fit technique of polarization curves. For a comparison, stainless steel type 304 samples were used under the same conditions.

For measuring the mechanical properties of the amorphous equiatomic FeCrSiNb HEA thin film deposited on silicon, hardness and modulus were determined by a Nanoindentation system from Micro Materials Ltd, UK. A Berkovich nano-indenter was utilised to apply a ramped load up to a maximum value of 50 mN.

6.3 Results and discussion

6.3.1 Microstructure

Figure 1 presents the data for a FeCrSiNb thin film synthesised by an ion beam depositing system. A Backscatter Electron (BSE) image was taken at high magnification and is shown in fig.1 (a). The main purpose of the BSE image is to clarify whether the elements are distributed uniformly or if there is any elemental or phase separation which will appear as contrast variation. In this case, the BSE image confirms that the microstructure of FeCrSiNb thin film is homogeneous and uniform. The Energy-dispersive X-ray spectroscopy (EDX) quantification showed that the alloy has an equiatomic composition, as evident in Fig.6.1 (b).

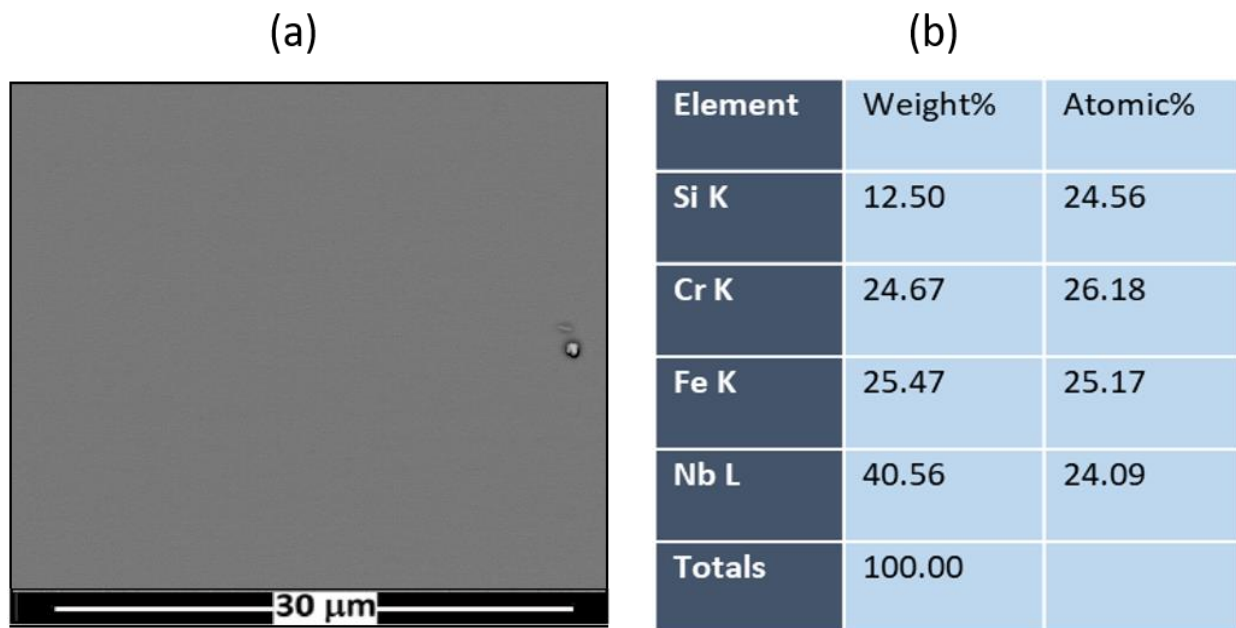


Figure 6-1: SEM analysis of the amorphous equiatomic FeCrSiNb high entropy alloy thin film. (a): BSE image microstructure image. (b): chemical composition of HEA thin film.

Element mapping of the FeCrSiNb thin film is presented in Fig. 6.2. As it can be seen from the mapping, all the elements are distributed uniformly and homogeneously.

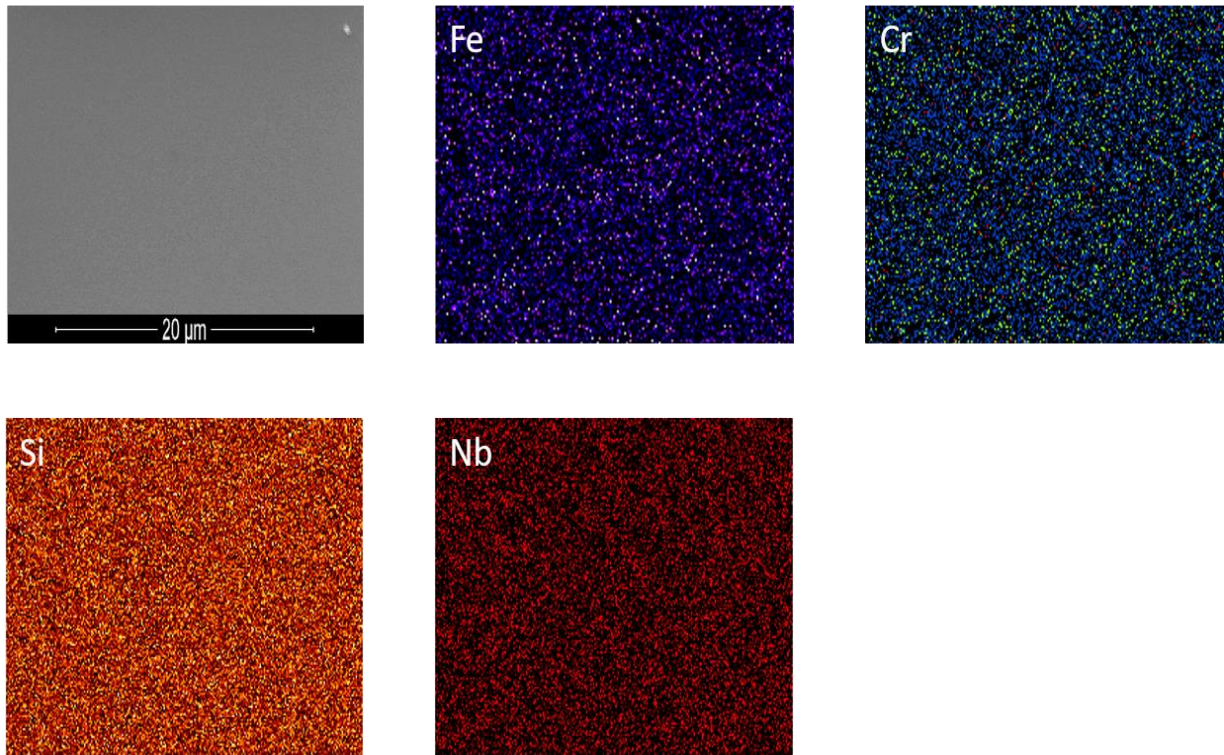


Figure 6-2: EDX mapping of the amorphous equiatomic FeCrSiNb HEA thin film.

EFTEM (Energy filtered TEM) imaging of FeCrSiNb thin film was performed to confirm the absence of element segregation. The elemental maps prove a uniform distribution for all elements (iron, chromium, silicon and niobium) without any element segregation or precipitation, as presented in Fig. 6.3.

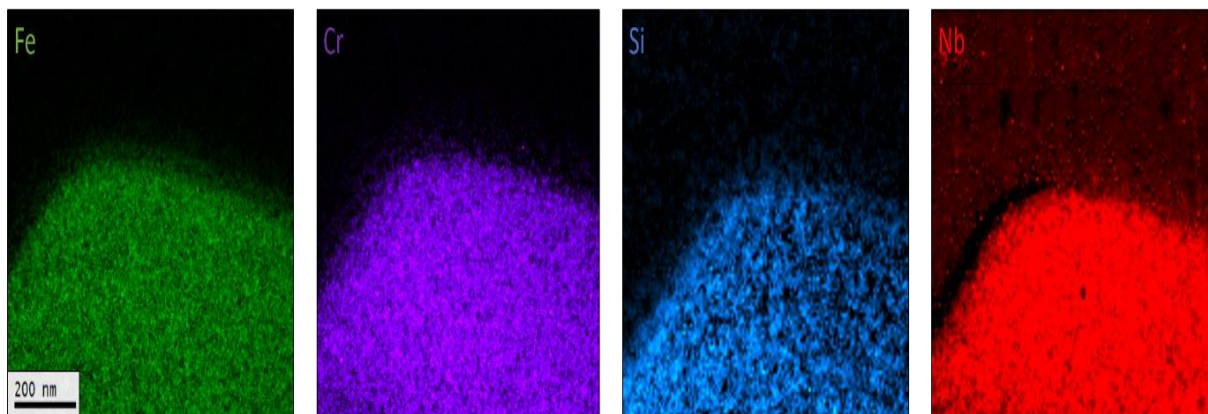


Figure 6-3: EFTEM images of the amorphous equiatomic FeCrSiNb HEA thin film.

The film was deposited on silica glass to assess the crystalline structure of the alloy. The X-Ray diffraction pattern (XRD) demonstrates that the FeCrSiNb HEA thin film possesses no crystalline structure. The XRD pattern is characteristic of an amorphous material, as displayed in Fig. 6.4. The main film diffraction peak at around 44° is very broad and has a low intensity which is a typical amorphous material XRD. The second peak at 21° is related to the silica substrate, as confirmed in Fig. 6.5.

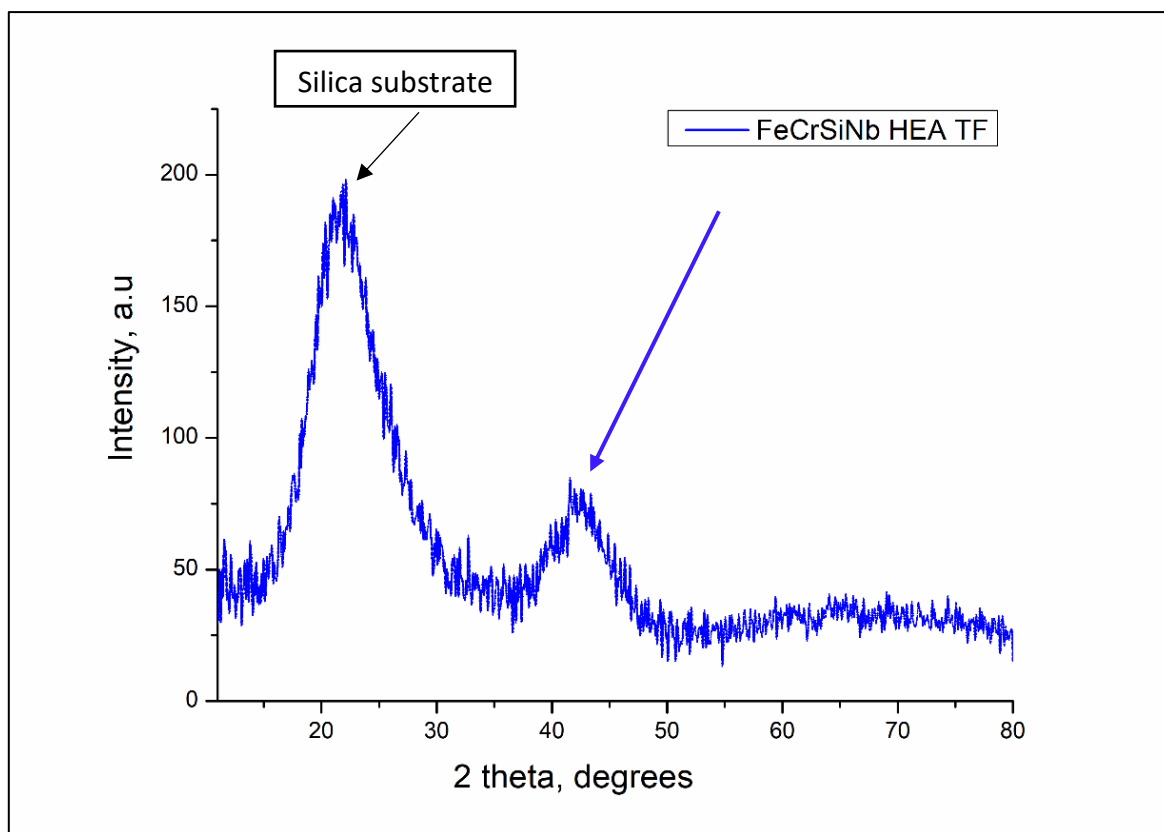


Figure 6-4: XRD pattern of the FeCrSiNb thin film on a silica substrate.

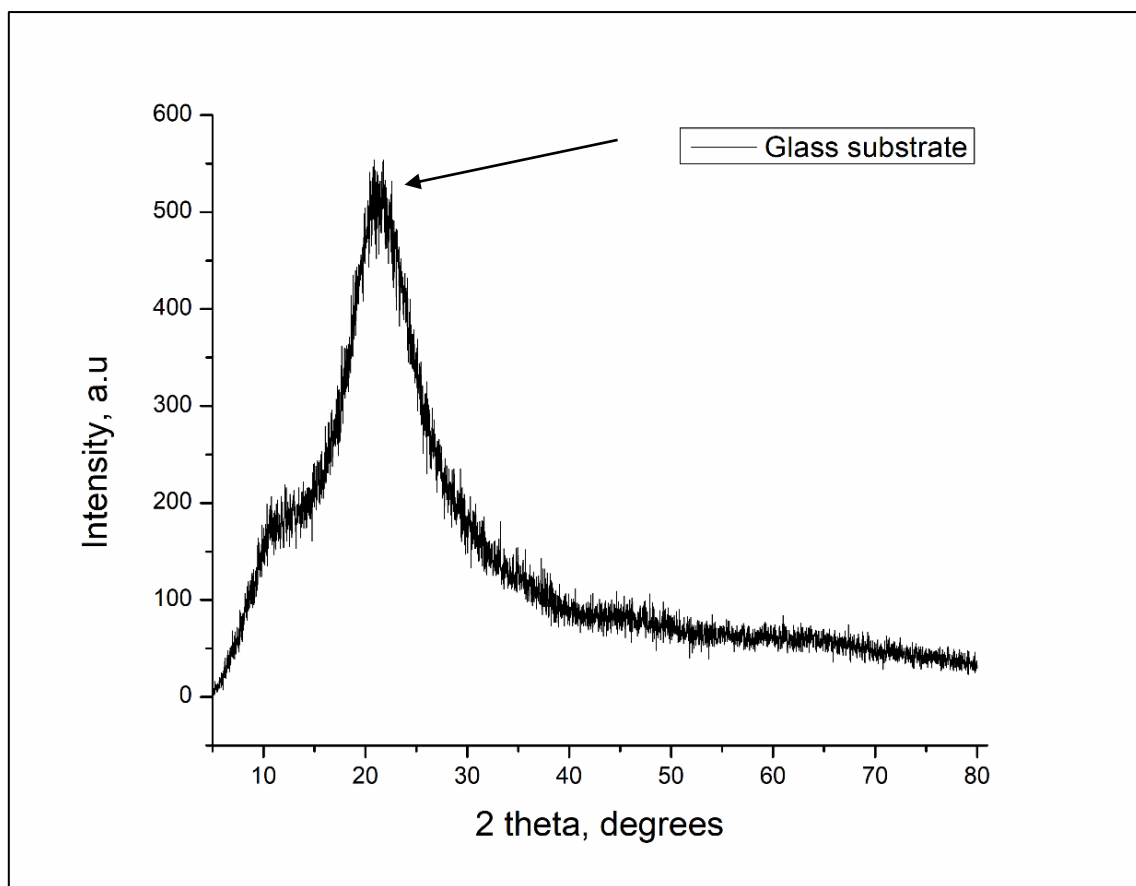


Figure 6-5: XRD pattern of the silica glass substrate.

For further examination of the amorphous structure of the amorphous equiatomic FeCrSiNb high entropy alloy thin film, a FIB (Focused Ion Beam) sample was studied in a Transmission Electron Microscope (TEM). Fig. 6.6 (a) shows a bright field image (BFTEM) high-resolution TEM image of a high entropy thin film synthesised by ion beam sputtering. Fig. 6.6 (b) is the selected area diffraction (SAED) of the thin film taken from the marked area and confirms the formation of a fully amorphous structure by the presence of only diffraction rings without any crystallinity patterns.

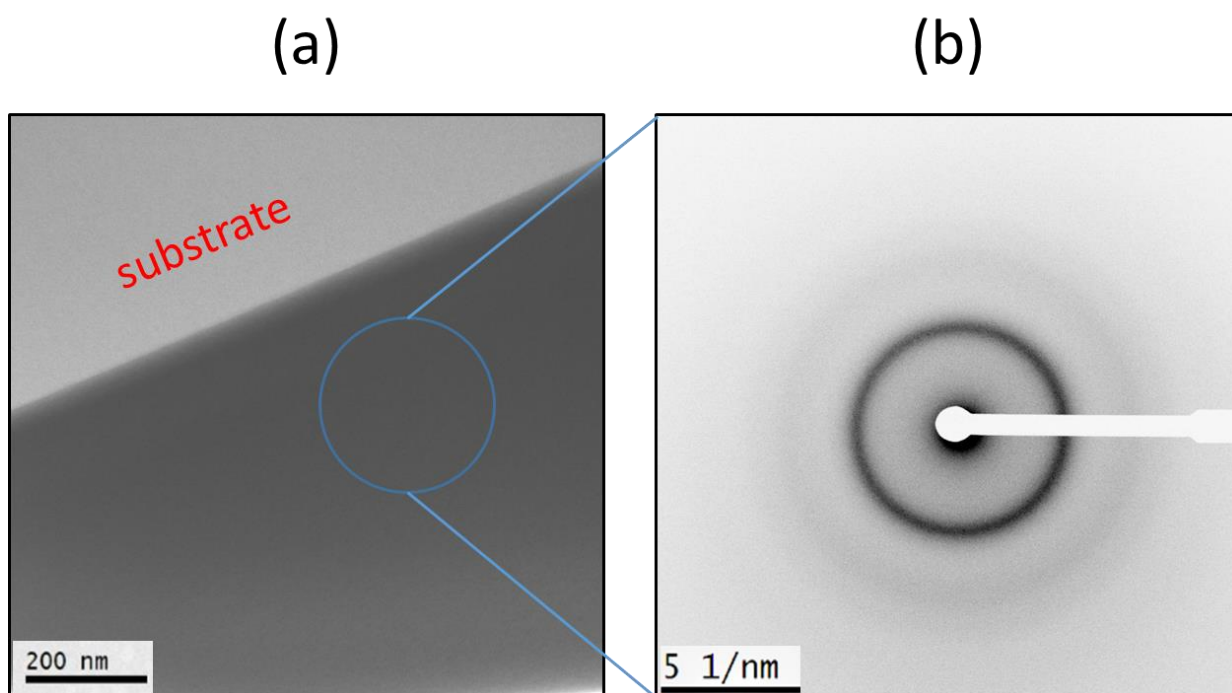


Figure 6-6: (a): BFTEM images of the amorphous equiatomic FeCrSiNb high entropy alloy thin film synthesised by ion beam sputtering, and fig. 6 (b) SAED images of amorphous film taken from the marked area.

All the results mentioned above from the SEM-BSE, EDX mapping show that the amorphous equiatomic FeCrSiNb high entropy alloy thin film synthesised by ion beam sputter deposition is a single phase and uniform alloy. This is mainly attributed to the layer-by-layer deposition carried out under stable conditions of temperature and pressure [151, 169]. The formation of a dense and amorphous alloy has been confirmed by XRD and TEM results. The main reason for this is the transformation from an ionic state to a solid state, which led to a significantly high cooling rate at the deposition chamber, and the condensation energy is released [171]. The amorphization of high entropy thin films could be attributed to the high mixing entropy and large atomic size difference. The high mixing entropy increases the mutual solubility of different elements in thin films and impedes the formation of phase separation [58]. Also, the

presence of Niobium has played a vital role in improving the amorphization process of the alloy. A study of the phase evolution in NbCoCrCuFeNi thin film deposited by magnetron sputtering has demonstrated that the film structure changed from a crystalline to an amorphous structure with a higher Nb content [172].

6.3.2 Corrosion tests

Figure 6.7 shows a potentiodynamic polarisation curve of the amorphous equiatomic FeCrSiNb high entropy alloy thin film carried out in the three-electrode electrochemical cell in 0.6 M NaCl (3.5 % sodium chloride) solution under conditions of atmospheric pressure and room temperature. Table 6.1 presents corrosion parameters for FeCrSiNb HEA thin film obtained by a linear fit technique. Figure 6.8 is a potentiodynamic polarisation curve of the amorphous equiatomic FeCrSiNb HEA thin film conducted in 0.6 M H₂SO₄ (sulphuric acid) solution under the same conditions. The obtained corrosion parameters are listed in table 6.2.

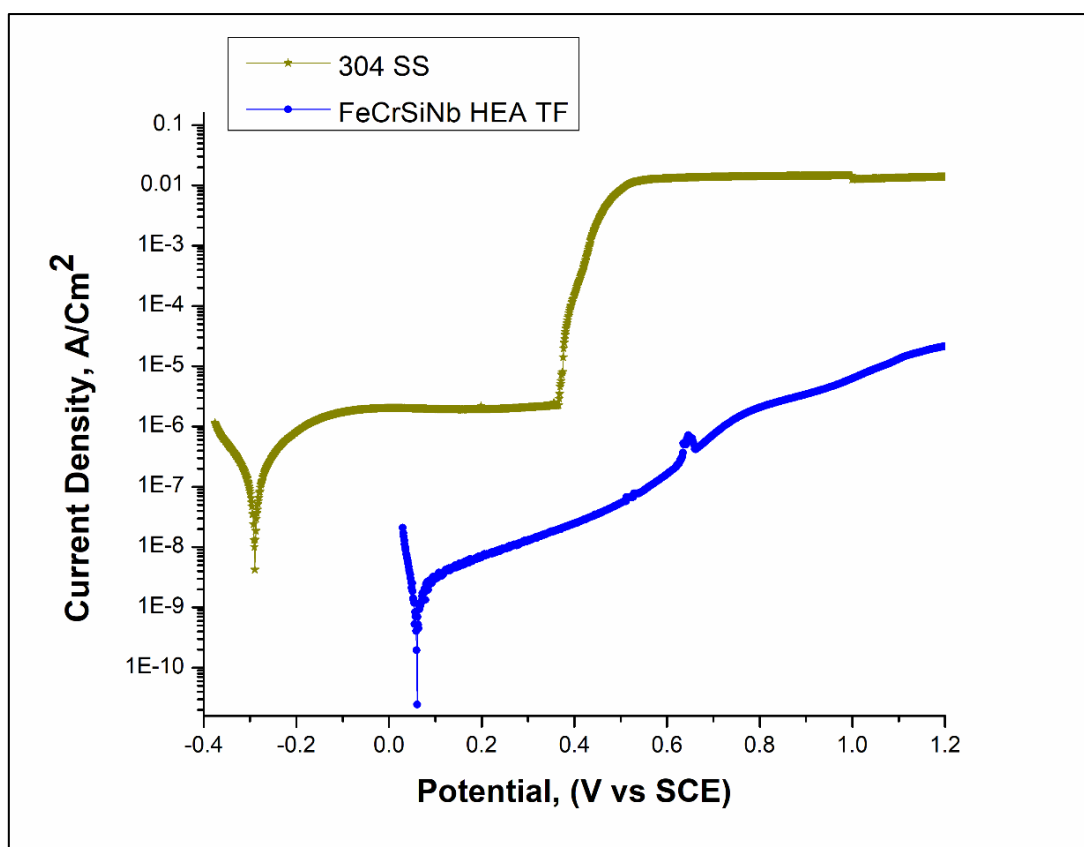


Figure 6-7: polarisation curves of the amorphous equiatomic FeCrSiNb high entropy alloy thin film and 304 SS in 0.6 M NaCl solution.

Table 6-1: the corrosion parameters of FeCrSiNb HEA thin film and 304 SS in 0.6 M NaCl solution.

Sample ID	i_{corr} , A/Cm ²	E_{corr} , V _{SCE}
FeCrSiNb	$8.66 \cdot 10^{-10}$	0.06
304 SS	$1.10 \cdot 10^{-7}$	-0.29

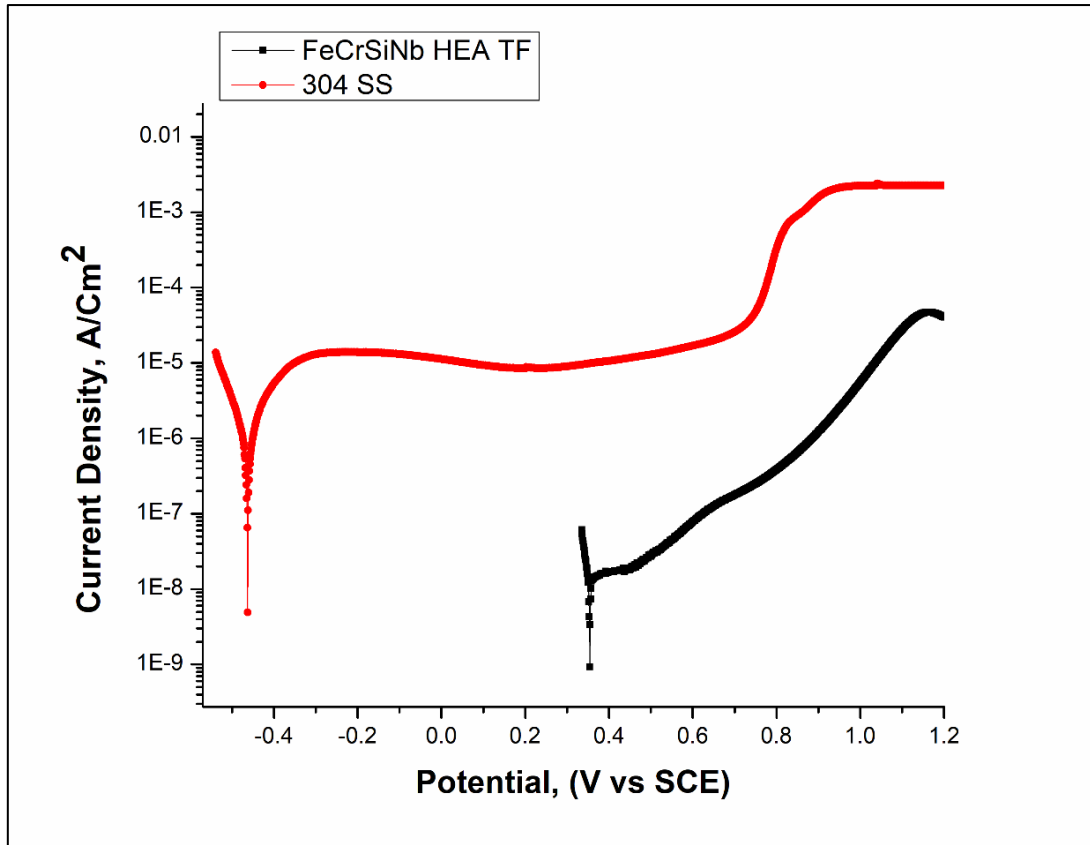


Figure 6-8: polarisation curves of amorphous equiatomic FeCrSiNb high entropy alloy thin film and 304 SS in 0.6 M H₂SO₄ solution.

Table 6-2: corrosion parameters of FeCrSiNb HEA thin film and 304 SS in 0.6 M H₂SO₄ solution.

Sample ID	i_{corr} , A/Cm ²	E_{corr} , V _{SCE}
FeCrSiNb	$1.22 \cdot 10^{-8}$	0.36
304 SS	$4.86 \cdot 10^{-6}$	-0.46

Figure 6.9 displays a potentiodynamic polarisation curve of the amorphous equiatomic FeCrSiNb high entropy alloy thin film carried out in crude oil under atmospheric pressure and room temperature. The obtained corrosion parameters are listed in table 6.3.

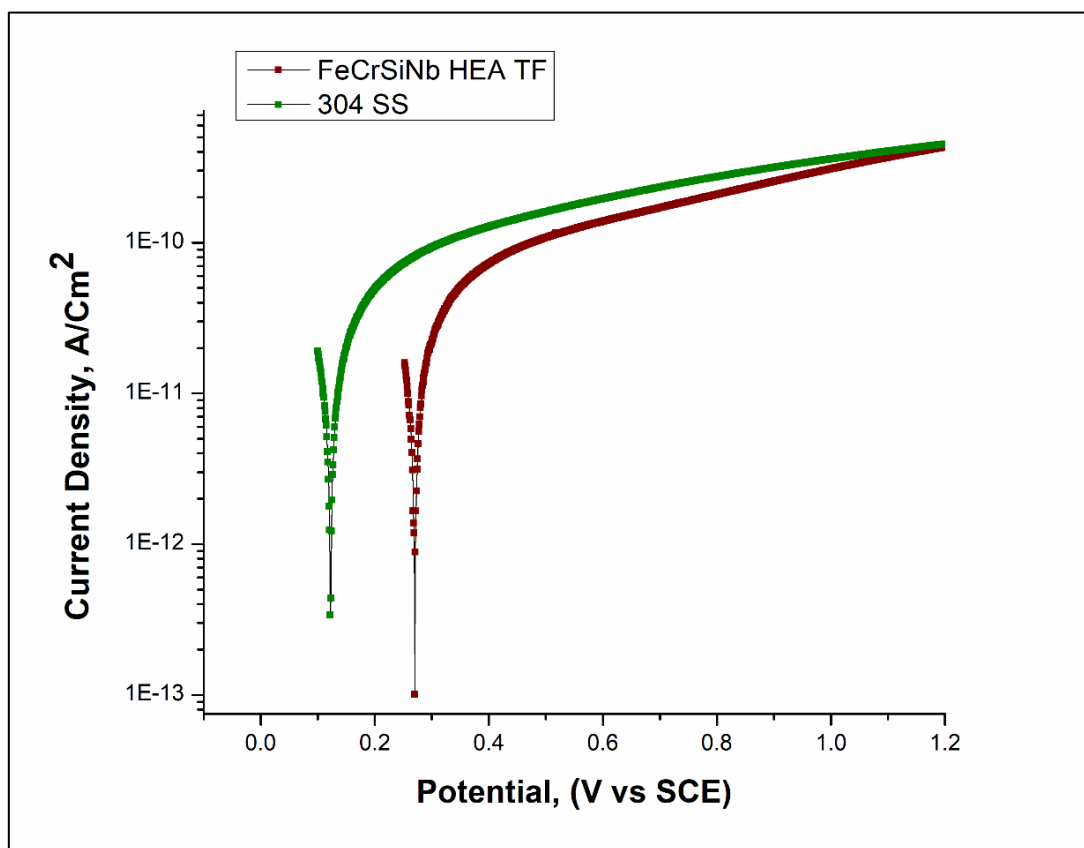


Figure 6-9: polarisation curves of FeCrSiNb HEA thin film & 304 SS in crude oil.

Table 6-3: corrosion parameters of FeCrSiNb HEA thin film and 304 SS in crude oil

Sample ID	i_{corr} , A/Cm ²	E_{corr} , V _{SCE}
FeCrSiNb	8.56×10^{-12}	0.27
304 SS	9.91×10^{-12}	0.12

It is well known in electrochemistry, when analysing the corrosion performance of a material, that when there is a smaller current density and a higher corrosion potential, the corrosion

resistance is better. In addition, the passivation layer occurs when the corrosion potential shifts to the positive side, continuing the corrosion current density at the same value or gradually increasing [145, 173, 174].

As it can be seen from the polarisation curve in fig. 6.7 and corrosion parameters of the FeCrSiNb HEA thin film and 304 SS in 0.6 M NaCl solution in the table. 6.1, the FeCrSiNb HEA thin film has a corrosion potential of 0.06 V and corrosion current density of 8.66×10^{-10} A/cm², compared to -0.29 V and 1.1×10^{-7} A/cm² for 304 SS. From fig. 6.8 and table 6.2, the corrosion potential of the HEA thin film is 0.36 V, and the corrosion current density is 1.22×10^{-8} A/cm² in 0.6 M H₂SO₄ solution, whereas 304 SS has -0.46 V and 4.86×10^{-6} A/cm².

In addition, 304 SS shows a presence of passive layers, then protective oxide failure happens, and pitting occurs suddenly in both solutions. In the case of amorphous equiatomic FeCrSiNb HEA thin film, the corrosion current density is increasing slowly, non-exponentially (where the obvious pitting occurs) and reaches a stable area at around 10^{-5} A/cm² of corrosion current density, which is still small value at around 1.2 V of corrosion potential in both solutions. In contrast, 304 SS at the same value 10^{-5} A/cm² is pitting at around 0.38 V in NaCl and around 0.76 V in H₂SO₄ solutions. This reflects that the corrosion resistance of FeCrSiNb HEA thin film to corrosion is much higher than 304 SS.

In the case of the crude oil test, the FeCrSiNb HEA thin film exhibited a corrosion potential of 0.27 V, higher than that for 304 SS of 0.12 V. Furthermore, the corrosion current density of the amorphous equiatomic FeCrSiNb HEA thin film and 304 SS showed relative values with a small advantage for the thin film alloy (8.56×10^{-12} , 9.91×10^{-12} A/cm²), respectively. As a result, the amorphous equiatomic FeCrSiNb high entropy alloy thin film has an excellent corrosion resistance nobler than 304 SS in NaCl, H₂SO₄ solutions, and crude oil.

This can be attributed to several reasons. Generally, the behaviour of high entropy alloys as they have uniform single-phase microstructure with no element separation leads to good corrosion resistance [59, 82]. Moreover, the cocktail effect of existing elements such as Cr, Si and Nb can create a passive layer to protect the material from corrosion [159, 162, 175]. The higher corrosion potential (E_{corr}) of amorphous equiatomic FeCrSiNb HEA thin film could be attributed to high entropy alloys undergoing self-passivation at OCP and forming a passive protective film as Shi et al. have stated in AlCoCrFeNi HEA [126, 176]. Furthermore, the amorphous structure with the absence of grain boundaries where the corrosion is more likely to happen could enhance the surface resistance to corrosion of the thin film alloy [164]. This has been discussed and proved in earlier work, where the amorphous equiatomic FeCrMnNiC HEA thin film displayed excellent corrosion resistance ($E_{\text{corr}}=0.07$ V, $i_{\text{corr}}=2.5\text{E}^{-10}$ A/cm²) in NaCl solution under the same conditions [111].

6.4 Mechanical properties

The hardness measurement of the thin film was carried out employing nanoindentation. The load was slowly increased from 10 to 50 mN. Loading and unloading were done at a fixed time – 20 sec/loading/unloading, the dwell period at maximum load was 60 sec, and thermal drift correction was done post-indentation for 60 sec.

Hardness measurement with the range of loads allows accounting in principle for various effects. At low loads, the surface effect, oxide layers, for instance, can be identified. It can be seen on Fig. 6.10 that the penetration curves at low loads are continuously smooth, which indicates negligent surface oxide development. The hardness is then can be averaged over measured data. The result showed that amorphous equiatomic HEA thin film has a hardness of 15 ± 1.2 GPa. The penetration depth is higher than usually used $1/10^{\text{th}}$ of film thickness but is rightful as silicon substrate has not so dissimilar to the thin film mechanical values. As shown from the graph, there is no change in the behaviour of the thin film result and no drop in the

value, which means the test is still going smoothly without an impact from the Si substrate. An experimental study was done on the impact of two different indentation depths between 500 nm and 1 μm on the Si substrate. The results did not observe any impact on the substrate and no changes in the mechanical properties of the thin film. Fig. 6.11 displays the value of reduced Young's modulus over plastic depth. As expected, smooth decay with plastic penetration depth also enforces the rightfulness of negligible substrate influence on measured values.

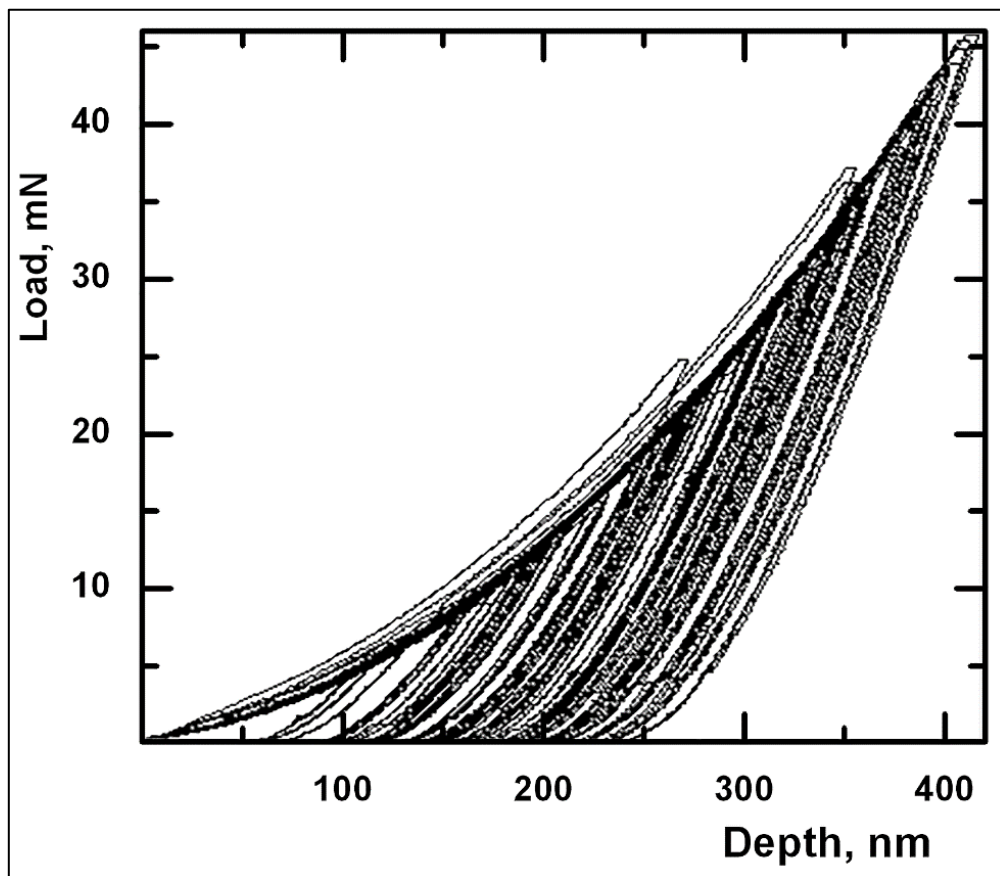


Figure 6-10: Nanoindentation data for amorphous equiatomic FeCrSiNb HEA thin film.

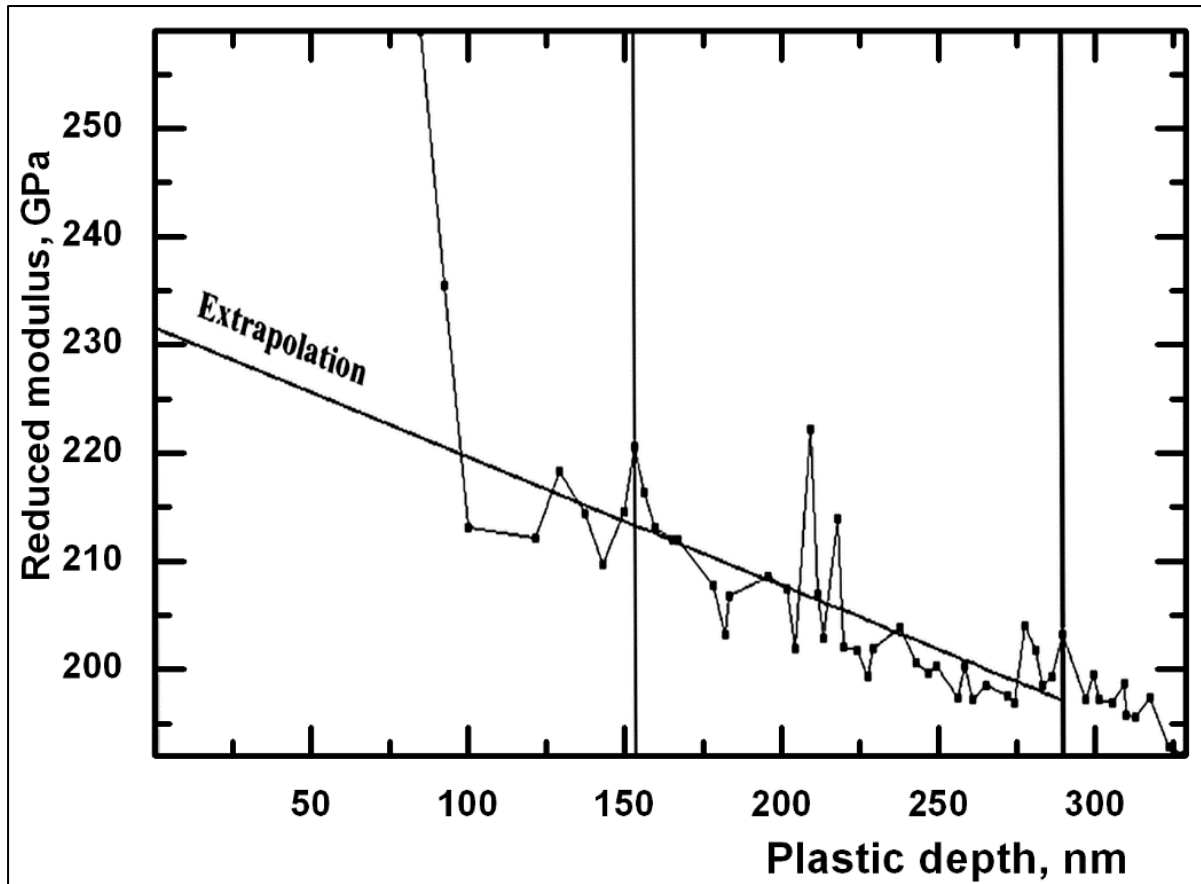


Figure 6-11: Reduced Young's modulus of amorphous equiatomic FeCrSiNb HEA thin film.

The value of the reduced Young's modulus should be determined at zero loads. This is done by linear extrapolation following the international standard. In our case, Young's modulus value is around 229 ± 12 GPa, as seen in Fig. 6.10.

The obtained mechanical properties in this work were superior to other high entropy thin film alloys. For example, the amorphous equiatomic FeCrSiNb HEA thin film is harder than CoCrFeNi [78] NbTiAlSiZrNx [177] crystalline and FeCoNiCuVZrAl [79] amorphous high entropy alloy films. The crystalline HETF alloys [78, 177] showed hardness of 8.5 & 12.4 GPa

and Young's modulus of 161.9 & 169 GPa, respectively. In contrast, the hardness and Young's modulus of amorphous equiatomic HEA thin film were 12 GPa and 166 GPa [79].

These superior properties of high hardness and reduced modulus in this work are produced due to the uniform and single-phase structure's effect, which led to the bonding structure's strengthening [82]. Furthermore, it could be possible to suggest that the presence of Niobium played a significant role in improving hardness as it was examined in AlCoCrFeNiNb_x High entropy thin film alloy [178].

6.5 Summary

In conclusion, ion beam sputter deposition successfully prepared a new equiatomic FeCrSiNb amorphous high entropy thin film alloy. The alloy was confirmed to be equiatomic and amorphous using several techniques such as SEM, EDX, XRD and SAED. Corrosion tests were carried out in 0.6 M sodium chloride (NaCl), sulphuric acid (H₂SO₄) solutions, and crude oil by using a three electrodes electrochemical cell. The corrosion parameters proved that the FeCrSiNb HEA thin film is nobler than the 304 SS, as it displayed a higher corrosion potential in NaCl, H₂SO₄ and crude oil. Even though 304 SS is categorised as good corrosion-resistant material, it shows early pitting due to its sensitivity to seawater and H₂SO₄ in many cases, which is unfavourable in the oil field as it requires regular maintenance. This cannot be done in many applications, especially offshore. That is why it is suggested to use high entropy thin films as they showed high corrosion potential with longer passivation zones, making them useable for longer. The amorphous equiatomic FeCrSiNb HEA thin film exhibited a high hardness at 15 ± 1.2 GPa. The Young's modulus value was observed at about 229 ± 12 GPa'' [179].

**7 Chapter7: Deposit FeCrMnNiC & FeCrSiNb
amorphous high entropy alloys thin films on steel and
conduct corrosion tests in crude oil**

7.1 Chapter overview

In this chapter, FeCrMnNiC & FeCrSiNb amorphous high entropy alloys thin films were successfully deposited on steel substrates. Several characterization methods, such as SEM, EDX, and XRD, were used to investigate the crystal nature and microstructure of the HEAs. In addition, the potentiodynamic polarization method via a three-electrode electrochemical cell was used to conduct corrosion tests in crude oil. This work aims to simulate the oil field by depositing FeCrMnNiC & FeCrSiNb amorphous high entropy alloys thin films on real steel applications and performing the corrosion tests in crude oil.

7.2 Materials and methods

FeCrMnNiC and FeCrSiNb have deposited steel substrates by ion beam sputter deposition at room temperature. The deposition ran for around two hours with a base system pressure of 2.3×10^{-4} Pa and the Ar partial of 3.5×10^{-2} Pa.

The microstructure of both deposited thin film samples was determined by FEI Scanning Electron Microscope (SEM). The chemical composition was investigated by using Energy-dispersive X-ray spectroscopy (EDX). X-Ray Diffraction (XRD) was used to examine the crystal structure to confirm whether the synthesised alloys have a crystalline or amorphous structure.

The corrosion tests were carried out via the potentiodynamic polarization technique using a three-electrode cell system. The samples with an exposed area of 0.5 cm^2 were used as working electrodes. Platinum wire was used as a counter electrode. Finally, a saturated calomel electrode (SCE) was used as a reference electrode. The corrosion tests were performed in Libyan crude oil at room temperature and under surrounding pressure.

The corrosion parameters: corrosion current density (i_{corr}), and corrosion potential (E_{corr}), were obtained from the polarisation curves using Autolab potentiostat controlled by Nova 1.10 software.

7.3 Results and discussion

7.3.1 Microstructure of FeCrMnNiC

Figure 7.1 (a) displays the BSED (backscatter) SEM micrograph of FeCrMnNiC HEA deposited on a steel substrate. Figure 7.1 (b) is the EDX mapping of the elemental composition of FeCrMnNiC in their near equiatomic ratio.

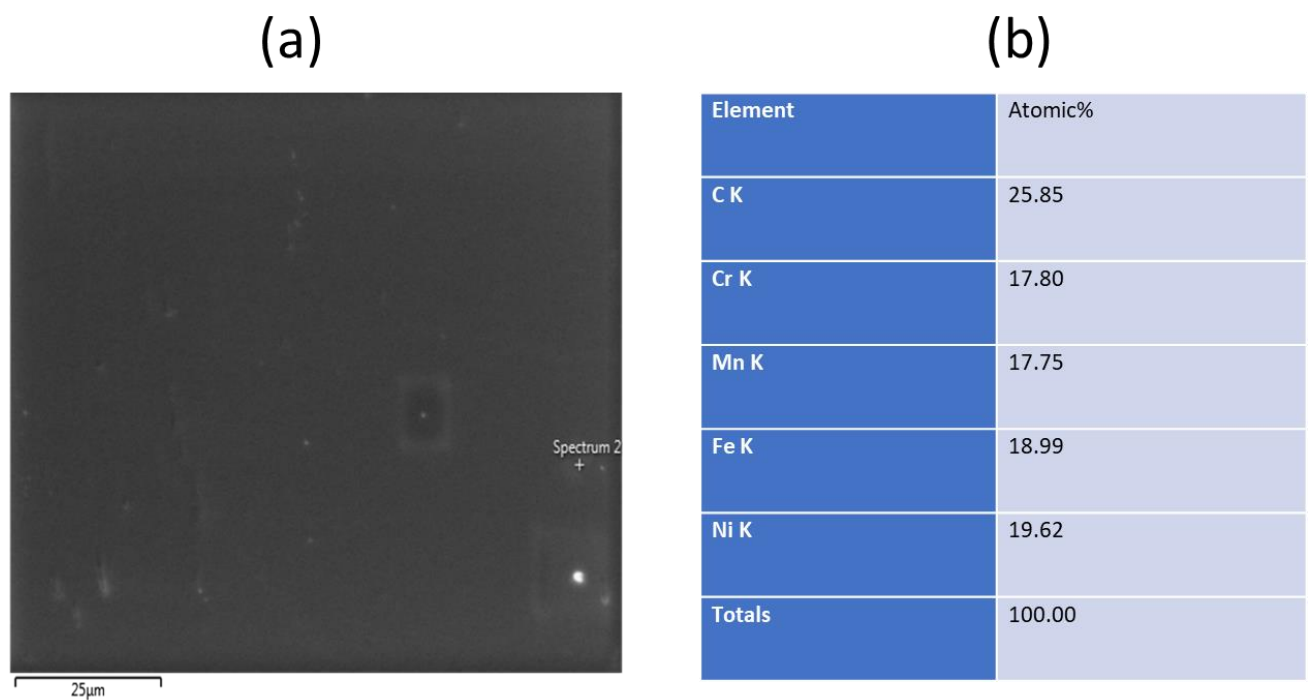


Figure 7-1: (a) BSE surface microstructure image of FeCrMnNiC amorphous HEA thin film alloy deposited on steel, and (b) elemental chemical composition.

The elemental mapping of FeCrMnNiC is shown in Figure 7.2, which confirms the homogenous distribution of Cr, Mn, Fe and Ni without any form of elemental separation.

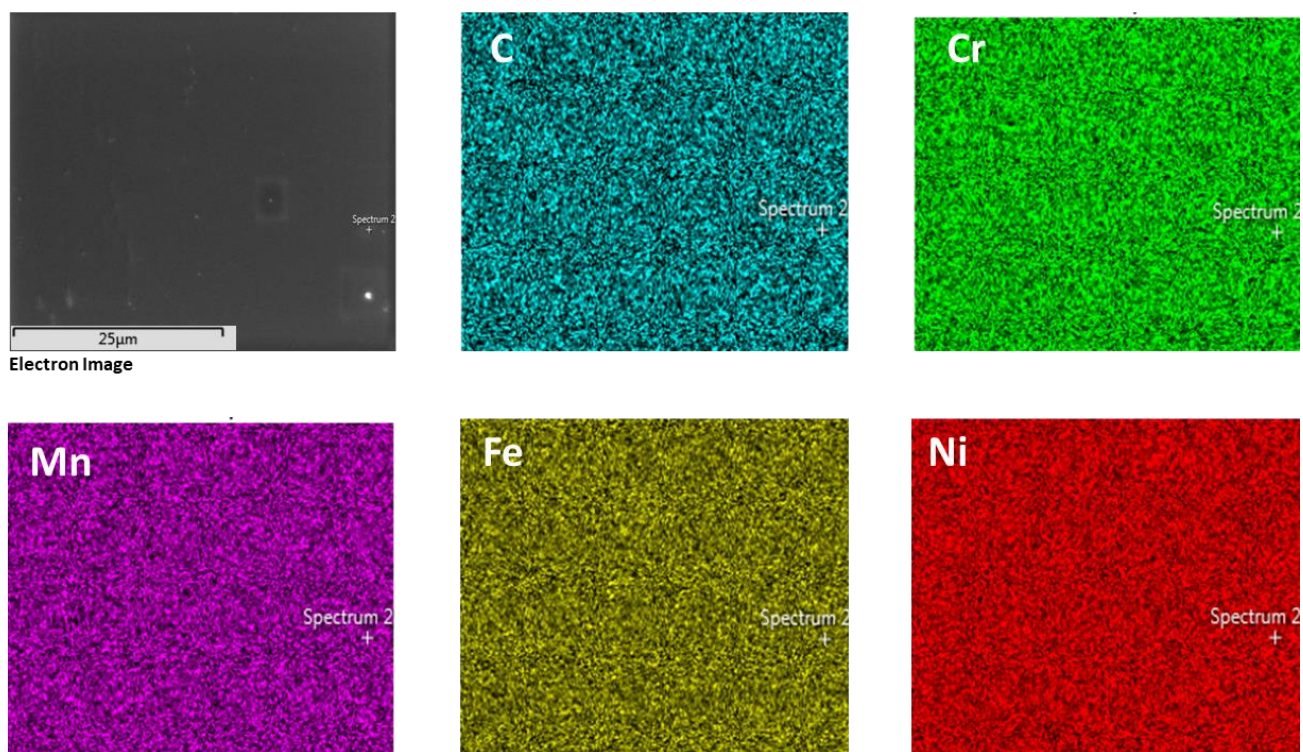


Figure 7-2: elemental mapping of FeCrMnNiC amorphous HEA thin film alloy deposited on steel

Fig. 7.3 XRD spectrum shows that FeCrMnNiC HEA TF deposited on steel is amorphous as the spectrum only presented one wide peak at around 44° without any sharp diffraction peaks. The other two peaks at around 46° and 66° refer to the steel substrate as arrowed and presented in fig 7.4.

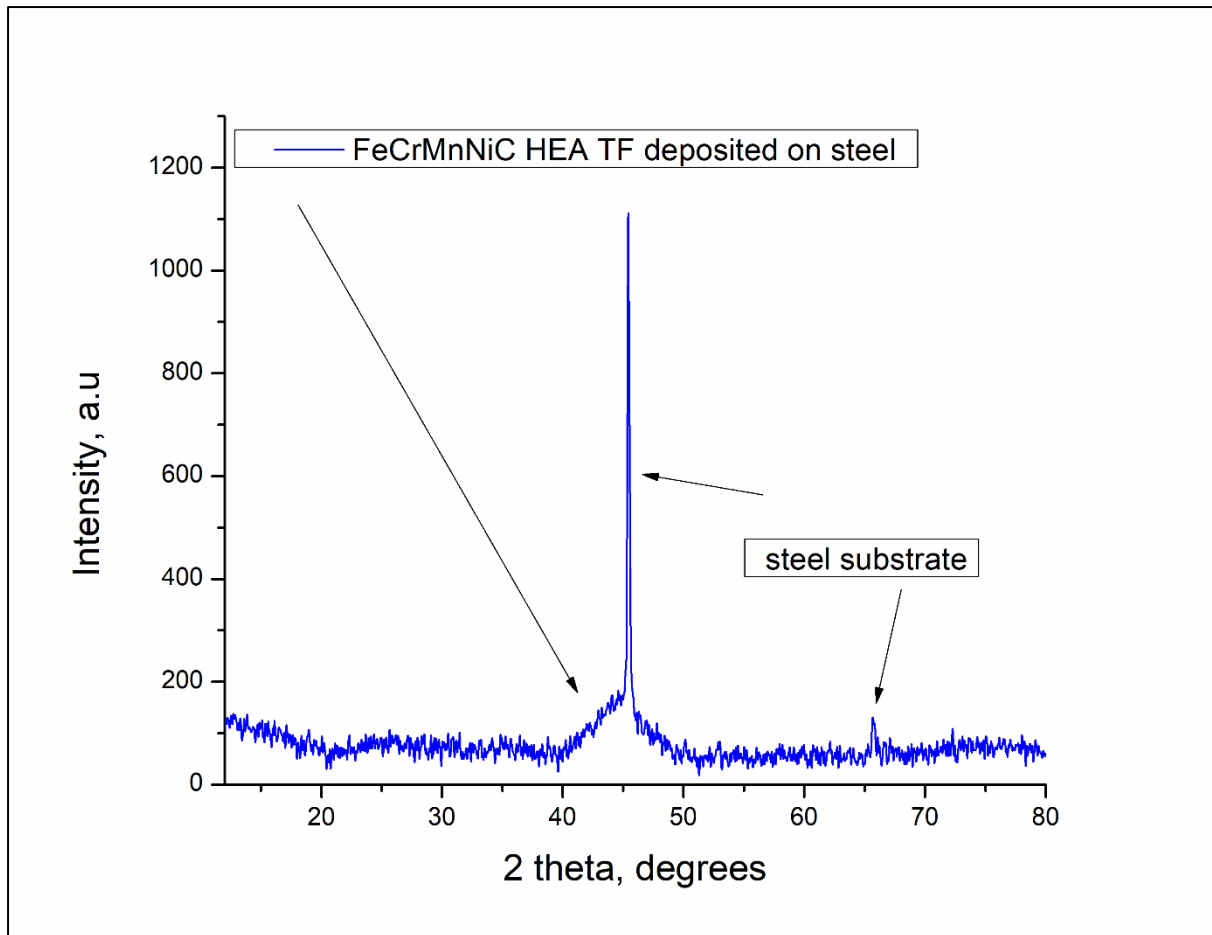


Figure 7-3: XRD pattern of FeCrMnNiC amorphous HEA thin film alloy deposited on the steel.

A crystalline material has long-range periodic order. However, the amorphous material does not have this long-range order. Therefore, the diffraction from amorphous material does not show sharp Bragg peaks. An incident x-ray in a crystal plane on atoms is scattered in a particular orientation to provide a high-intensity narrow peak. However, in amorphous materials, the incident x-ray on atoms in a plane is scattered in random orientations, and due to this random orientation results in a broad peak or background hump [180].

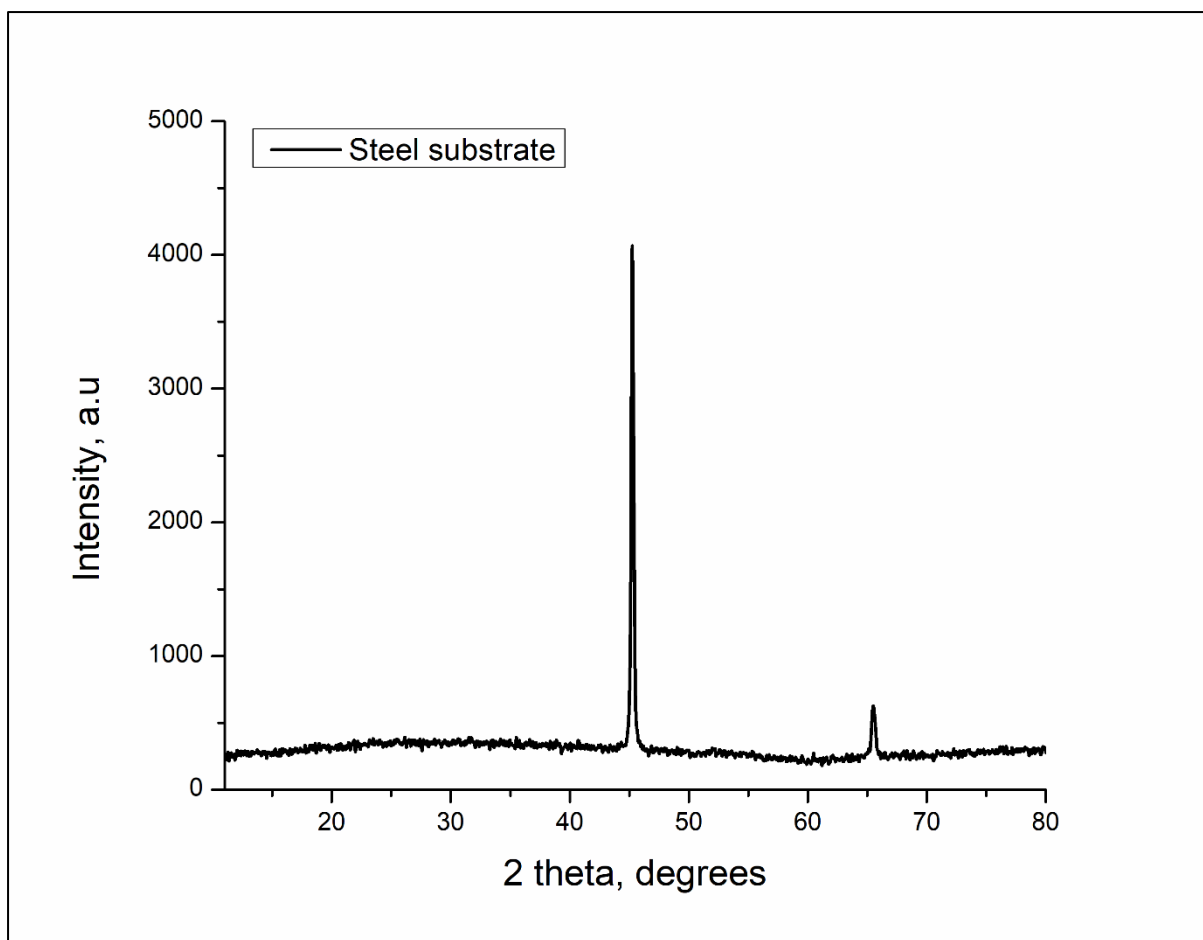


Figure 7-4: XRD pattern of steel substrate.

7.3.2 Corrosion test of FeCrMnNiC in crude oil

Figure 7.5 depicts the potentiodynamic polarisation curves of FeCrMnNiC HEA deposited on steel and SS304 in crude oil. Corrosion parameters (corrosion potential & corrosion current density) are seen in Table 7.1. The FeCrMnNiC alloy has a higher corrosion potential (0.19x higher) than that of SS304 (0.12 V), while the corrosion current density of FeCrMnNiC alloy is $5.30 \times 10^{-12} \text{ A/Cm}^2$ which is smaller than 9.91×10^{-12} for SS304. This suggests better corrosion resistance of the FeCrMnNiC HEA deposited on steel than that in SS304 in crude oil at normal temperature & pressure.

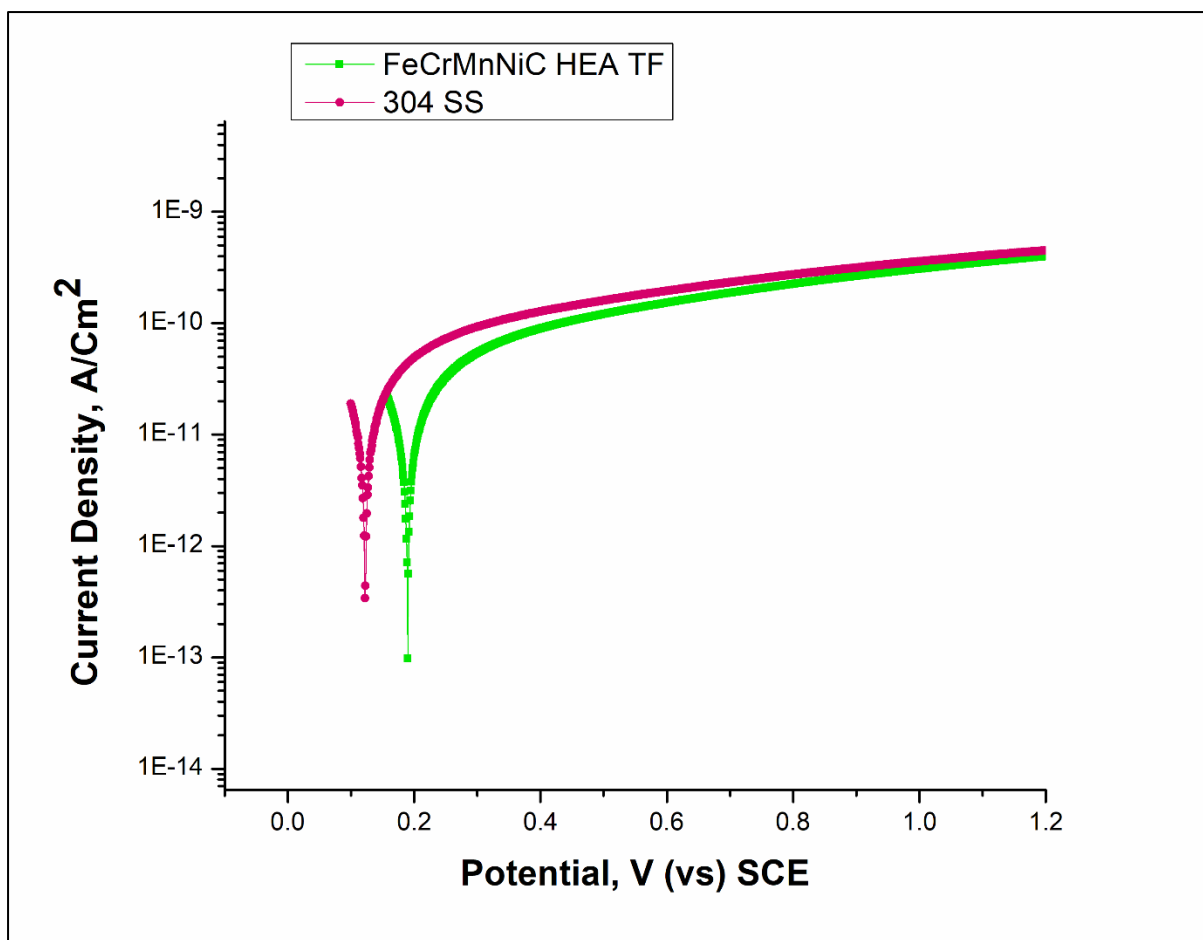


Figure 7-5: polarization curves of FeCrMnNiC HEA thin film deposited on steel & SS304 in crude oil.

Table 7-1: corrosion parameters of FeCrMnNiC HE TF alloy deposited on steel and SS304 in crude oil.

Sample ID	i_{corr} , A/Cm ²	E_{corr} , V
FeCrMnNiC	$5.30 \cdot 10^{-12}$	0.190
SS304	$9.91 \cdot 10^{-12}$	0.120

7.3.3 Microstructure of FeCrSiNb

Figure 7.6 (a) displays the BSED image of FeCrSiNb HEA deposited on a steel substrate, while Figure 7.6 (b) is the chemical composition determined using EDX analysis which confirms that FeCrMnNiC HEA is equiatomic.

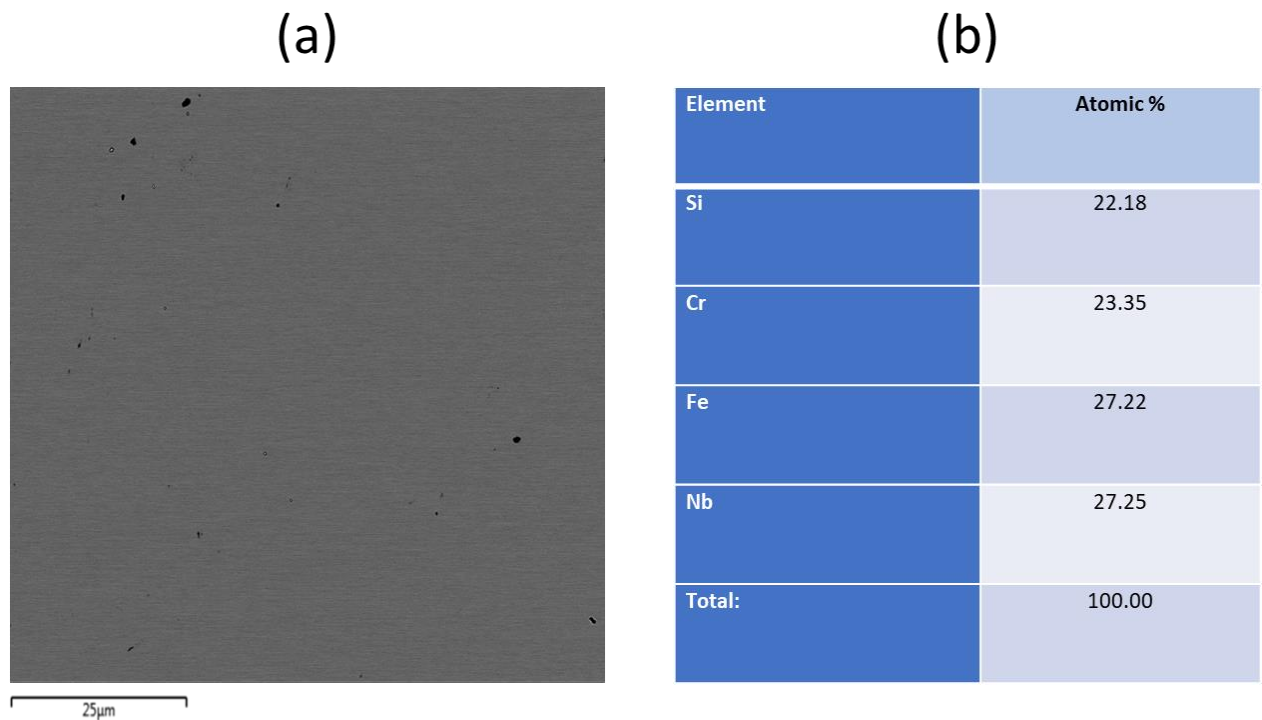


Figure 7-6: (a) BSE microstructure image of FeCrSiNb amorphous HEA thin film alloy deposited on steel, (b) elemental chemical composition.

Fig. 7.7 displays the elemental mapping of FeCrSiNb amorphous HEA TF. The elemental mapping confirms that the FeCrSiNb alloy has a single-phase microstructure without separations or segregations.

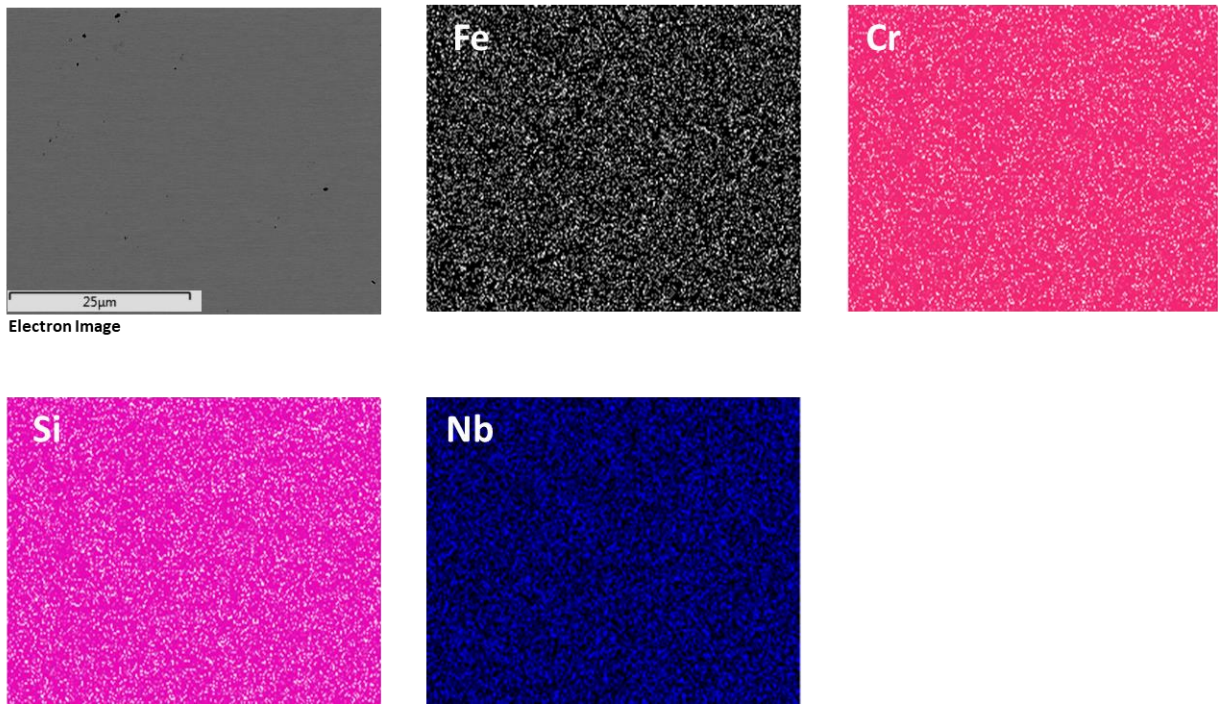


Figure 7-7: elemental mapping of FeCrSiNb amorphous HEA TF

Fig. 7.8 represents the XRD pattern of FeCrSiNb HEA TF deposited on the steel. As shown in the figure, there is a broad peak at around 43° , which refers to the typical pattern of amorphous structure. The peaks at 46° and 66° represent the steel substrate, as shown in fig. 7.4.

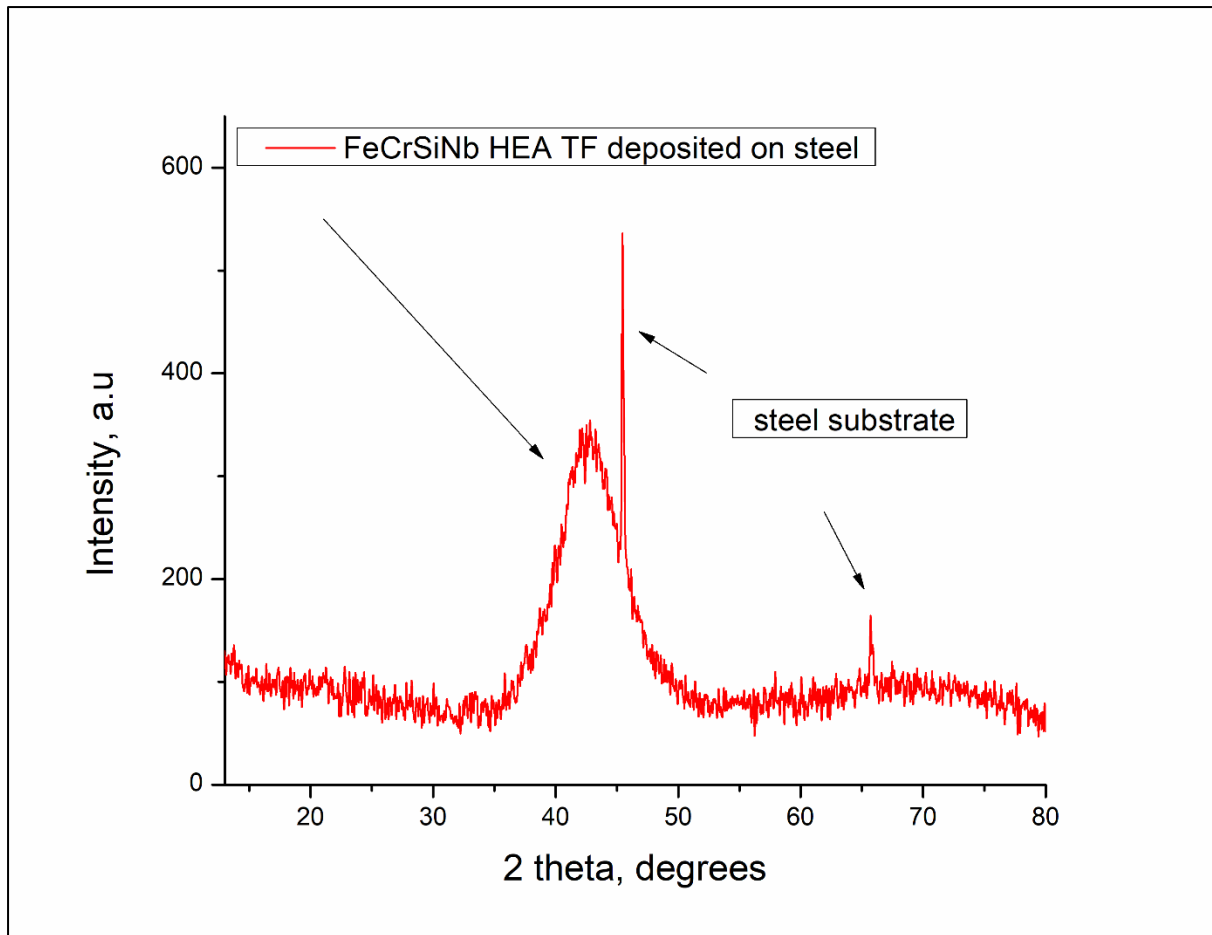


Figure 7-8: XRD pattern of FeCrSiNb amorphous HEA thin film alloy deposited on the steel.

7.3.4 Corrosion test of FeCrSiNb in crude oil

The potentiodynamic polarization curves shown in Fig 7.9 are for the FeCrSiNb equiatomic HEA against that of SS304. Table 7.2 presents the corrosion potential and corrosion current density as well. The results show that FeCrSiNb amorphous HEA TF has a higher corrosion potential of 0.24 than 0.12 V for 304 SS. With a bit smaller corrosion current density of FeCrSiNb alloy 5.41×10^{-12} A/cm² than 9.91×10^{-12} for 304 SS. The results prove that the FeCrSiNb HEA TF deposited on steel has high corrosion resistance and is better than SS304 in crude oil at normal temperature and pressure.

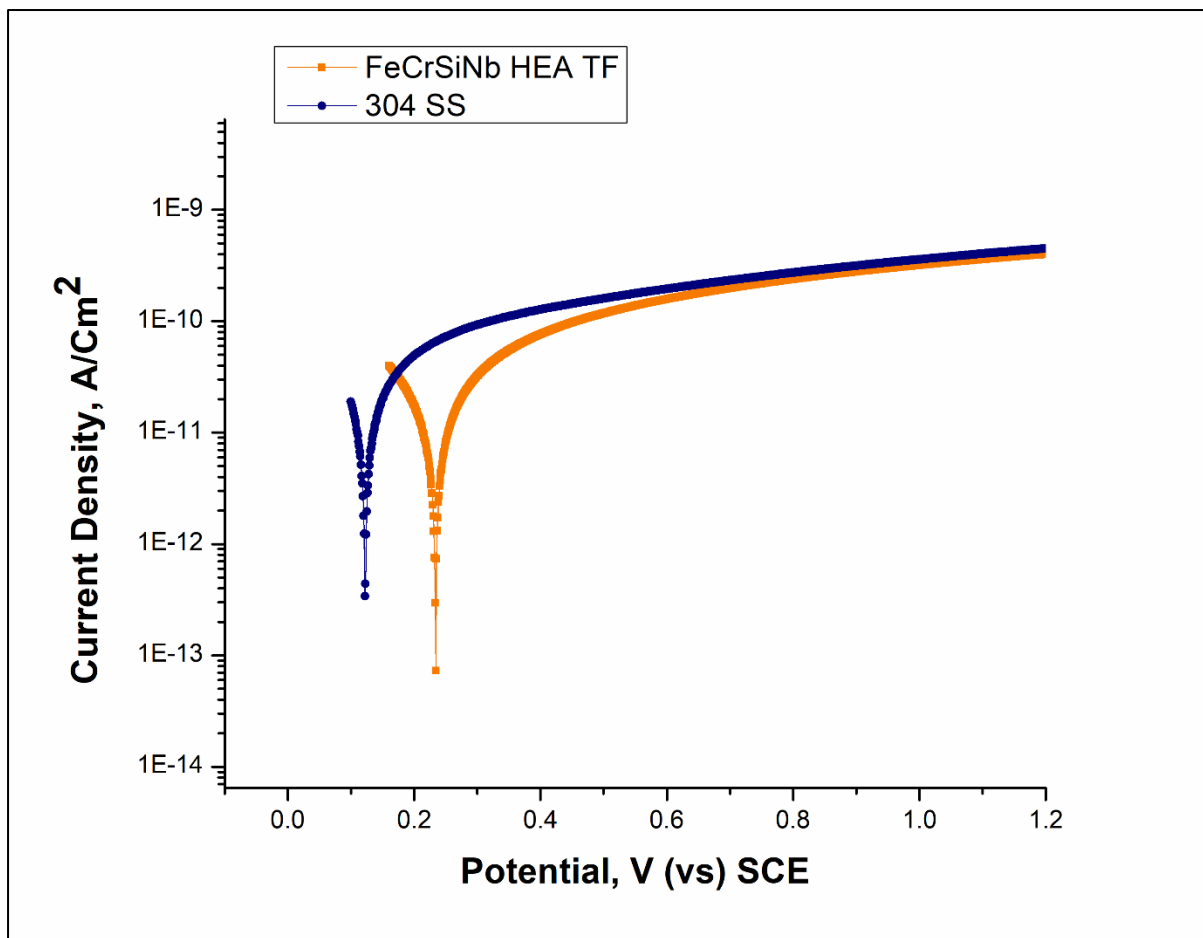


Figure 7-9: polarization curves of FeCrSiNb HEA thin film deposited on steel & 304 SS in crude oil.

Table 7-2: corrosion parameters of FeCrSiNb HE TF alloy deposited on steel and 304 SS in crude oil

Sample	i_{corr} , A/Cm ²	E_{corr} , V
FeCrSiNb	$5.41 \cdot 10^{-12}$	0.240
SS304	$9.91 \cdot 10^{-12}$	0.120

These samples were produced on mild steel, particularly aiming to be provided with a real application in the oil field. Although, generally, there is a lack of studying high entropy alloys

deposited on steel samples, only very few alloys have been reported, such as CrMnFeCoNi high entropy alloy coating prepared on Q235 substrate by mechanical alloying technique [63], FeCoCrAlNiTi_x high entropy alloy coatings deposited on 304 stainless steel via laser surface alloying method [181], and AlTiCrNiTa high entropy alloy coating synthesised on X80 pipeline steel sample [182]. However, all these alloys had a crystalline structure, not an amorphous structure.

The high corrosion resistance of both FeCrMnNiC and FeCrSiNb high entropy thin film alloys deposited on steel substrates could refer to the high entropy effect in the form of a thin film. Also, the higher corrosion resistance of the HEA thin films could be due to the cocktail effect with the presence of elements with high corrosion resistance, for example, Chromium, Nickel, Carbon, Silicon and Niobium in their equiatomic ratios. These elements can create a protective passivation layer that can prevent further corrosion from developing on the alloy surface. Furthermore, the corrosion performance of the prepared alloys was enhanced due to the absence of grain boundaries with no element separation or segregation due to their amorphous structure. In contrast, corrosion usually occurs preferably at inhomogeneous of the grain, grain boundaries [111, 179]. The higher corrosion potential (E_{corr}) of amorphous equiatomic FeCrMnNiC and FeCrSiNb HEA thin film can be attributed to the fact that high entropy alloys undergo self-passivation at the beginning of the test at open circuit potential (OCP), and this what makes high entropy alloys unique and better than stainless steel which has less corrosion potential (E_{corr}) values [51, 126].

7.4 Summary

Equiatomic FeCrMnNiC and FeCrSiNb high entropy amorphous thin film alloys were successfully prepared by an ion beam sputter deposition. SEM and EDX mapping confirmed uniform structure with no element segregation. In addition, the amorphous structure of both alloys was successfully achieved by depositing layer by layer at low temperatures and confirmed by XRD. The FeCrMnNiC and FeCrSiNb high entropy amorphous thin films exhibited high resistance to corrosion as they showed more positive E_{corr} and less i_{corr} than 304 ss in crude oil at room temperature under atmospheric pressure. This chapter aimed to simulate the oil field by depositing FeCrMnNiC & FeCrSiNb amorphous high entropy thin film alloys on the real application, which is steel and performing the corrosion tests in crude oil.

8 Chapter8: general conclusion

8.1 Conclusion

In this work, several high entropy or complex, concentrated bulk alloys around 36 alloys (see appendix I) were fabricated via arc melting furnace and characterised by SEM and EDX (and some with XRD) and found to have two phases and three phases. FeCrMnNiC_x alloys with (x = 2, 5, 10 and 20 at. %) were characterised by SEM, EDX and XRD. Where x = 2 at. %, the alloy showed a single-phase structure as it was aimed and motivated. In contrast, the other alloys displayed two phases. The alloys and compositions were chosen as they have not been reported in previous studies. Also, the elements in the composition were chosen to have high corrosion resistance alloys. Moreover, all FeCrMnNiC alloys were tested in NaCl to conduct a corrosion test. The results showed slight increases in corrosion resistance as the number of components increased.

Two high entropy thin films (HEA TFs) (FeCrMnNiC & FeCrSiNb) were synthesised using an Ion beam sputter deposition system. These two alloys with equiatomic compositions and amorphous structures were chosen to aim to have high corrosion resistance and because they are new HEAs TF.

FeCrMnNiC and FeCrSiNb equiatomic high entropy amorphous thin film alloys were successfully deposited on silicon substrate for lab and different application use and on mild steel substrates to simulate real applications in the oil field by ion beam sputter deposition.

The HEAs were subjected to characterisation tests using EDX, SEM, XRD and TEM to study the microstructure. FeCrMnNiC and FeCrSiNb HEA TF alloys exhibited single phase and amorphous structure.

FeCrMnNiC and FeCrSiNb HEAs TF deposited on silicon were subjected to electrochemical tests to conduct corrosion tests in 0.6 M NaCl solution, as shown in fig. 8.1, and in 0.6 M H₂SO₄ solution, as shown in fig. 8.2, and in crude oil, as shown in figure 8.3 below.

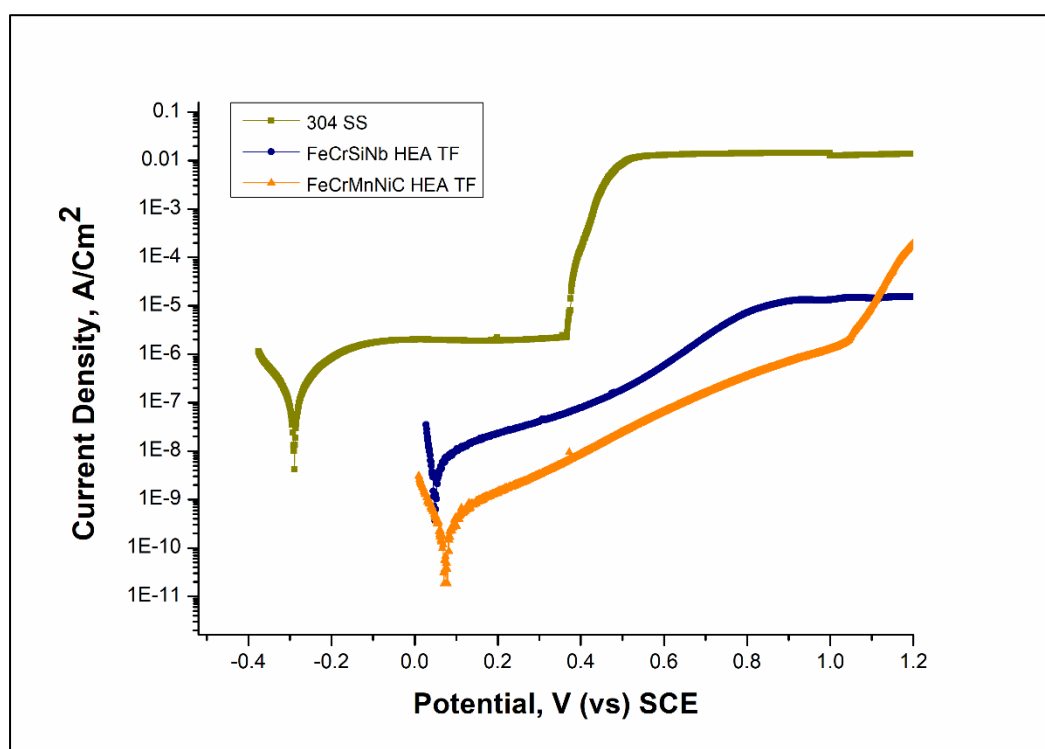


Figure 8-1: polarization curves of FeCrMnNiC and FeCrSiNb HE TF alloys deposited on silicon and 304 SS in 0.6 M NaCl solution.

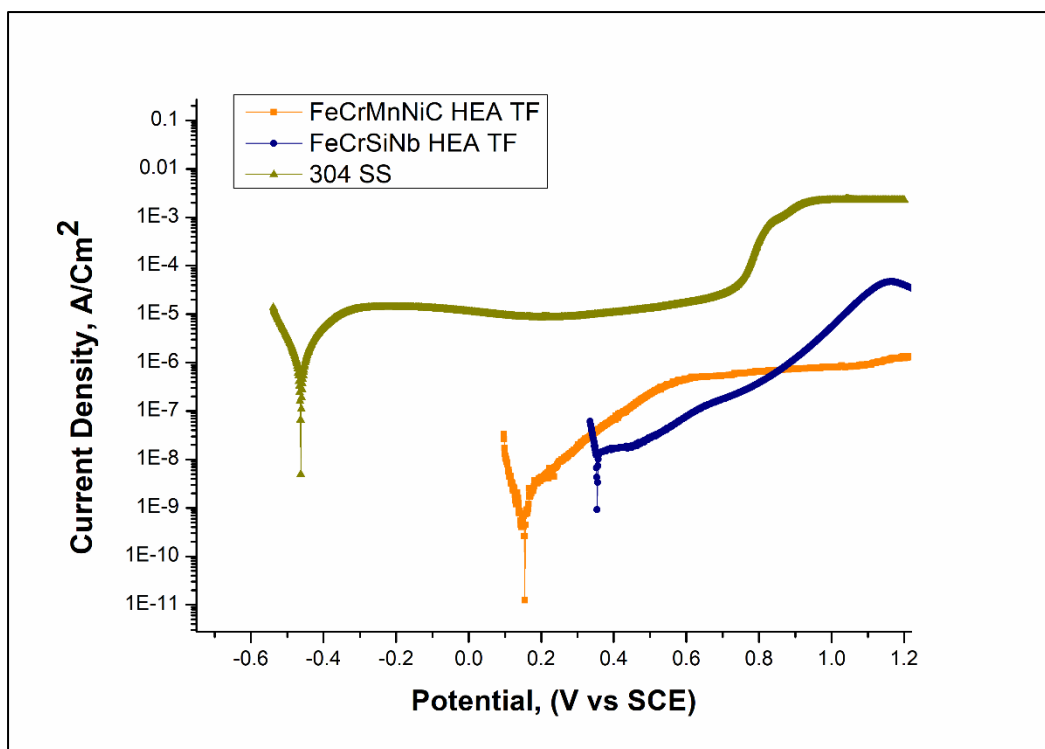


Figure 8-2: polarization curves of FeCrMnNiC and FeCrSiNb HE TF alloys deposited on silicon and 304 SS in 0.6 M H₂SO₄ solution.

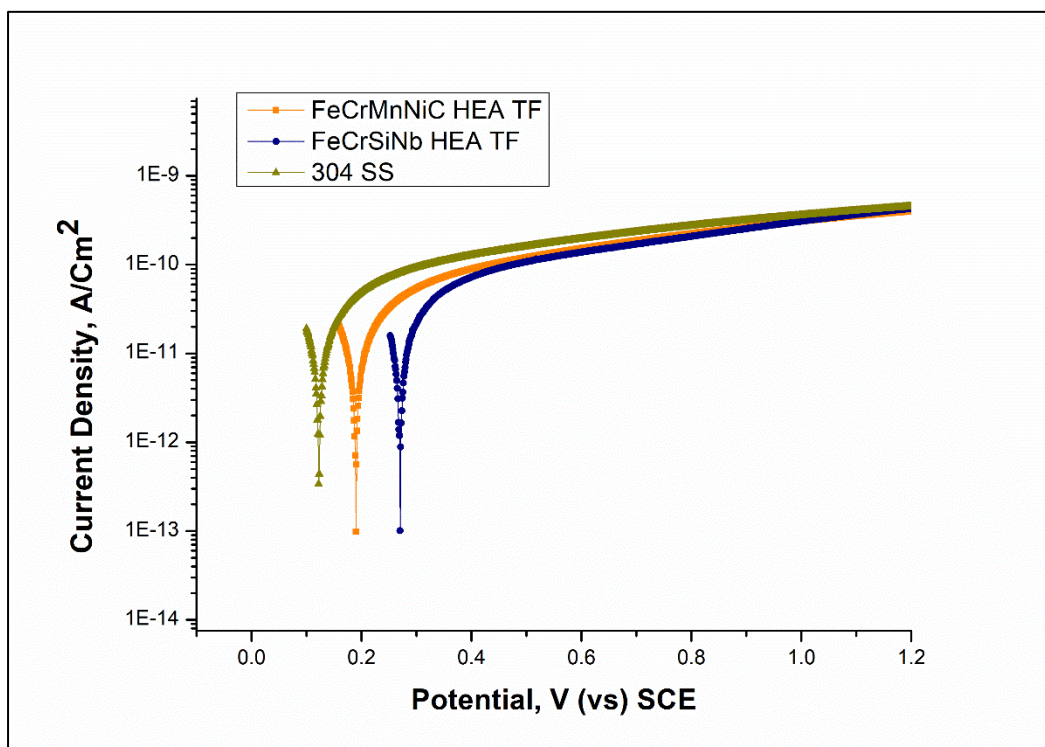


Figure 8-3: polarization curves of FeCrMnNiC and FeCrSiNb HE TF alloys deposited on silicon and 304 SS in crude oil.

Both; FeCrMnNiC and FeCrSiNb HEAs TF deposited on silicon substrates showed outstanding corrosion resistance and better than that in 304 SS in all solutions, NaCl and H₂SO₄ solutions, and in crude oil. Furthermore, the obtained corrosion parameters (corrosion potential & corrosion current density) demonstrate that FeCrMnNiC and FeCrSiNb HEA amorphous thin films have high corrosion resistance with excellent performance in all mentioned solutions.

Also, FeCrMnNiC and FeCrSiNb HEAs TF deposited on mild steel substrates tests in crude oil to mimic real oil fields, as provided in fig. 8.4 below. FeCrMnNiC and FeCrSiNb equiatomic HEA thin films showed higher corrosion potential with less corrosion current density than that in 304 SS. This suggests better corrosion resistance of the FeCrMnNiC and FeCrSiNb HEA thin films deposited on steel than in 304 SS in crude oil at room temperature & surrounding pressure.

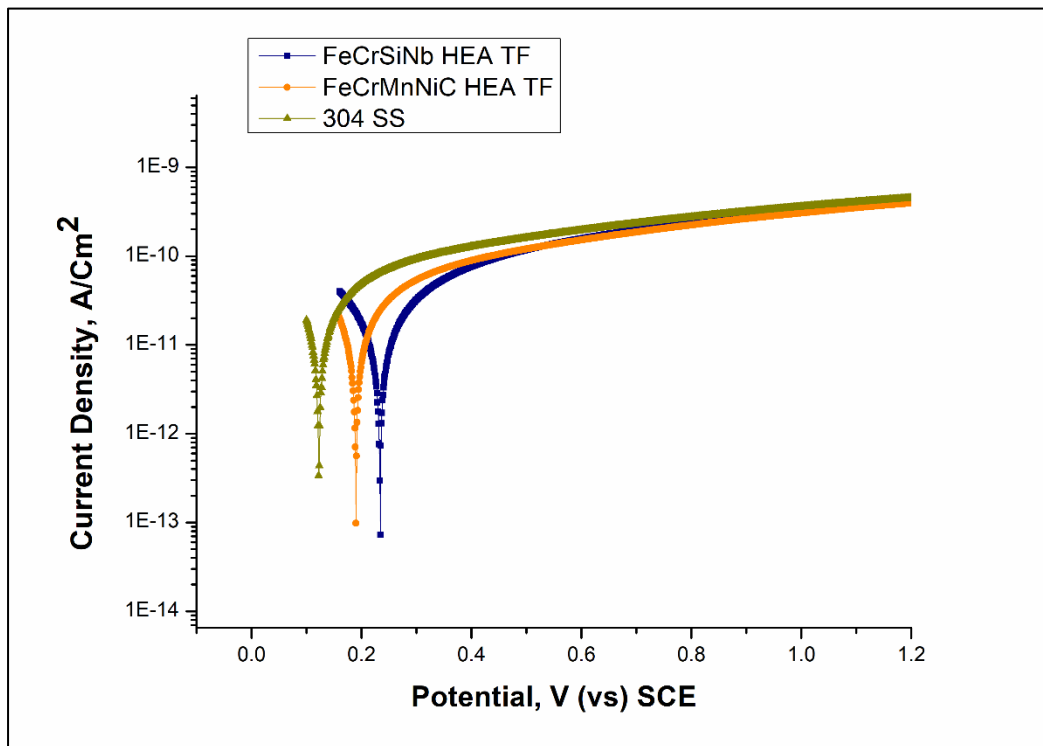


Figure 8-4: polarization curves of FeCrMnNiC and FeCrSiNb HE TF alloys deposited on mild steel and 304 SS in crude oil.

The high corrosion resistance of both FeCrMnNiC and FeCrSiNb amorphous equiatomic thin film alloys deposited on silicon and mild steel can be attributed to several reasons, such as; the equiatomic ratio of having alloys contain four or five elements which is one of the main effects of high entropy alloys [59, 162]. Conventional materials rely on the oxide layer, which forms from one of the main elements only; for instance, 304 SS is well-known as a good corrosion-resistant material used in different areas. However, 304 SS mainly relies on the chromium content in the composition, which reacts with oxygen to form a passive protective layer; however, over time and in different environments, the passive layer starts to break down (where pitting occurs), failing the application. This could happen especially in an environment with high amounts of salty water and chlorine [51, 126]. However, the high entropy thin film alloys rely on the resistance of the material itself as well as on the elements chosen. As a result, corrosion is more likely to occur in large deviations and grain boundaries. Hence, a more uniform homogenous structure with the absence of grain boundaries in an amorphous structure with no elemental segregation or separation could improve the corrosion resistance of the alloy. On the other hand, the potential difference in multi-phase material will form an anode and cathode, resulting in pitting on the material surface [69].

In addition, the presence of the chosen elements with good corrosion resistance, for instance, Cr, Ni, C, Si and Nb (cocktail effect), can increase the alloy's passive layer and inhibit the appearance of holes or pitting [146, 159, 175].

Also, equiatomic FeCrMnNiC and FeCrSiNb amorphous thin film alloys deposited on high silicon hardness and reduced Young modulus values were tested by nanoindentation test. The results show that the equiatomic FeCrMnNiC and FeCrSiNb amorphous thin film alloys have excellent mechanical properties. This confirms that equiatomic FeCrMnNiC and FeCrSiNb

amorphous thin film alloys are very good materials and can be used in oil fields and other applications.

Novelty statement

A combination of widely available elements, like Fe, Mn, Cr, Si and C, with a more exotic element, Nb, allowed producing novel High Entropy Amorphous films with exceptionally high corrosion resistance for challenging environments. In addition, the high hardness of the produced films allows for the alloy designation as highly erosion-resistive materials proposed for coatings in oil extraction and its processing.

Future work

Some tests and analyses have been left due to time and lab availability, as they are time-consuming and need to be conducted under several techniques and in different labs.

In future, it aims to study some properties of the FeCrMnNiC and FeCrSiNb amorphous equiatomic thin film alloys such as nano-scratch to study the resistance of the synthesised amorphous HEAs TF to the wear.

Also, it would be a great achievement to investigate the mechanical properties of the multi-phase FeCrMnNiC_x bulk alloys with ($x = 5, 10$ and 20 at. %).

Covid-19 restrictions

It was aimed to study some properties of the synthesised alloys, as mentioned in future work. However, the university was closed for around seven months due to the national lockdowns

imposed by the UK government. Then the return to the lab was restricted to a couple of hours per week to be divided fairly among all the students. Also, there was no access to the other labs in other departments at the university. All these affected getting the results and led to a delay in accomplishing the aimed research. In addition, I tested positive twice for the covid-19 virus two different times. Working from home also was not convenient for establishing practical and lab experimentation. However, time was invested in publishing research papers and attending academic conferences.

9 References

1. Revie, R.W., *Corrosion and corrosion control: an introduction to corrosion science and engineering*. 2008: John Wiley & Sons.
2. Groysman, A., *Corrosion in systems for storage and transportation of petroleum products and biofuels: identification, monitoring and solutions*. 2014: Springer Science & Business Media.
3. Makhlouf, A.S.H., V. Herrera, and E. Muñoz, *Corrosion and protection of the metallic structures in the petroleum industry due to corrosion and the techniques for protection*, in *Handbook of Materials Failure Analysis*. 2018, Elsevier. p. 107-122.
4. Popoola, L.T., et al., *Corrosion problems during oil and gas production and its mitigation*. International Journal of Industrial Chemistry, 2013. **4**(1): p. 35.
5. Lusk, D., et al., *Armoured against corrosion*. Hydrocarbon engineering, 2008. **13**(11).
6. Roberge, P.R., *Handbook of corrosion engineering*. 2019: McGraw-Hill Education.
7. Speight, J.G., *Oil and gas corrosion prevention: from surface facilities to refineries*. 2014: Gulf Professional Publishing.
8. Brondel, D., et al., *Corrosion in the oil industry*. Oilfield review, 1994. **6**(2): p. 4-18.
9. Eiselstein, L. and R. Huet, *Corrosion Failure Analysis with Case Histories*. Uhlig's Corrosion Handbook, 2011. **51**: p. 1.
10. Corbin, D. and E. Willson. *New technology for real-time corrosion detection*. in *Tri-service corrosion conference, USA*. 2007.

11. Dean, F. and S. Powell. *Hydrogen flux and high temperature acid corrosion*. in *CORROSION 2006*. 2006. NACE International.
12. Fontana, M.G., *Corrosion engineering*. 2005: Tata McGraw-Hill Education.
13. Frankel, G. and N. Sridhar, *Understanding localized corrosion*. *Materials today*, 2008. **11**(10): p. 38-44.
14. Askari, M., M. Aliofkhazraei, and S. Afroukhteh, *A comprehensive review on internal corrosion and cracking of oil and gas pipelines*. *Journal of Natural Gas Science and Engineering*, 2019. **71**: p. 102971.
15. Ebrahimi, N., M.H. Moayed, and A. Davoodi, *Critical pitting temperature dependence of 2205 duplex stainless steel on dichromate ion concentration in chloride medium*. *Corrosion Science*, 2011. **53**(4): p. 1278-1287.
16. Popov, B.N., *Corrosion engineering: principles and solved problems*. 2015: Elsevier.
17. Singh, R., *Corrosion control for offshore structures: cathodic protection and high-efficiency Coating*. 2014: Gulf Professional Publishing.
18. Shi, L., C. Wang, and C. Zou, *Corrosion failure analysis of L485 natural gas pipeline in CO₂ environment*. *Engineering Failure Analysis*, 2014. **36**: p. 372-378.
19. Bardal, E. and B. Derby, *Different forms of corrosion classified on the basis of appearance*. *Corrosion and protection*, 2004: p. 89-191.
20. Kermani, M. and A. Morshed, *Carbon dioxide corrosion in oil and gas production—a compendium*. *Corrosion*, 2003. **59**(8): p. 659-683.

21. Abdallah, D., et al., *Casing corrosion measurement to extend asset life*. Oilfield Review, 2013. **25**(3): p. 18-31.
22. Dunlop, A., H. Hassell, and P. Rhodes, *Fundamental considerations in sweet gas well corrosion*, in *Corrosion* 83. 1983. p. 461-4624.
23. Perez, T.E., *Corrosion in the oil and gas industry: an increasing challenge for materials*. Jom, 2013. **65**(8): p. 1033-1042.
24. Smith, L., *Control of corrosion in oil and gas production tubing*. British Corrosion Journal, 1999. **34**(4): p. 247-253.
25. Bahadori, A., *Corrosion and materials selection: a guide for the chemical and petroleum industries*. 2014: John Wiley & Sons.
26. Al-Janabi, Y.T., *An overview of corrosion in oil and gas industry: upstream, midstream, and downstream sectors*. Corrosion Inhibitors in the Oil and Gas Industry, 2020: p. 1-39.
27. Corlett, N., L. Eiselstein, and N. Budiansky, *Crevice corrosion*. 2010.
28. Kelly, R.G. and J.S. Lee, *Localized Corrosion: Crevice Corrosion*, in *Encyclopedia of Interfacial Chemistry*, K. Wandelt, Editor. 2018, Elsevier: Oxford. p. 291-301.
29. Papavinasam, S., *Corrosion control in the oil and gas industry*. 2013: Elsevier.
30. Lipp, W. and S. Shafer, *The future of corrosion resistant steels and alloys in the oil and gas industry*. Stainless steel world, 2013. **25**: p. 29-32.
31. Craig, B.D., *Selection guidelines for corrosion resistant alloys in the oil and gas industry*. Chemical engineering world, 1998. **33**: p. 57-60.

32. Craig, B.D. and L. Smith, *Corrosion Resistant Alloys (CRAs) in the oil and gas industry*. Nickel Institute Technical Series, 2011. **1**: p. 0073.
33. Bradford, S.A., *CORROSION CONTROL*. Second Edition
ed. 2001, National Library of Canada Cataloguing in Publication Data: CASTI.
34. Eremin, E., et al., *Anti-corrosion wear-resistant coatings on parts of oil field equipment*. Procedia Engineering, 2016. **152**: p. 594-600.
35. Fessler, R.R., *Pipeline corrosion*. Report, US Department of Transportation Pipeline and Hazardous Materials Safety Administration, Baker, Evanston, IL, 2008.
36. Zavareh, M.A., et al., *Plasma thermal spray of ceramic oxide coating on carbon steel with enhanced wear and corrosion resistance for oil and gas applications*. Ceramics International, 2014. **40**(9): p. 14267-14277.
37. Rossnagel, S., *Thin film deposition with physical vapor deposition and related technologies*. Journal of Vacuum Science & Technology A: Vacuum, Surfaces, and Films, 2003. **21**(5): p. S74-S87.
38. Tunes, M.A., V.M. Vishnyakov, and S.E. Donnelly, *Synthesis and characterisation of high-entropy alloy thin films as candidates for coating nuclear fuel cladding alloys*. Thin Solid Films, 2018. **649**: p. 115-120.
39. Wittmer, M. and H. Melchior, *Applications of TiN thin films in silicon device technology*. MRS Online Proceedings Library Archive, 1981. **10**.
40. Ojovan, M.I. and W.B.E. Lee, *Connectivity and glass transition in disordered oxide systems*. Journal of Non-Crystalline Solids, 2010. **356**(44-49): p. 2534-2540.

41. Wang, W., *High-entropy metallic glasses*. Jom, 2014. **66**(10): p. 2067-2077.
42. Telford, M., *The case for bulk metallic glass*. Materials today, 2004. **7**(3): p. 36-43.
43. Masumoto, T. and K. Hashimoto, *Corrosion properties of amorphous metals*. Le Journal de Physique Colloques, 1980. **41**(C8): p. C8-894-C8-900.
44. Gao, X., et al., *High mixing entropy bulk metallic glasses*. Journal of Non-Crystalline Solids, 2011. **357**(21): p. 3557-3560.
45. Yeh, J.W., et al., *Nanostructured high-entropy alloys with multiple principal elements: novel alloy design concepts and outcomes*. Advanced Engineering Materials, 2004. **6**(5): p. 299-303.
46. Mary, S.J., N. Rajan, and R. Epshiba, *High entropy alloys properties and its applications—An over view*. European Chemical Bulletin, 2015. **4**(4-6): p. 279-284.
47. Ye, Y., et al., *High-entropy alloy: challenges and prospects*. Materials Today, 2016. **19**(6): p. 349-362.
48. Miracle, D.B. and O.N. Senkov, *A critical review of high entropy alloys and related concepts*. Acta Materialia, 2017. **122**: p. 448-511.
49. Gorsse, S., J.-P. Couzinié, and D.B. Miracle, *From high-entropy alloys to complex concentrated alloys*. Comptes Rendus Physique, 2018. **19**(8): p. 721-736.
50. Gorsse, S., D.B. Miracle, and O.N. Senkov, *Mapping the world of complex concentrated alloys*. Acta Materialia, 2017. **135**: p. 177-187.
51. Gorsse, S., et al., *Database on the mechanical properties of high entropy alloys and complex concentrated alloys*. Data in brief, 2018. **21**: p. 2664-2678.

52. Wu, Z., et al., *Temperature dependence of the mechanical properties of equiatomic solid solution alloys with face-centered cubic crystal structures*. Acta Materialia, 2014. **81**: p. 428-441.
53. Zuo, T., et al., *Effects of Al and Si addition on the structure and properties of CoFeNi equal atomic ratio alloy*. Journal of Magnetism and Magnetic Materials, 2014. **371**: p. 60-68.
54. Tseng, K., et al., *A light-weight high-entropy alloy Al 20 Be 20 Fe 10 Si 15 Ti 35*. Science China Technological Sciences, 2018. **61**(2): p. 184-188.
55. An, Z., et al., *Solid-solution CrCoCuFeNi high-entropy alloy thin films synthesized by sputter deposition*. Materials Research Letters, 2015. **3**(4): p. 203-209.
56. Braic, M., et al., *Solid solution or amorphous phase formation in TiZr-based ternary to quinary multi-principal-element films*. Progress in Natural Science: Materials International, 2014. **24**(4): p. 305-312.
57. Shen, W.-J., M.-H. Tsai, and J.-W. Yeh, *Machining performance of sputter-deposited (Al_{0.34}Cr_{0.22}Nb_{0.11}Si_{0.11}Ti_{0.22})₅₀N₅₀ high-entropy nitride coatings*. Coatings, 2015. **5**(3): p. 312-325.
58. Li, W., P. Liu, and P.K. Liaw, *Microstructures and properties of high-entropy alloy films and coatings: a review*. Materials Research Letters, 2018. **6**(4): p. 199-229.
59. Shi, Y., B. Yang, and P. Liaw, *Corrosion-resistant high-entropy alloys: A review*. Metals, 2017. **7**(2): p. 43.

60. Hsu, Y.-J., W.-C. Chiang, and J.-K. Wu, *Corrosion behavior of FeCoNiCrCux high-entropy alloys in 3.5% sodium chloride solution*. Materials Chemistry and Physics, 2005. **92**(1): p. 112-117.
61. Zhou, Q., et al., *Corrosion behavior of Hf0. 5Nb0. 5Ta0. 5Ti1. 5Zr refractory high-entropy in aqueous chloride solutions*. Electrochemistry Communications, 2019. **98**: p. 63-68.
62. Zeng, Q. and Y. Xu, *A comparative study on the tribocorrosion behaviors of AlFeCrNiMo high entropy alloy coatings and 304 stainless steel*. Materials Today Communications, 2020: p. 101261.
63. Tian, Y., et al., *Microstructure and corrosion property of CrMnFeCoNi high entropy alloy coating on Q235 substrate via mechanical alloying method*. Surfaces and Interfaces, 2019. **15**: p. 135-140.
64. Wang, H.-d., et al., *Microstructure and corrosion behaviour of AlCoFeNiTiZr high-entropy alloy films*. Surface Engineering, 2020. **36**(1): p. 78-85.
65. Qiu, X.-w., et al., *Structure and properties of AlCrFeNiCuTi six principal elements equimolar alloy*. Journal of Alloys and Compounds, 2016. **658**: p. 1-5.
66. Ren, B., et al., *Corrosion behavior of CuCrFeNiMn high entropy alloy system in 1 M sulfuric acid solution*. Materials and Corrosion, 2012. **63**(9): p. 828-834.
67. Cheng, J., et al., *Formation and mechanical properties of CoNiCuFeCr high-entropy alloys coatings prepared by plasma transferred arc cladding process*. Plasma Chemistry and Plasma Processing, 2013. **33**(5): p. 979-992.

68. Qiu, X., Y. Zhang, and C. Liu, *Effect of Ti content on structure and properties of Al₂CrFeNiCoCuTi_x high-entropy alloy coatings*. Journal of alloys and compounds, 2014. **585**: p. 282-286.
69. Qiu, X.-w., et al., *Corrosion performance of Al₂CrFeCoxCuNiTi high-entropy alloy coatings in acid liquids*. Journal of Alloys and Compounds, 2017. **708**: p. 353-357.
70. Xu, Y., et al., *Formation and properties of Fe₂₅Co₂₅Ni₂₅ (P, C, B, Si) 25 high-entropy bulk metallic glasses*. Journal of Non-Crystalline Solids, 2018. **487**: p. 60-64.
71. Ding, H. and K. Yao, *High entropy Ti₂₀Zr₂₀Cu₂₀Ni₂₀Be₂₀ bulk metallic glass*. Journal of Non-Crystalline Solids, 2013. **364**: p. 9-12.
72. Chen, Y., et al., *Microstructure and electrochemical properties of high entropy alloys—a comparison with type-304 stainless steel*. Corrosion science, 2005. **47**(9): p. 2257-2279.
73. Tabor, D., *The hardness of metals*. 2000: Oxford university press.
74. Doerner, M. and W. Nix, *A method for interpreting the data from depth-sensing indentation*. Journal of Materials research, 1986. **1**(4): p. 601-609.
75. Jönsson, B. and S. Hogmark, *Hardness measurements of thin films*. Thin solid films, 1984. **114**(3): p. 257-269.
76. Chudoba, T., *Measurement of hardness and Young's modulus by nanoindentation*, in *Nanostructured coatings*. 2006, Springer. p. 216-260.

77. Huang, T., et al., *Effect of carbon addition on the microstructure and mechanical properties of CoCrFeNi high entropy alloy*. Science China Technological Sciences, 2018. **61**(1): p. 117-123.
78. Huo, W., et al., *Ultrahigh hardness and high electrical resistivity in nano-twinned, nanocrystalline high-entropy alloy films*. Applied Surface Science, 2018. **439**: p. 222-225.
79. Liu, L., et al., *Dense and smooth amorphous films of multicomponent FeCoNiCuVZrAl high-entropy alloy deposited by direct current magnetron sputtering*. Materials & Design, 2013. **46**: p. 675-679.
80. MTI. *Compact Vacuum Arc Melting System with 7 Cavities - EQ-SP-MSM207*. 1994; Available from: <https://www.mtixtl.com/EQ-SP-MSM207.aspx>.
81. Asensio Dominguez, L., *Combinatorial high throughput synthesis of high entropy alloys*. 2016, University of Sheffield.
82. Zhang, Y., et al., *Microstructures and properties of high-entropy alloys*. Progress in Materials Science, 2014. **61**: p. 1-93.
83. Goldstein, J.I., et al., *Scanning electron microscopy and X-ray microanalysis*. 2017: Springer.
84. Stokes, D., *Principles and practice of variable pressure/environmental scanning electron microscopy (VP-ESEM)*. 2008: John Wiley & Sons.
85. Zhou, W., et al., *Fundamentals of scanning electron microscopy (SEM)*, in *Scanning microscopy for nanotechnology*. 2006, Springer. p. 1-40.

86. Cheney, B., *Introduction to scanning electron microscopy*. Materials Engineering department San Jose State University, 2007.
87. Williams, D.B. and C. Barry, *Carter. Transmission electron microscopy: a textbook for materials science*. 2009, New York: Springer.
88. Carter, C.B. and D.B. Williams, *Transmission electron microscopy: Diffraction, imaging, and spectrometry*. 2016: Springer.
89. Fultz, B. and J.M. Howe, *Transmission electron microscopy and diffractometry of materials*. 2012: Springer Science & Business Media.
90. CARTER, B.A., et al., *Transmission Electron Microscopy: A Textbook for Materials Science. Diffraction. II. Vol. 2*. 1996: Springer Science & Business Media.
91. Marturi, N., *Vision and visual servoing for nanomanipulation and nanocharacterization in scanning electron microscope*. 2013, Université de Franche-Comté.
92. Giannuzzi, L.A., *Introduction to focused ion beams: instrumentation, theory, techniques and practice*. 2004: Springer Science & Business Media.
93. Nee, A.Y.C., *Handbook of manufacturing engineering and technology*. 2015: Springer.
94. Kelly, P.J. and R.D. Arnell, *Magnetron sputtering: a review of recent developments and applications*. Vacuum, 2000. **56**(3): p. 159-172.

95. Teixeira, V., et al., *11 - High barrier plastics using nanoscale inorganic films*, in *Multifunctional and Nanoreinforced Polymers for Food Packaging*, J.-M. Lagarón, Editor. 2011, Woodhead Publishing. p. 285-315.
96. McNeil, J.R., J.J. McNally, and P.D. Reader, *11 - Ion Beam Deposition*, in *Handbook of Thin Film Deposition Processes and Techniques (Second Edition)*, K. Seshan, Editor. 2001, William Andrew Publishing: Norwich, NY. p. 463-499.
97. Mattox, D.M., *Handbook of physical vapor deposition (PVD) processing*. 2010: William Andrew.
98. Chinn, R.E., *Ceramography: preparation and analysis of ceramic microstructures*. 2002: ASM International.
99. Elssner, G., et al., *Ceramics and ceramic composites: materialographic preparation*. 1999: Elsevier.
100. Renault, P.-O., *X-Ray Diffraction (XRD)*. 2010.
101. Epp, J., *X-ray diffraction (XRD) techniques for materials characterization*, in *Materials characterization using Nondestructive Evaluation (NDE) methods*. 2016, Elsevier. p. 81-124.
102. Stansbury, E.E. and R.A. Buchanan, *Fundamentals of electrochemical corrosion*. 2000: ASM international.
103. Mansfeld, F., *Evaluation of electrochemical techniques for monitoring of atmospheric corrosion phenomena*, in *Electrochemical Corrosion Testing*. 1981, ASTM International.

104. McIntyre, P. and A. Mercer, *Corrosion testing and determination of corrosion rates*. 2010.
105. Cottis, R., *Electrochemical methods*. 2010.
106. Kelly, R.G., et al., *Electrochemical techniques in corrosion science and engineering*. 2002: CRC Press.
107. Strehblow, H.H., *Passivity of metals*. Advances in electrochemical science and engineering, 2003. **8**: p. 271.
108. Swain, S. *CORROSION BASICS*. 1996, 1997; Available from: <https://docplayer.net/28132024-Corrosion-basics-from-swain-1996-and-schultz-1997.html>.
109. Van Orden, A.C. *Applications and problem solving using the polarization technique*. in *CORROSION* 98. 1998. NACE International.
110. Instruments, G., *Getting Started with Electrochemical Corrosion Measurement*. Gamry Instruments: Warminster, PA, USA, 2011.
111. Muftah, W., N. Patmore, and V. Vishnyakov, *Demanding applications in harsh environment—FeCrMnNiC amorphous equiatomic alloy thin film*. Materials Science and Technology, 2020. **36**(12): p. 1301-1307.
112. Guan, L., et al., *Effects of cyclic stress on the metastable pitting characteristic for 304 stainless steel under potentiostatic polarization*. Corrosion Science, 2015. **93**: p. 80-89.

113. Cao, F., *Development of CMOS integrated electrochemical microsensors*. 2008, Carnegie Mellon University.
114. Qi, Z., *Electrochemical methods for catalyst activity evaluation*, in *PEM Fuel cell electrocatalysts and catalyst layers*. 2008, Springer. p. 547-607.
115. Sequeira, C.A., *High temperature corrosion: fundamentals and engineering*. 2019: John Wiley & Sons.
116. EC08, A.A.N., *Basic overview of the working principle of a potentiostat/galvanostat (PGSTAT)–Electrochemical cell setup*. Metrohm Autolab. BV, 2011: p. 1-3.
117. Heineman, W.R., *Laboratory techniques in electroanalytical chemistry*. 2018: CRC Press.
118. Mizusaki, J., et al., *Electrode reaction at Pt, O₂ (g)/stabilized zirconia interfaces. Part II: Electrochemical measurements and analysis*. Solid State Ionics, 1987. **22**(4): p. 323-330.
119. NOVA. *User manual* 2013; Available from: https://www.metrohm-autolab.com/download/NovaSoftware/User_manual_1.10.pdf.
120. Zinkle, S. and J. Huang, *Mechanical properties of carbon-implanted niobium*. MRS Online Proceedings Library (OPL), 1990. **188**.
121. Oliver, W.C. and G.M. Pharr, *Nanoindentation in materials research: Past, present, and future*. Mrs Bulletin, 2010. **35**(11): p. 897-907.

122. Haghshenas, M., et al., *Indentation-based rate-dependent plastic deformation of polycrystalline pure magnesium*. Materials Science and Engineering: A, 2018. **716**: p. 63-71.
123. Baker, S.P. and J. Liu, *Nanoindentation Techniques*, in *Reference Module in Materials Science and Materials Engineering*. 2016, Elsevier.
124. Sasmal, S. and M. Anoop, *Nanoindentation for evaluation of properties of cement hydration products*, in *Nanotechnology in Eco-efficient Construction*. 2019, Elsevier. p. 141-161.
125. Enos, D. and L.J.S.I. Scribner, *The Potentiodynamic Polarisation Scan–Technical Report 33*. 1997.
126. Shi, Y., et al., *Corrosion of Al_xCoCrFeNi high-entropy alloys: Al-content and potential scan-rate dependent pitting behavior*. Corrosion Science, 2017. **119**: p. 33-45.
127. Lee, C., et al., *Effect of the aluminium content of Al_xCrFe1.5MnNi0.5 high-entropy alloys on the corrosion behaviour in aqueous environments*. Corrosion Science, 2008. **50**(7): p. 2053-2060.
128. Chou, Y., J. Yeh, and H. Shih, *The effect of molybdenum on the corrosion behaviour of the high-entropy alloys Co1.5CrFeNi1.5Ti0.5Mox in aqueous environments*. Corrosion Science, 2010. **52**(8): p. 2571-2581.
129. Malinovskis, P., et al., *Synthesis and characterization of multicomponent (CrNbTaTiW) C films for increased hardness and corrosion resistance*. Materials & Design, 2018. **149**: p. 51-62.

130. Kang, S., et al., *Effects of recrystallization annealing temperature on carbide precipitation, microstructure, and mechanical properties in Fe–18Mn–0.6 C–1.5 Al TWIP steel*. Materials Science and Engineering: A, 2010. **527**(3): p. 745-751.
131. Zuhailawati, H., T.C. Geok, and P. Basu, *Microstructure and hardness characterization of mechanically alloyed Fe–C elemental powder mixture*. Materials & Design, 2010. **31**(4): p. 2211-2215.
132. Poletti, M.G., et al., *Development of a new high entropy alloy for wear resistance: FeCoCrNiW0.3 and FeCoCrNiW0.3+5 at.% of C*. Materials & Design, 2017. **115**: p. 247-254.
133. Cheng, H., et al., *Controllable fabrication of a carbide-containing FeCoCrNiMn high-entropy alloy: microstructure and mechanical properties*. Materials Science and Technology, 2017. **33**(17): p. 2032-2039.
134. Shen, S., et al., *Effects of carbon doping on irradiation resistance of Fe₃₈Mn₄₀Ni₁₁Al₄Cr₇ high entropy alloys*. Journal of Nuclear Materials, 2020. **540**: p. 152380.
135. Wu, Z., et al., *Recovery, recrystallization, grain growth and phase stability of a family of FCC-structured multi-component equiatomic solid solution alloys*. Intermetallics, 2014. **46**: p. 131-140.
136. Ma, Y., et al., *The BCC/B2 morphologies in Al_xNiCoFeCr high-entropy alloys*. Metals, 2017. **7**(2): p. 57.
137. Bae, J.W., et al., *Deep drawing behavior of CoCrFeMnNi high-entropy alloys*. Metallurgical and Materials Transactions A, 2017. **48**(9): p. 4111-4120.

138. Wang, W.-R., W.-L. Wang, and J.-W. Yeh, *Phases, microstructure and mechanical properties of Al_xCoCrFeNi high-entropy alloys at elevated temperatures*. Journal of Alloys and Compounds, 2014. **589**: p. 143-152.
139. Schmuecker, S.M., et al., *Synthesis of metastable chromium carbide nanomaterials and their electrocatalytic activity for the hydrogen evolution reaction*. Dalton Transactions, 2017. **46**(39): p. 13524-13530.
140. Tirumalasetty, G., et al., *Structural tale of two novel (Cr, Mn) C carbides in steel*. Acta materialia, 2014. **78**: p. 161-172.
141. Guo, S., et al., *Solid solutioning in equiatomic alloys: limit set by topological instability*. Journal of Alloys and Compounds, 2014. **583**: p. 410-413.
142. Klimova, M., et al., *Effect of carbon on cryogenic tensile behavior of CoCrFeMnNi-type high entropy alloys*. Journal of Alloys and Compounds, 2019. **811**: p. 152000.
143. Qian, C., et al., *Effects of interstitial carbon atoms on texture structure and mechanical properties of FeMnCoCr alloys*. PLoS One, 2020. **15**(12): p. e0242322.
144. Davis, J.R., *ASM Handbook: Nondestructive evaluation and quality control*. Vol. 17. 1989: ASM International.
145. Pletcher, D. and F.C. Walsh, *Industrial electrochemistry*. 2012: Springer Science & Business Media.
146. Henderson, R.S., G.A. Shreve, and M.A. Tenhover, *Enhanced corrosion resistant amorphous metal alloy coatings*. 1989, Google Patents.

147. Nygren, K., et al., *Influence of deposition temperature and amorphous carbon on microstructure and oxidation resistance of magnetron sputtered nanocomposite CrC films*. Applied surface science, 2014. **305**: p. 143-153.
148. Shang, X.-L., et al., *Effect of Mo Addition on Corrosion Behavior of High-Entropy Alloys CoCrFeNiMo_x in Aqueous Environments*. Acta Metallurgica Sinica (English Letters), 2019. **32**(1): p. 41-51.
149. Erdoğan, A. and S. Zeytin, *Influence of Al and Ti elements on the microstructure and properties of CrNiFeCoAlTiTi₂Heas fabricated by ECAS*. 2016.
150. Muftah, W. and V. Vishnyakov, *Microstructure and properties of FeCrMnNiC_x compositionally complex bulk alloys*. Vacuum, 2021: p. 110181.
151. Vishnyakov, V., et al., *Ion sputter-deposition and in-air crystallisation of Cr₂AlC films*. Vacuum, 2014. **100**: p. 61-65.
152. Luttge, R., *Nano-and microfabrication for industrial and biomedical applications*. 2016: William Andrew.
153. Satpathy, R.K. and V. Pamuru, *Solar PV Power: Design, Manufacturing and Applications from Sand to Systems*. 2020: Academic Press.
154. Tilli, M., et al., *Handbook of silicon based MEMS materials and technologies*. 2020: Elsevier.
155. Dolique, V., et al., *Thermal stability of AlCoCrCuFeNi high entropy alloy thin films studied by in-situ XRD analysis*. Surface and Coatings Technology, 2010. **204**(12-13): p. 1989-1992.

156. Sheng, W., et al., *Nano-crystallization of high-entropy amorphous NbTiAlSiW_xNy films prepared by magnetron sputtering*. Entropy, 2016. **18**(6): p. 226.
157. Ye, Q., et al., *Microstructure and corrosion properties of CrMnFeCoNi high entropy alloy coating*. Applied Surface Science, 2017. **396**: p. 1420-1426.
158. Shang, C., et al., *CoCrFeNi (W1– xMox) high-entropy alloy coatings with excellent mechanical properties and corrosion resistance prepared by mechanical alloying and hot pressing sintering*. Materials & Design, 2017. **117**: p. 193-202.
159. Wang, W., et al., *Microstructure and Corrosion behavior of (CoCrFeNi) 95Nb5 high-entropy alloy coating fabricated by plasma spraying*. Materials, 2019. **12**(5): p. 694.
160. Qiu, Y., et al., *Corrosion characteristics of high entropy alloys*. Materials Science and Technology, 2015. **31**(10): p. 1235-1243.
161. Rodriguez, A.A., et al., *Effect of molybdenum on the corrosion behavior of high-entropy alloys CoCrFeNi₂ and CoCrFeNi₂Mo_{0.25} under sodium chloride aqueous conditions*. Advances in Materials Science and Engineering, 2018. **2018**.
162. Jien-Wei, Y., *Recent progress in high entropy alloys*. Ann. Chim. Sci. Mat, 2006. **31**(6): p. 633-648.
163. Gan, Y., et al., *Multi-layer laser solid forming of Zr₆₅Al_{17.5}Ni₁₀Cu_{17.5} amorphous coating: Microstructure and corrosion resistance*. Optics & Laser Technology, 2015. **69**: p. 17-22.
164. Li, R., et al., *Structure and corrosion resistance properties of Ni–Fe–B–Si–Nb amorphous composite coatings fabricated by laser processing*. Journal of alloys and compounds, 2013. **580**: p. 327-331.

165. Han, G., K.P. Marimuthu, and H. Lee, *Evaluation of thin film material properties using a deep nanoindentation and ANN*. Materials & Design, 2022. **221**: p. 111000.
166. Dang, C., et al., *Mechanical properties of nanostructured CoCrFeNiMn high-entropy alloy (HEA) coating*. Frontiers in Materials, 2018. **5**: p. 41.
167. Tunes, M.A. and V.M. Vishnyakov, *Microstructural origins of the high mechanical damage tolerance of NbTaMoW refractory high-entropy alloy thin films*. Materials & Design, 2019. **170**: p. 107692.
168. Chang, Z.-C., et al., *Characteristics of TiVCrAlZr multi-element nitride films prepared by reactive sputtering*. Nuclear Instruments and Methods in Physics Research Section B: Beam Interactions with Materials and Atoms, 2010. **268**(16): p. 2504-2509.
169. Vishnyakov, V., et al., *Amorphous Boron containing silicon carbo-nitrides created by ion sputtering*. Surface and Coatings Technology, 2011. **206**(1): p. 149-154.
170. Ausralia, G.A.o. *COATING THICKNESS AND FACTORS INFLUENCING THICKNESS*. 2020; Available from: <https://gaa.com.au/coating-thickness-and-factors-influencing-thickness/>.
171. Guo, S., et al., *More than entropy in high-entropy alloys: Forming solid solutions or amorphous phase*. Intermetallics, 2013. **41**: p. 96-103.
172. Braeckman, B. and D. Depla, *Structure formation and properties of sputter deposited Nbx-CoCrCuFeNi high entropy alloy thin films*. Journal of Alloys and Compounds, 2015. **646**: p. 810-815.

173. Kao, Y.-F., et al., *Electrochemical passive properties of Al_xCoCrFeNi (x= 0, 0.25, 0.50, 1.00) alloys in sulfuric acids*. Corrosion Science, 2010. **52**(3): p. 1026-1034.
174. Shun, T.-T., C.-H. Hung, and C.-F. Lee, *The effects of secondary elemental Mo or Ti addition in Al_{0.3}CoCrFeNi high-entropy alloy on age hardening at 700 C*. Journal of Alloys and Compounds, 2010. **495**(1): p. 55-58.
175. Nene, S., et al., *Corrosion-resistant high entropy alloy with high strength and ductility*. Scripta Materialia, 2019. **166**: p. 168-172.
176. Shi, Y., et al., *In-situ electrochemical-AFM study of localized corrosion of Al_xCoCrFeNi high-entropy alloys in chloride solution*. Applied Surface Science, 2018. **439**: p. 533-544.
177. Xing, Q., et al., *Mechanical properties and corrosion resistance of NbTiAlSiZrN_x high-entropy films prepared by RF magnetron sputtering*. Entropy, 2019. **21**(4): p. 396.
178. Jiang, H., et al., *Synthesis and characterization of AlCoCrFeNiNb_x high-entropy alloy coatings by laser cladding*. Crystals, 2019. **9**(1): p. 56.
179. Muftah, W., J. Allport, and V. Vishnyakov, *Corrosion performance and mechanical properties of FeCrSiNb amorphous equiatomic HEA thin film*. Surface and Coatings Technology, 2021. **422**: p. 127486.
180. Krishnan, K.M., *Principles of Materials Characterization and Metrology*. 2021: Oxford University Press.

181. Wu, C., et al., *Phase evolution and cavitation erosion-corrosion behavior of FeCoCrAlNiTi_x high entropy alloy coatings on 304 stainless steel by laser surface alloying*. Journal of Alloys and Compounds, 2017. **698**: p. 761-770.
182. Zhao, S., et al., *Microstructure and chloride corrosion property of nanocrystalline AlTiCrNiTa high entropy alloy coating on X80 pipeline steel*. Surface and Coatings Technology, 2019. **375**: p. 215-220.

10 Appendix

Appendix I

Table of all synthesised bulk alloys

The table below shows all melts with different compositions have been prepared by arc melting as they are displayed in different colours with brief comments:

Melt no.	Composition	Volume (CC)	Mass (g)	Comments
1	FeCrMnNiCu	1.5	13	<ol style="list-style-type: none">1. Mass didn't fit the crucible perfectly2. Near equiatomic3. Two phases observed4. Re-melting has been recommended
2	FeCrMnNiCu	1.25	10.78	Three phases: <ol style="list-style-type: none">1. Near equiatomic2. Depletion in Cu, high Fe3. Only Cr
3	FeCrMnNiB	1.5	10	Two phases: <ol style="list-style-type: none">1. Depletion in B and Cr, with the increase in Mn, Fe and Ni2. Forming CrB with depletion in other elements

4	CuCrMnAlB	2	9.5	<ol style="list-style-type: none"> 1. Half amount only of B was added 2. Many pores formed 3. Forming (CrB) phase 4. Al & Cu depleted in the other phase
5	AlCrNiTiSi	1.5	10.34	<ol style="list-style-type: none"> 1. The melt was not completed. Al was added instead of Ti, so there is no Ti in this system
6	AlCrNiTiSi	1.25	8.61	<p>Half the amount of Al was added.</p> <p>Two phases were observed:</p> <ol style="list-style-type: none"> 1. NiAl phase with depletion in SiTiCr 2. Forming CrSiTi with low AlNi
7	AlCrNiTiSi	1.25	8.35	<p>A quarter amount of Al was added</p> <p>Two phases:</p> <ol style="list-style-type: none"> 1. Forming NiAl phase with depletion in SiTiCr 2. Forming CrSiTi with depletion in AlNi
8	AlCrNiMgiSi	1.35	9.37	<ol style="list-style-type: none"> 1. Melting wasn't completed because of too much emissions

9	AlCrNiZrSi	1.2	10.32	<p>Half the amount of Al was added.</p> <p>Forming three phases:</p> <ol style="list-style-type: none"> 1. High Si, Cr and Zr with depletion in Al, Ni 2. Depletion in Si no Zr, with the increase in AlCrNi 3. Forming CrSi phase, depletion in Al and Ni with no Zr
10	AlCrNiZrSi	1.2	10.32	<p>The same composition as melt9.</p> <p>Ball miller machine used aiming to reach more homogeneity. Almost the same result. Forming three phases.</p>
11	FeCrMnNiB	1.2	8.18	<p>Two phases:</p> <ol style="list-style-type: none"> 1. One has high B with depletion in Ni 2. Other has high Ni with very low Cr
12,13,14	FeCrMnNiB	1.2	8.18	<ol style="list-style-type: none"> 1. Samples repeated at different times 2. Results showed two phases also
15	CrNiNbMo	1	7.95	<p>Two phases:</p> <ol style="list-style-type: none"> 1. MoNbCr, high at. % of Mo (60 at. %).

				2. Depletion in Mo with increasing of the other elements
16	CrNiNbMoB ₈ at. %	0.7	8.05	Melt wasn't completed (cracks issue)
17	CrNiNbMoC ₈ at. %	0.7	8.06	Three phases: 1. High Mo with low Ni 2. Near equiatomic with a bit high Mo 3. Depletion in Mo with high Cr
18	CrNiNbMoC ₂ at. %	0.8	9.12	Two phases: 1. High Mo and C, low Ni 2. Depletion in Mo, high Ni
19	CrNiNbMoB ₂ at. %	0.8	9.11	Two phases: 1. High Mo and B, low Ni 2. Depletion in Mo
20	CrNiNbMoSi ₂ at. %	0.8	9.16	Two phases: 1. High Mo 2. Depletion in Mo
15-20	-	-	-	All samples have Mo separation
21	CrMnNiNb	1	9.81	Three phases: 1. Near equiatomic 2. High at. % of Nb (45 at. %). 3. Depletion in Nb & Cr with increasing the Mn and Ni
22	FeCrSiZr	1.3	9.92	Three phases:

				<ol style="list-style-type: none"> 1. Near equiatomic 2. High at. % of Zr 3. Forming ZrSi phase with depletion in Cr and Fe
23	FeCrSiZr	1.2	8.66	<p>Two phases:</p> <ol style="list-style-type: none"> 1. High Si and Zr 2. High Cr & Fe
24	FeCrSiZrNb	1.2	9.29	<p>Three phases:</p> <ol style="list-style-type: none"> 1. Near equiatomic 2. High SiZrNb, depletion in CrFe 3. High CrNb with depletion in Si, Fe and Zr
25	FeCrSiZrC _{10 at. %}	1.25	9.21	<p>Three phases:</p> <ol style="list-style-type: none"> 1. Near equiatomic 2. High at. % of Cr, no Zr 3. Forming CrZr only
22-25	-	-	-	Samples have Zr separation
26	FeCrSiTi	1.3	8.43	<p>Two phases:</p> <ol style="list-style-type: none"> 1. One is near equiatomic 2. Forming SiTi, depletion in Cr and Fe
27	FeCrSiNb	1.2	8.7	<p>Two phases with some clear areas:</p> <ol style="list-style-type: none"> 1. High at. % of Nb

				2. Depletion in Nb with increasing of the other elements
28	FeCrMnNb	1.2	8.22	Two phases: 1. High at. % of Nb 2. Depletion in Nb with increasing of the other elements
29	FeCrMnNiC _{10 at. %}	1	8.05	Two phases: 1. Near equiatomic 2. Forming CrC phase with depletion in other elements
30	FeCrMnNiC _{5 at. %}	1	7.92	Two phases 1. Near equiatomic 2. Forming CrC phase with depletion in Fe, Mn & Ni
31	FeCrMnNiC _{20 at. %}	1	7	Two phases: 1. Equiatomic 2. Forming CrC phase with depletion in other elements
32	FeCrMnNiC _{2 at. %}	0.9	7.07	A single phase has been achieved

All melts have been prepared using vacuum arc melting

Summary

- All the prepared alloy compositions, either in the form of four or five elements, were chosen as new alloys, and they have not been reported yet by another researcher up to date.
- The reason behind choosing particular elements, such as Cr, Ni, Mo, Nb, Al, Si, Ti, Zr, Cu, C and B, is to increase the corrosion resistance of the alloys.
- The rational composition of all alloys was equiatomic or near equiatomic as it was aimed to follow the main definition of high entropy alloys or compositionally concentrated alloys, except few cases where a certain element was reduced to reach to single-phase alloy.
- Around 32 melts of different compositionally concentrated alloys have been prepared by arc melting furnace aiming to reach a single-phase high entropy alloy
- It has been achieved from the experiments that mass between 9-10 g of the composition is suitable and helpful during the melting process to control the composition within the melting process
- Re-melting three or four times is very important to acquire a good homogeneity
- Adding 25% or 50% atomic weight of light elements helps to achieve equiatomic or near- equiatomic per cent of the composition
- Phase separation can be reduced by decreasing some elements' atomic percentages, such as using only 1 to 5 at. % of an element
- Eventually, a high entropy single-phase alloy (FeCrMnNiC_2 at. %) has been successfully reached

Appendix II

Oil specification

Gialo high field (Libya)

Well name: 6K2

The oil sample was taken from the top of the well.

API = 36.5 to 37.1

Salt = 50 ptb (pounds per thousand barrel)

BS & W (bottom sediment and water) = 0.03 to 0.09 %

Pour point = 50 °F

H₂S liquid phase = 150 ppm

H₂S vapour phase = 14000 ppm (part per million)